DISSERTATION

DAMPING MECHANISMS IN MAGNETIC RECORDING MATERIALS & MICROWAVE-ASSISTED MAGNETIZATION REVERSAL

Submitted by

Lei Lu

Department of Physics

In partial fulfillment of the requirements

For the Degree of Doctor of Philosophy

Colorado State University

Fort Collins, Colorado

Spring 2014

Doctoral Committee:

Advisor: Mingzhong Wu

Martin P. Gelfand
Pavel Kabos
Mario C. Marconi
Carl E. Patton

ABSTRACT

DAMPING MECHANISMS IN MAGNETIC RECORDING MATERIALS & MICROWAVE-ASSISTED MAGNETIZATION REVERSAL

Understanding the damping of magnetization precession in magnetic recording materials is of both fundamental and practical significance. From the practical perspective, the relaxation processes not only set a natural limit to the time of magnetization switching which determines recording data rates, but also play critical roles in advanced magnetic recording techniques such as microwave-assisted magnetic recording and two-dimensional magnetic recording.

Experimental and theoretical studies of magnon-electron scattering and two-magnon scattering (TMS) contributions to magnetization relaxations in magnetic recording head and media materials were conducted for the first time in this dissertation. The accuracy of ferromagnetic resonance (FMR) measurements was increased by the use of vector network analyzer (VNA) FMR techniques. Working equations of the grain-to-grain TMS and grain boundary TMS processes were developed based on the TMS models of Krivosik and Mo, and were applied to understand the relaxation mechanisms in various recording-related thin film materials. The dependences of the FMR behavior and relaxation rates on the external field orientation, the microwave frequency, and the temperature were investigated experimentally in the following three domains: the exchange-coupled composite media, the free layers of tunnel magneto-resistance readers, and FeCo alloy films for future writers. The theoretical models were used to analyze the experimental data and to understand the relaxation mechanisms.

Microwave-assisted magnetization reversal (MAMR) is considered as a promising mechanism for further increasing the recording area density and pushing it beyond the super-paramagnetic limit. The MAMR operation was demonstrated with a 700-Gbit/in^2 perpendicular media sample in this thesis study. For microwaves with frequencies close to the FMR frequency of the media, MAMR was observed for microwave power higher than a certain threshold. For microwaves with certain high power, MAMR was observed for a broad microwave frequency range which covers the FMR frequency and is centered below the FMR frequency.

ACKNOWLEDGEMENTS

I would like to thank my advisor Professor Mingzhong Wu for the patient guidance, encouragement, and advices which he has provided throughout my time as his student. He had brought me to the world of magnetization dynamics, and had been very supportive of my work since the days I began working on FeCo films which was my first graduate-level research project. He has supported me not only by providing a research assistantship, but also academically and emotionally through the rough road to finish this thesis. I remember that he used to say something like "whatever you do, do your best" to encourage me to keep working hard and never stop moving forward. And during the most difficult times when working on the media samples, he gave me the moral support and the freedom I needed to move on. Without his guidance and persistent helps this dissertation would not have been possible.

There are a lot of people I would like to express my gratitude to for their helps and supports during my Ph.D. study. I am very grateful to Professor Carl Patton for his sincere help and knowledge. He spent a lot of time in answering my questions on fundamentals of FMR techniques and magnetization relaxation theories. I would like to thank Professor Boris Kalinikos who taught me a lot on spin-wave theories and microwave device physics. I must express my gratitude to Mr. Mike Kabatek, for his tremendously contributions on building the VNA-FMR spectrometer, which allowed me to complete the work on media damping. Completing this thesis would have been all the more difficult were it not for the help and friendship I received from the other members of Microwave Magnetics and Nanomagnetism Group at CSU.

Lastly, I would like to thank my wife Xiaoran Wang for her patience, inspiration, and love throughout my graduate studies. I am very grateful to her willingness to proof read countless pages of my writings, although most contents make no sense to her. LaiLai Lu, although she is too little to help, I would like to thank her for all the joys she brought to the family.

This work was supported in part by Seagate Technology, Western Digital Corporation, the U. S. National Science Foundation, and the U. S. National Institute of Standards and Technology.

TABLE OF CONTENTS

CHAPTER 1. INTRODUCTION

The EMC-IDC Digital Universe 2012 report projects the explosive growth of the digital universe through the end of the decade. In the United States, the amount of data created, replicated, and consumed each year will grow an amazing 6 fold through the end of the decade, and will reach 6.6 zettabytes by 2020, according to the EMC-IDC Digital Universe 2020 study. It is thus vitally important to ensure the continuous rapid increases in the capacity of the ubiquitous hard disk drive (HDD) that provides the foundation for this digital universe (Shiroishi 2009). Fundamental understanding on the magnetization dynamic of the ferromagnetic materials used in recording readers, writers, and media materials becomes more and more crucial with the rapid demanding incensement of both the recording area density and the data rate. On the other hand, the HDD industry is at its critical technology cross roads, and several comprehensive technology options such as bit patterned media magnetic recording, energy-assisted magnetic recording, and two-dimensional magnetic recording are under developing to push the areal density beyond the limit. Microwave-assisted magnetic recording is one of the few promising technology options for the realization of next-generation magnetic recording at several terabits per square inch.

1.1. Magnetization precession and relaxation concepts

Ferromagnetic materials exhibit a long-range ordering phenomenon at the atomic level which causes the unpaired electron spins to tend to line up parallel with each other in a region called magnetic domain. Within one magnetic domain, the magnetic moments are well aligned

and one has the so-called spontaneous magnetization. Multiple magnetic domains with randomly orientated magnetization is usually observed in ferromagnetic materials, and an external magnetic field can cause the magnetic moments in the domains to line up with each other and the material is said to be magnetized. Under a larger external field, all the microscopic magnetizations may line up to the same direction and stay at the static equilibrium. Any perturbation that drives the magnetization away from its equilibrium will induce the magnetization to precess around the equilibrium direction. The magnetization eventually relaxes back to its equilibrium at a certain decay rate.

A small-amplitude transverse microwave field can be used to drive the magnetization precession and compensate the loss. As the microwave frequency meets the precession frequency, the amplitude of the excited precession reaches its maximum and shows a resonance response which is the well-known ferromagnetic resonance (FMR) effect. The microwave energy stored in the magnetization precession typically decays due to microwave damping or relaxation, and the evaluation of the relaxations is usually a rather complex task. Magnon-electron scattering (MES) and two-magnon scattering (TMS) are usually considered as the dominated damping mechanisms in ferromagnetic thin films, with the former being viewed as intrinsic loss while the latter as extrinsic loss (Sparks 1961, Schlömann 1969).

A large-amplitude transverse microwave field with its frequency close to the FMR frequency can excite large-angle magnetization precession, and the large-angle precession can lower the energy barrier for the magnetization rotation reversal in single-domain elements and that for

domain nucleation or domain wall motion in multi-domain materials, resulting in the magnetization reversal at relatively small switching fields.

1.2. Outline of the dissertation

This dissertation presents comprehensive studies on magnetization dynamics in various ferromagnetic thin films currently used or to be used in the HDD technology, including the free layers of tunnel magneto-resistance readers, high-moment FeCo thin films for future perpendicular recording writers, and exchange-coupled perpendicular recording media. Demonstration of microwave-assisted magnetization reversal in commercial quality perpendicular media is also discussed.

Chapter 2 presents conceptual and qualitative descriptions about the uniform and non-uniform precessional motions of magnetization in the classical theory limit. Analysis on magnetization static equilibrium and magnetization dynamics is also discussed.

Chapter 3 presents a classical theory for the two-magnon scattering (TMS) relaxation process. Two types of scattering are discussed: (1) grain-to-grain TMS that arises from the random grain-to-grain fluctuations in the effective magneto-crystalline anisotropy field directions in polycrystalline thin films and (2) grain boundary-associated TMS. The concepts of the coupling factor, the density of degenerate states, and the ellipticity function are introduced and are used to derive the working formula for the TMS processes.

Chapter 4 presents the development of the vector network analyzer (VNA) FMR spectrometer and the derivation of the FMR expressions in terms of transmission coefficients.

It is shown that the VNA FMR spectrometer has a larger signal-to-noise ratio and a much broader operation frequency range than conventional shorted waveguide FMR spectrometers.

Chapter 5 reports on the damping properties in the free layers of tunnel magneto-resistance readers. The frequency-dependent FMR study with an external magnetic field normal to the film plane yielded a Gilbert damping constant of α=8.13×10^{-3}. Both the frequency-dependent FMR study with an external magnetic field along the in-plane easy axis and the polar angle-dependent FMR study indicated that the damping contribution from two-magnon scattering can't be ignored.

Chapter 6 reports on the tuning of magnetization relaxation in $Fe_{65}Co_{35}$ thin films via the use of different types of seed layers. Through the use of different seed layers, one can tune substantially both the magnitude and frequency dependence of the relaxation rate η of the film. This tuning relies on the change of the film grain properties with the seed layer and the correlation between the grain properties and the TMS processes. In spite of a significant change of η with the seed layer, the film static magnetic properties remain relatively constant. A change in the seed layer thickness produces insignificant effects on η.

Chapter 7 reports on the damping properties in perpendicular recording media. The experiments made use of a sample cut from a commercial quality 700-Gbit/in^2 media disk. The frequency-dependent FMR study indicated a Gilbert damping constant of α=0.056, and the temperature-dependent FMR study yielded α=0.05-0.15. These damping constants consist of contributions from breathing Fermi surface-associated relaxation and spin-flip magnon-electron

scattering, with the first process being slightly stronger than the second, and include no contributions from two-magnon scattering.

Chapter 8 presents the demonstration of microwave-assisted magnetization reversal (MAMR) in a 700-Gbit/in^2 perpendicular media sample. The microwave fields were applied by placing a coplanar waveguide on the media sample and feeding it with narrow microwave pulses. The switching states of the media grains were measured by magnetic force microscopy. For microwaves with a frequency close to the ferromagnetic resonance (FMR) frequency of the media, MAMR was observed for microwave power higher than a certain threshold. For microwaves with certain high power, MAMR was observed for a broad microwave frequency range which covers the FMR frequency and is centered below the FMR frequency.

1.3. Units

The Gaussian system (cgs) of base and derived units is used in this thesis. The magnetic field is expressed in the unit of Oe (Oersteds). The saturation induction is expressed in the unit of G (Gauss). The magnetic anisotropy energy is expressed in the unit of erg/cm^3. The exchange constant is expressed in the unit of erg/cm. The gyromagnetic ratio is expressed in the unit of MHz/Oe.

CHAPTER 2. PRECESSIONAL MOTION OF MAGNETIZATION

2.1 Uniform precessional motion

Magnetization dynamics has been studied for years for both bulk and thin film materials (Patton 1975, Hurben 1996, Nan 2006, Kalarickal 2006). Recently, magnetization dynamic behavior in magnetic thin films has attracted considerable attention for the improvement of currently magnetic recording technology. To be more specific, with the rapid increase in the recording area density and the data rate, understanding of magnetization relaxations in recording materials is of both fundamental and practical significance. From the practical perspective, the relaxation processes in the magnetic recording materials not only set a natural limit to the time of magnetization switching, but also play critical roles in new advanced magnetic recording technologies, such as microwave-assisted magnetic recording, domain wall-assisted recording, and two-dimensional magnetic recording. Earlier works have shown that the two main contributions to the magnetization relaxation in thin films include: (1) a near intrinsic magnon-electron scattering (MES) contribution that could be modeled as Gilbert (G) damping (Gilbert 2004) and (2) a magnon interaction-related extrinsic contribution named as two-magnon scattering (TMS) (McMichael 2004). Both the processes are described in detail later in this chapter.

This section introduces the dynamics of the uniform precession. The purpose of this section is to introduce the concepts and the background which are needed by the presentation in the following sections. Consider the simplest configuration (Stancil 1993) - an electron moving

in an atomic orbital. The trajectory of the electron motion is a circular loop as shown in Fig. 2.1. The electron motion induced current can be written as $I = \frac{ev}{2\pi r}$, where e is the charge of electron, v is the electron traveling velocity, and r is the radius of the electron orbit. The magnetic moment (vector) generated by the electron motion can be expressed as $\boldsymbol{\mu} = IA\hat{\mathbf{n}}$, where $\hat{\mathbf{n}}$ is a unit vector normal to the loop area surface determined by the right-hand rule and A is the area of the electron orbit. On the other hand, the orbital angular momentum (vector) of the traveling electron can be expressed as $\mathbf{l} = \mathbf{r} \times \mathbf{p} = \mathbf{r} \times m_e \mathbf{v}$, where m_e is the electron mass. It is a vector pointing in the opposite direction of $\boldsymbol{\mu}$. In the presence of a magnetic field **H**, a magnetic torque arises and causes a change in the angular momentum according the Newton's second law, as described by

$$\frac{d\mathbf{l}}{dt} = \boldsymbol{\mu} \times \mathbf{H} \tag{2.1}$$

In the classical theory, the relation between the magnetic moment and the orbital angular momentum is given as.

$$\boldsymbol{\mu} = -\frac{e}{2m_\mathrm{e}}\mathbf{l} = \gamma_\mathrm{l}\mathbf{l} \tag{2.2}$$

Explicitly, the gyromagnetic ratio for the orbital motion is defined as

$$\gamma_l = -\frac{e}{2m_e} \tag{2.3}$$

A similar approach can be introduced to describe the electron spin precession, and the equation of motion can be written as Eq. (2.4).

$$\frac{d\mathbf{s}}{dt} = \boldsymbol{\mu} \times \mathbf{H} \tag{2.4}$$

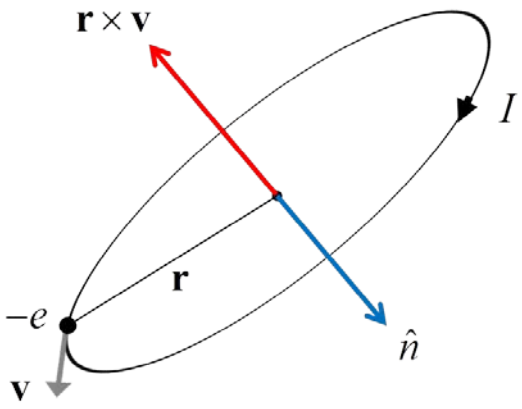

FIG. 2.1. Schematic diagram of an orbiting electron. The electron has a mass of m_e, carries a negative charge of $-e$, and travels at a speed of $\mathbf{v}$. The radius of the circular loop is $\mathbf{r}$. The current generated by the orbiting electron is I. $\hat{n}$ is a vector unit normal to the loop area surface.

Similar to the equation of the orbital motion, Eq. (2.4) is also set up based on the Newton's second law. However, the orbital angular momentum $\mathbf{l}$ is replaced by the spin angular momentum $\mathbf{s}$ in the equation of motion for the electron spinning. The magnetic moment $\boldsymbol{\mu}$ is defined in a different manner. In the classical limit, the magnetic moment of an electron spin can be described as.

$$\boldsymbol{\mu} = -g_e \frac{e}{2m_e}\mathbf{s} = \gamma_e \mathbf{s} \tag{2.5}$$

One can tell that a factor g_e is added in the expression of the magnetic moment for electron spin. The quantum mechanical calculation tells that the gyromagnetic ratio γ_e for an electron spin is different by a factor of 2 from the gyromagnetic ratio γ for electron orbiting. This is because the Landé g factor equals to 1 for pure orbital angular momentum and 2 for pure

spin angular momentum. With the Landé g factor, a general expression for the gyromagnetic ratio is given as

$$\gamma = -g\frac{e}{2m_e} \tag{2.6}$$

The value of the gyromagnetic ratio for a single electron spin was found to be

$$\frac{|\gamma_s|}{2\pi} = 2.8 \text{ MHz/Oe} \tag{2.7}$$

Combining Eq. (2.4) and Eq. (2.5), the time dependence of the magnetic moment $\boldsymbol{\mu}$ can be written as

$$\frac{d\boldsymbol{\mu}}{dt} = -|\gamma_e|\boldsymbol{\mu}\times\mathbf{H} \tag{2.8}$$

Eq. (2.8) is the well-known torque equation which is widely used to describe the precessional motion of a single electron spin. Usually the collective behavior of massive spin precessions are detected and studied. The spins spontaneously align in a ferromagnetic material, and this strong magnetic ordering is caused by the magnetic exchange interaction. In the consideration of describing the collective motion of massive spins, the magnetization $\mathbf{M}$ is used to replace the magnetic moment $\boldsymbol{\mu}$, as shown in Eq. (2.9).

$$\frac{d\mathbf{M}}{dt} = -|\gamma|\mathbf{M}\times\mathbf{H} \tag{2.9}$$

Eq. (2.9) is the equation of the motion for magnetization, which is different from the torque equation for a single electron spin by two parameters, $\mathbf{M}$ and γ. The magnetization $\mathbf{M}$ represents the total magnetic moment of a large collection of spins in a unit volume, defined as

$$\mathbf{M} = \sum_{i=1}^{n}\frac{\boldsymbol{\mu}_i}{V} \tag{2.10}$$

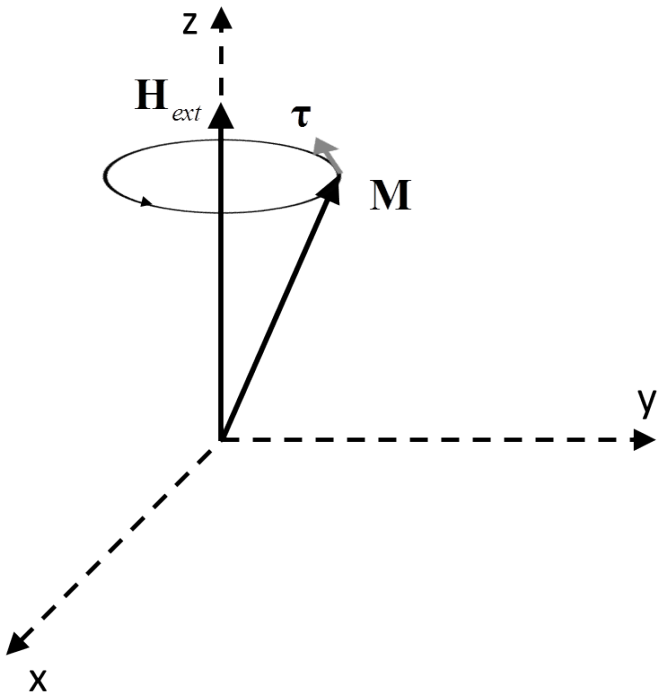

FIG. 2.2. Schematic graph of magnetization precession. The external magnetic field $\mathbf{H}_{ext}$ is along the *Z* axis. The magnetization $\mathbf{M}$ precesses around the *Z* axis, and this precession motion is along the count-clockwise direction (viewed from the top) and is called as the Lamar precession. The torque equals to the cross product of the magnetization and the external magnetic field, which always points along the tangential direction of the trajectory.

$\boldsymbol{\mu}_i$ represents the magnetic moment of an individual spin *i* within the unit volume V. The gyromagnetic ratio γ of magnetization could have a different value from that of single spin magnetic moment, because of the difference of Landé g factor. Different gyromagnetic ratio values have been reported for different magnetic materials. The analysis below takes the simplest consideration in which all the spins are behaving in phase and there are no spatial

variations. Under this approximation, the magnetization is considered to be time dependent only and no spatial variation is involved. Eq. (2.11) is the equation of motion for magnetization in the classical limit, which is also known as the Landau-Lifshitz (LL) torque equation.

$$\frac{d\mathbf{M}(t)}{dt} = -|\gamma|\mathbf{M}(t)\times\mathbf{H} \tag{2.11}$$

Figure 2.2 shows schematically the motion of magnetization. The torque $\boldsymbol{\tau} = \mathbf{M}\times\mathbf{H}$ is pointing along the tangential direction of the spin precession trajectory, and the $\mathbf{M}$ is driven by the torque to precess around the magnetic field $\mathbf{H}$. This precession of $\mathbf{M}$ is assumed to have a harmonic time dependence and have no spatial variation. Once the sample properties and the external magnetic field $\mathbf{H}$ are specified, the motion of $\mathbf{M}$ can be resolved, and the precession frequency ω_0 can also be found. Generally ω_0 depends on a number of factors such as the external magnetic field, the sample geometry, and the magneto-crystalline anisotropy. All these factors will be included in the analysis later in this chapter. At this point, take the simplest consideration of an infinite, isotropic material where no sample dimensions or anisotropy fields are under consideration, the precession frequency ω_0 predicted by Eq. (2.11) is found to be $\omega_0 = |\gamma|H$ (Kittel 1948).

2.2 Phenomenological damping model

In the following subsections, the torque equation is going to be revised into more complicated forms with more factors considered. Equation (2.11) describes the magnetization precession in an ideal system without loss. The spin undergoes non-dispersive precession since no term counting the energy dissipation. However, damped magnetization precessions are

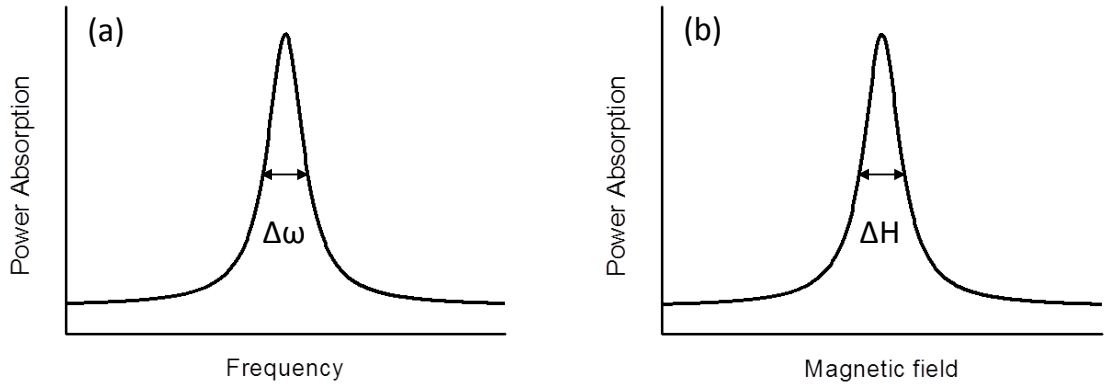

FIG. 2.3. Schematics of ferromagnetic resonance (FMR) power absorption profiles. (a) FMR power absorption profile for sweeping the microwave frequency at a fixed external magnetic field. (b) FMR power absorption profile for sweeping the external magnetic field at a fixed microwave frequency.

always observed in experiments due to non-avoidable loss. Equation (2.12) is the modified torque equation with a damping term added.

$$\frac{d\mathbf{M}(t)}{dt} = -|\gamma|\mathbf{M}(t)\times\mathbf{H}(t) + damping \tag{2.12}$$

There exist several phenomenological models to describe the damped magnetization precession (Landou-Lifshitz 1935, Block-Bloombergen 1956, Patton 1975, Mckinstry 1991, Gilbert 2004). All the results and discussions involved in this dissertation are about metallic thin films. Since the Gilbert damping model is the most widely used model to explain the damping in metallic thin films, only the Gilbert model is going to be discussed. The spin dynamics in the classical limit can be described by the Gilbert equation of motion as Eq. (2.13).

$$\frac{d\mathbf{M}(t)}{dt} = -\left|\gamma\right|\mathbf{M}(t)\times\mathbf{H}(t) - \frac{\alpha}{M_s}\mathbf{M}(t)\times\frac{d\mathbf{M}(t)}{dt} \tag{2.13}$$

In Eq. (2.13), the damping term is considered as a persistent torque pointing towards the precession axis to drag the magnetization back to the equilibrium position, and α is the well-known Gilbert damping constant which is a dimensionless parameter. When the Gilbert damping constant is given, the relaxation rate η (in frequency units) can be calculated. The details are provided later in this chapter. The Gilbert damping is consistent with the theory of magnon-electron scattering which is the dominant phenomenological damping in metallic thin films.

The damping is related to the rate at which energy is lost from the precessing magnetization. In terms of ferromagnetic resonance, the damping is responsible for the finite linewidth of the measured ferromagnetic resonance (FMR) power absorption profile shown in Fig. 2.3. The widths of half maximum power $\Delta\omega$ (in frequency unit) and ΔH (in magnetic field unit), which are shown in Fig. 2.3 (a) and (b), respectively, are the standard experimental measures of loss in ferromagnetic materials. The damping can be extracted from the analysis of the FMR linewidths.

2.3 Analysis on magnetization static equilibrium

Before the discussion on dynamic behavior of the sample magnetization, the static equilibrium condition with the presence of a static external magnetic field is discussed (Hurben 1996). The applied static magnetic field is termed as the external magnetic field, and the direction of this field in Cartesian coordinate is considered to be pointing at some general

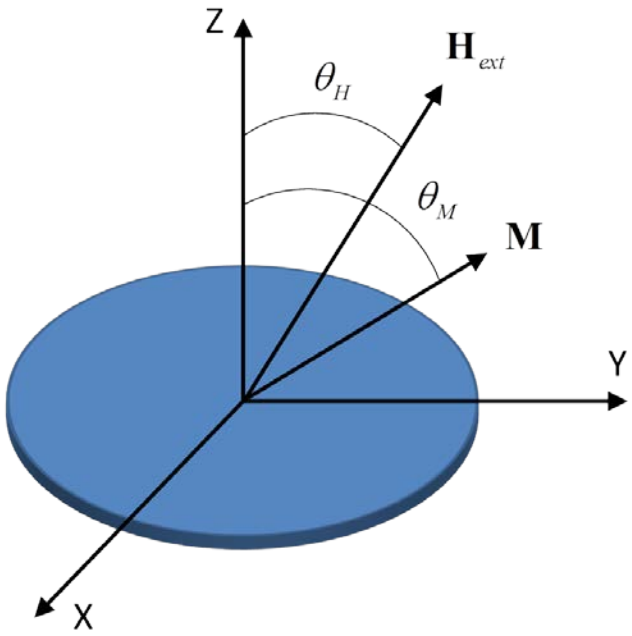

FIG. 2.4. The external magnetic field and magnetization configuration in the sample frame. The film normal direction is chosen to be the Z axis. The external magnetic field points at an oblique direction. The angle between the external magnetic field and the Z axis is θ_H. The plane contains both $\mathbf{H}_{ext}$ and the Z axis is set to be the $Y-Z$ plane. The magnetization also lies in the $Y-Z$ plane and points at an angle of θ_M with respect to the Z axis.

oblique angle. Unlike the situation discussed in Fig. 2.2, where the magnetization is precessing along the external magnetic field direction, the magnetization precession is no longer around the principle axis of the external magnetic field, and the precession axis is off from the external magnetic field axis with a certain angle, as shown in Fig. 2.4. The precession axis is set to be aligned with the magnetization since only small angle precession is under consideration. The misalignment between the magnetization and magnetic field is due to the presents of the

demagnetization field and the magneto-crystalline anisotropy. Demagnetization fields exist in magnetic samples with finite dimensions. In some literatures, the demagnetization field is also named as the magnetic shape anisotropy field. The effect of demagnetization fields can be considered as the accumulation of magnetic charges on the sample surfaces which have the tendency to reduce the alignment of total magnetization with the external magnetic field. The demagnetization field $\mathbf{H}_{\text{dem}}$ is related to the magnetization by geometry dependent constants called demagnetization factors. The relation between the demagnetization field and the demagnetization factors is given by

$$\mathbf{H}_{\text{dem}} = -4\pi \mathbf{N} \cdot M_{\text{s}} \tag{2.15}$$

The demagnetization matrix $\mathbf{N}$ is a 3×3 tensor. Both the sample geometry and the external magnetic field orientation affect the demagnetization field. It is easy to determine the demagnetization factors for samples with ordinary shapes, such as sphere, cylinder, and rectangular, but quite difficult for arbitrarily shaped magnetic objects. For the consideration of magnetic thin films, the demagnetization tensor is diagonal and has a relatively simple form as

$$\mathbf{N} = \begin{pmatrix} N_X & 0 & 0 \\ 0 & N_Y & 0 \\ 0 & 0 & N_Z \end{pmatrix} \tag{2.16}$$

The subscripts X, Y, and Z are defined as the coordinate axes in the sample frame. The sum of the demagnetization factors equals to 1, namely, $N_X + N_Y + N_Z = 1$. This relation is true for any sample shapes. As shown in Fig. 2.4, the disk stands for a typical thin film sample with its in-plane dimensions much larger than the sample thickness. As the in-plane

dimensions can be treated as infinity, one has $N_X = N_y = 0$ and $N_Z = 1$. For the external magnetic field configuration shown in Fig. 2.4, the demagnetization fields can be written as

$$\mathbf{H}_{\text{dem}} = \begin{pmatrix} 0 \\ -4\pi N_Y M_{\text{s}} \sin\theta_{\text{M}} \\ -4\pi N_Z M_{\text{s}} \cos\theta_{\text{M}} \end{pmatrix} \tag{2.17}$$

Equation (2.17) tells that the amplitude of the external magnetic field that required to conquer the demagnetization field and pull the magnetization along the external magnetic field direction is proportional to the sample saturation magnetization. The net magnetic field acting on the magnetization in the sample is the vector summation of the external magnetic field $\mathbf{H}_{\text{ext}}$ and the demagnetization field $\mathbf{H}_{\text{dem}}$. The presence of the demagnetization field gives rise to the misalignment between the magnetization and the external magnetic field. The magnetization is under a static equilibrium since it is directed parallel to the net field direction with zero torque exerted on it.

Magneto-crystalline anisotropy is the second static term going to be considered in this subsection, and it can lead to a change on the alignment between the magnetization $\mathbf{M}$ and the magnetic field of $\mathbf{H}_{\text{ext}} + \mathbf{H}_{\text{dem}}$. Magneto-crystalline anisotropy is the dependence of the internal magnetic energy of a ferromagnetic material on its crystalline directions. As a consequence, certain crystallographic directions are preferred directions for the magnetization, namely, the easy axes. Spin-orbit interactions are usually considered to be the primary source of magneto-crystalline anisotropy. One can express the anisotropy in terms of the free energy of the magnetization. Only the uniaxial magnetic anisotropy is going to be discussed in this

dissertation. The free energy for a uniaxial magnetic anisotropy generally can be in the form of

$$F_u(M_X, M_Y, M_Z) = K(1 - \frac{M_Z^2}{M_s^2}) \tag{2.18}$$

where M_s is the saturation magnetization. The easy axis direction is set to be along the *Z* axis, and M_z is the component of $\mathbf{M}$ along the easy axis. In the perpendicular magnetic recording media materials, there always exists extremely high uniaxial magnetic anisotropy pointing in the media film normal direction. This magnetic anisotropy has to be sufficient large to conquer the demagnetization field and pull the magnetizations along the *Z* axis. Chapter 7 explicitly discusses the magnetic static and dynamic behaviors of perpendicular magnetic recording media.

It is important to include the magnetic anisotropy in the magnetic static equilibrium analysis. It is convenient to describe the uniaxial magnetic anisotropy by the use of an effective static uniaxial magnetic anisotropy field H_u. According to Eq. (2.18), the effective uniaxial magnetic anisotropy field can be derived as.

$$\mathbf{H}_{\mathrm{u}} = -\nabla_{\mathrm{M}} F_{\mathrm{u}}(M_X, M_Y, M_Z) \tag{2.19}$$

The magneto-crystalline anisotropy field is generally expressed as an expansion in series of the magnetization trigonometric functions. Explicitly, the expression for a uniaxial magnetic anisotropy along the *Z* axis is given by

$$H_{\mathrm{u}}\hat{Z} = -K\frac{\partial}{\partial M_Z}(1 - \frac{M_Z^2}{M_{\mathrm{s}}^2}) = \frac{2K}{M_{\mathrm{s}}}\frac{M_Z}{M_{\mathrm{s}}} = H_{\mathrm{A}}\cos\theta_{\mathrm{M}} \tag{2.20}$$

where $H_A = 2K / M_s$, $M_Z / M_s = \cos\theta_M$, and the uniaxial magnetic anisotropy field orients along the *Z* axis.

Similar to the demagnetization field, the magnetic anisotropy field also affects the net magnetic field orientation. It is convenient to use the concept of an effective magnetic field to represent the net magnetic field. The effective static magnetic field is defined as the vector sum of all the magnetic fields acting on the magnetizations, as given in Eq. (2.21).

$$\mathbf{H}_{\text{eff}} = \mathbf{H}_{\text{ext}} + \mathbf{H}_{\text{dem}} + \mathbf{H}_{\text{u}} \tag{2.21}$$

And the three components (*X*, *Y*, and *Z*) of the effective magnetic field can be written as Eq. (2.22).

$$\mathbf{H}_{eff} = \begin{pmatrix} 0 \\ H_{\text{ext}} \sin\theta_{\text{H}} - 4\pi N_Y M_s \sin\theta_{\text{M}} \\ H_{\text{ext}} \cos\theta_{\text{H}} - 4\pi N_Z M_{\text{s}} \cos\theta_{\text{M}} + H_{\text{A}} \cos\theta_{\text{M}} \end{pmatrix} \tag{2.22}$$

The static equilibrium occurs when the net torque working on the magnetization is zero, namely, $\mathbf{M}_s \times \mathbf{H}_{eff} = 0$. Under the static equilibrium one obtains,

$$\begin{pmatrix} \hat{X} & \hat{Y} & \hat{Z} \\ 0 & M_{\text{s}} \sin\theta_{\text{M}} & M_{\text{s}} \cos\theta_{\text{M}} \\ 0 & H_{\text{ext}} \sin\theta_{\text{H}} - 4\pi N_{\text{Y}} M_{\text{s}} \sin\theta_{\text{M}} & H_{\text{ext}} \cos\theta_{\text{H}} - 4\pi N_Z M_{\text{s}} \cos\theta_{\text{M}} + H_{\text{A}} \cos\theta_{\text{M}} \end{pmatrix} = 0 \tag{2.23}$$

The simplified expression of the above matrix given in Eq. (2.24) is the so-called equation of static equilibrium.

$$H_{\text{ext}} \sin(\theta_{\text{M}} - \theta_{\text{H}}) + \frac{1}{2}\left[4\pi M_{\text{s}}(N_Y - N_Z) + H_{\text{A}}\right]\sin(2\theta_{\text{M}}) = 0 \tag{2.24}$$

This static equilibrium equation is the key conclusion of this subsection. It tells that once the amplitude and orientation (θ_H) of the external magnetic field is fixed, the equilibrium angle (θ_M) of the magnetization can be determined if one knows the saturation magnetization, sample geometry, and magnetic anisotropy field.

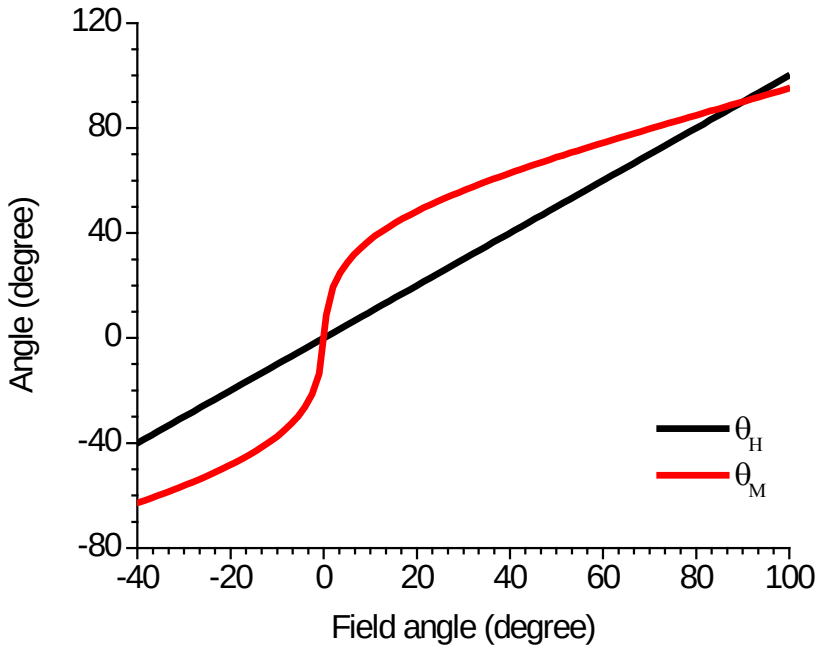

FIG. 2.5. Example of calculations of magnetization angle. A thin film configuration is considered in the calculations. The material has a saturation induction of 10.5 kG, and the external magnetic field has an amplitude of 11.0 kOe. No anisotropy magnetic field is considered. The black line is the magnetic field angle vs. itself, and the red curve is the magnetization angle vs. the magnetic field angle.

Figure 2.5 shows example calculations of the magnetization angle. The black and red lines have cross points at 0 degree (out-of-plane) and 90 degree (in-plane) field angles. The gap between the two lines at other angles is due to the existence of the demagnetization field. The anisotropy magnetic field is not in the consideration. Figure 2.6 shows specific examples on the static equilibrium calculation where the external magnetic fields have the same angle but different amplitudes. The black line crosses the colored curves at different points indicates, and

this indicates that the static equilibrium happens at different magnetization angles for different external magnetic field amplitudes.

With the determination of static equilibrium of the magnetization, the amplitude of the internal magnetic field acting on the magnetization can be calculated with Eq. (2.25).

$$\begin{aligned} H_{\text{int}} = &\left[H_{\text{ext}} \sin\theta_{\text{H}} - 4\pi N_Y M_{\text{s}} \sin\theta_{\text{M}}\right]\sin\theta_{\text{M}} \\ &+\left[H_{\text{ext}} \cos\theta_{\text{H}} - 4\pi N_Z M_{\text{s}} \cos\theta_{\text{M}} + H_{\text{A}} \cos\theta_{\text{M}}\right]\cos\theta_{\text{M}} \end{aligned} \tag{2.25}$$

Equation (2.26) gives the simplified form of internal magnetic field, which is the key result of this subsection and will be used throughout the dissertation. It brings a considerable simplification to use this single internal magnetic field rather than work with several magnetic fields ($\mathbf{H}_{\text{ext}}$, $\mathbf{H}_{\text{dem}}$, and $\mathbf{H}_{\text{u}}$). One can also determine the internal magnetic field by measuring the ferromagnetic resonance. Studying the internal magnetic field through FMR, one can determine the static magnetic properties of the material, including the saturation magnetization and the magnetic anisotropy field. Specific examples are given in Chapter 5.

$$H_{\text{int}} = H_{\text{ext}} \cos(\theta_{\text{H}} - \theta_{\text{M}}) - 4\pi M_{\text{s}}(N_Y \sin^2\theta_{\text{M}} + N_Z \cos^2\theta_{\text{M}}) + H_{\text{A}} \cos^2\theta_{\text{M}} \tag{2.26}$$

2.4 Analysis of magnetization dynamics

So far the analysis on magnetization static equilibrium is developed in the sample frame. The following analysis will be focusing on the magnetization dynamics, namely, the precessional motion of the magnetization around the principle axis of the internal magnetic field. A new coordinate frame of reference is introduced, which provides considerable simplification on the magnetization dynamics analysis. The new coordinate system is known as the precession frame with x-, y-, z-axis as shown in Fig. 2.7.

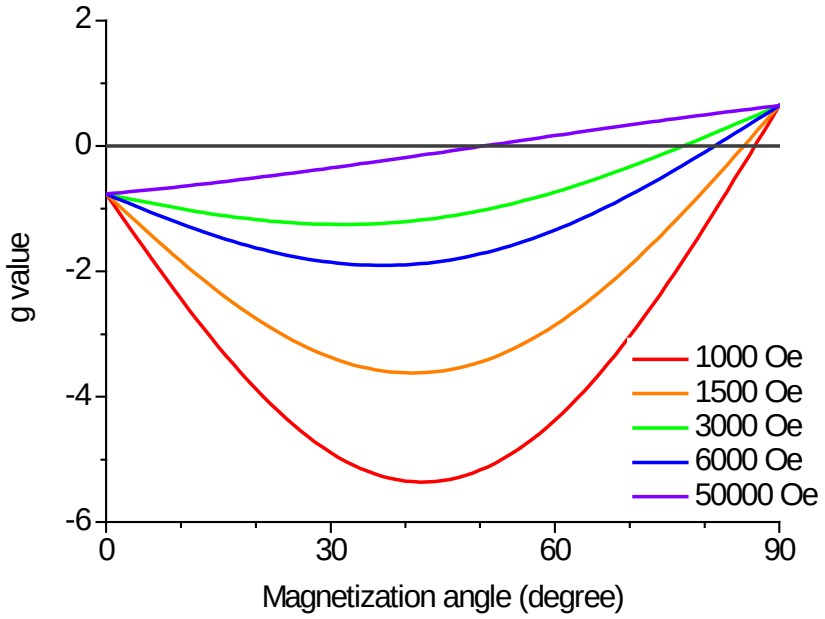

FIG. 2.6. Example of finding the static equilibrium. A thin film configuration is considered in the calculations. The material has a saturation induction of 10.5 kG. The external magnetic fields have the same angle - 50 degree off from the film normal direction but different amplitudes in the 1-50 kOe range. No anisotropy magnetic field is considered. The g value label on the vertical axis has the expression of $\sin(\theta_{\mathrm{M}} - \theta_{\mathrm{H}}) - 2\pi M_{\mathrm{s}} \sin(2\theta_{\mathrm{M}}) / H_{\mathrm{ext}}$ which is equivalent to Eq. (2.24). The static equilibrium happens when the g equals to zero.

The magnetization dynamic components lie in the x-y plane, while the internal magnetic field orientation is along the orthogonal *z*-axis. Take a brief summary on the coordinate system definition: the uppercase letters *X*, *Y*, *Z* represent the Cartesian coordinates in the sample frame, and the lowercase letters *x*, *y*, *z* represent the Cartesian coordinates in the magnetization precession frame. The conversion between the magnetization precession frame and the sample

frame can be implemented by the rotation matrix given in Eq. (2.27) and the inverse matrix given in Eq. (2.28).

$$T = \begin{pmatrix} 1 & 0 & 0 \\ 0 & \cos\theta_{\mathrm{M}} & -\sin\theta_{\mathrm{M}} \\ 0 & \sin\theta_{\mathrm{M}} & \cos\theta_{\mathrm{M}} \end{pmatrix} \tag{2.27}$$

$$T^{-1} = \begin{pmatrix} 1 & 0 & 0 \\ 0 & \cos\theta_{\mathrm{M}} & \sin\theta_{\mathrm{M}} \\ 0 & -\sin\theta_{\mathrm{M}} & \cos\theta_{\mathrm{M}} \end{pmatrix} \tag{2.28}$$

The two frames obey the relation given in Eq. (2.29).

$$V_{xyz} = T \cdot V_{XYZ} \cdot T^{-1} \tag{2.29}$$

Ferromagnetic resonance is one of the standard ways to probe the magnetization dynamics. Typically, the ac magnetic component of a microwave is used to drive the magnetization precession and compensate the loss. An energy transfer from the microwave to the magnetic system occurs when the microwave frequency meets the magnetization precession frequency. One can use the microwave power absorption curves to characterize the collective behavior of magnetizations in the specimen.

Both the magnetization and the magnetic field have the dynamic components while in ferromagnetic resonance. The magnetization dynamic components come from the magnetization precession, and the magnetic field dynamic components originate from the applied microwave. The $\mathbf{M}$ and $\mathbf{H}$ vectors can be separated into static and dynamic parts with Eqs. (2.30) and (2.31).

$$\mathbf{M}(t) = M_{\mathrm{s}}\hat{\mathbf{z}} + \mathbf{m}(t) \tag{2.30}$$

$$\mathbf{H}(t) = H\hat{\mathbf{z}} + \mathbf{h}(t) \tag{2.31}$$

$\mathbf{m}(t)$ and $\mathbf{h}(t)$ represent the dynamic components. In the small signal approximation of ferromagnetic resonance, the dynamic component of the magnetic field has very small amplitude. The angle between the magnetization and the internal magnetic field is also very small, and, in other words, only small-angle magnetization precession is induced. Thus, the dynamic component of the magnetization is considered also to be very small, namely, $|\mathbf{m}(t)| \ll M_s$. Only linear effects are under consideration, and any nonlinear effects are beyond the consideration of this thesis.

In order to show a full perspective of the magnetization dynamics, the dynamic demagnetization field and the anisotropy field raised from the dynamic components of magnetization are also considered. The time dependent demagnetization field has the form of Eq. (2.32).

$$\mathbf{H}_{\text{dem}}(t) = -4\pi N \cdot \mathbf{M}(t) \tag{2.32}$$

The demagnetization field is also considered to have a static component and a dynamic component as given in Eq. (2.33).

$$\mathbf{H}_{\text{dem}} + \mathbf{h}_{\text{dem}}(t) = -4\pi N \cdot (M_{\text{s}}\hat{\mathbf{z}} + \mathbf{m}(t)) \tag{2.33}$$

The analysis of the static demagnetization field is done in the sample frame, and the expressions for the dynamic demagnetization field will be developed in the magnetization precession frame. The demagnetization factor can be converted easily between the two frames

by using the rotation matrix as Eq. (2.34).

$$N_{xyz} = T \cdot N_{XYZ} \cdot T^{-1} \tag{2.34}$$

The demagnetization tensor under the magnetization precession frame was found to be Eq. (2.35).

$$N_{xyz} = \begin{pmatrix} N_X & 0 & 0 \\ 0 & N_Y \cos^2\theta_{\mathrm{M}} + N_Z \sin^2\theta_{\mathrm{M}} & \dfrac{(N_Y - N_Z)}{2}\sin(2\theta_{\mathrm{M}}) \\ 0 & \dfrac{(N_Y - N_Z)}{2}\sin(2\theta_{\mathrm{M}}) & N_Y \sin^2\theta_{\mathrm{M}} + N_Z \cos^2\theta_{\mathrm{M}} \end{pmatrix} \tag{2.35}$$

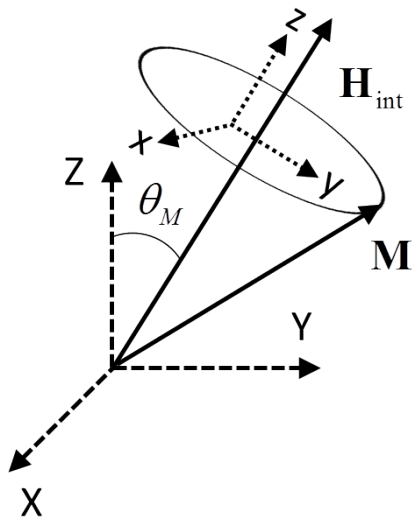

FIG. 2.7. The external magnetic field and magnetization configuration in the precession frame. The internal magnetic field direction is chosen to be the z axis. The angle between the internal magnetic field and the Z axis is θ_{M}. The magnetization precesses around the principle axis of the internal magnetic field. And the dynamic component of the magnetization lies in the $x-y$ plane.

One can directly obtain the dynamic demagnetization field by using the expression, $\mathbf{h}_{\text{dem}}(t) = -4\pi N \cdot \mathbf{m}(t)$. This field is shown in Eq. (2.36).

$$\mathbf{h}_{\text{dem}} = \begin{pmatrix} -4\pi N_X m_{0x}(t) \\ -4\pi(N_Y \cos^2\theta_{\text{M}} + N_Z \sin^2\theta_{\text{M}}) m_{0y}(t) \\ -2\pi(N_Y - N_Z)\sin\theta_{\text{M}} m_{0y}(t) \end{pmatrix} \tag{2.36}$$

Besides the dynamic demagnetization field, the other dynamic magnetic field considered in this subsection is the dynamic magnetic anisotropy field. While working in the GHz frequency range, the complex magnetic susceptibility of ultrathin films could be significantly affected by the dynamic magnetic anisotropy field. Similar to the derivation of the dynamic demagnetization field, the derivation of dynamic magnetic anisotropy field will also be carried out in the magnetization precession frame. One can first transform the magnetization from the (x, y, z) frame to the (X, Y, Z) frame by formula $V_{XYZ} = T^{-1} \cdot V_{xyz}$.

$$\begin{pmatrix} M_X \\ M_Y \\ M_Z \end{pmatrix} = \begin{pmatrix} 1 & 0 & 0 \\ 0 & \cos\theta_{\text{M}} & \sin\theta_{\text{M}} \\ 0 & -\sin\theta_{\text{M}} & \cos\theta_{\text{M}} \end{pmatrix} \cdot \begin{pmatrix} m_x(t) \\ m_y(t) \\ M_z \end{pmatrix} \tag{2.37}$$

$$\begin{pmatrix} M_X \\ M_Y \\ M_Z \end{pmatrix} = \begin{pmatrix} m_x(t) \\ M_z \sin\theta_{\text{M}} + m_y(t)\cos\theta_{\text{M}} \\ M_z \cos\theta_{\text{M}} - m_y(t)\sin\theta_{\text{M}} \end{pmatrix} \tag{2.38}$$

Recall the Eq. (2.20), the overall magnetic anisotropy field in the sample frame can be expressed as Eq. (2.39).

$$\begin{pmatrix} (H_{\text{an}}(t))_X \\ (H_{\text{an}}(t))_Y \\ (H_{\text{an}}(t))_Z \end{pmatrix} = \frac{H_A}{M_s} \begin{pmatrix} m_x(t) \\ M_z \sin\theta_{\text{M}} + m_y(t)\cos\theta_{\text{M}} \\ M_z \cos\theta_{\text{M}} - m_y(t)\sin\theta_{\text{M}} \end{pmatrix} \tag{2.39}$$

The dynamic component of the magnetic anisotropy field rises from the dynamic component of

magnetization. And this dynamic anisotropy field in the sample frame can be written as Eq. (2.40).

$$\begin{pmatrix} (h_{\mathrm{an}}(t))_X \\ (h_{\mathrm{an}}(t))_Y \\ (h_{\mathrm{an}}(t))_Z \end{pmatrix} = \frac{H_{\mathrm{A}}}{M_{\mathrm{s}}} \begin{pmatrix} m_x(t) \\ m_y(t)\cos\theta_{\mathrm{M}} \\ -m_y(t)\sin\theta_{\mathrm{M}} \end{pmatrix} \tag{2.40}$$

Applying the rotation matrix to Eq. (2.40) one can directly get the expression for the dynamic magnetic anisotropy field in the precession frame as Eq. (2.41).

$$\begin{pmatrix} (h_{\mathrm{an}})_x \\ (h_{\mathrm{an}})_y \\ (h_{\mathrm{an}})_z \end{pmatrix} = T \cdot \begin{pmatrix} 0 \\ 0 \\ (h_{\mathrm{an}})_Z \end{pmatrix} = \frac{H_{\mathrm{A}}}{M_{\mathrm{s}}} \begin{pmatrix} 0 \\ m_y(t)\sin^2\theta_{\mathrm{M}} \\ -m_y(t)\dfrac{\sin(2\theta_{\mathrm{M}})}{2} \end{pmatrix} \tag{2.41}$$

A dynamic magnetic anisotropy tensor is introduced to make the expression simple (Kalarickal 2006), which is given in Eq. (2.42).

$$A = \frac{H_{\mathrm{A}}}{M_{\mathrm{s}}} \begin{pmatrix} 0 & 0 & 0 \\ 0 & m_y(t)\sin^2\theta_{\mathrm{M}} & 0 \\ 0 & -m_y(t)\dfrac{\sin(2\theta_{\mathrm{M}})}{2} & 0 \end{pmatrix} \tag{2.42}$$

Thereby the expression of the dynamic magnetic anisotropy in the (x, y, z) frame has a simple form of $h_{an}(t) = A \cdot m(t)$. This thesis only covers the derivation of working formulas for dynamic demagnetization field and dynamic anisotropy magnetic field.

2.5 Ferromagnetic resonance response

So far the static and dynamic components for the demagnetization field and the magnetic anisotropy field have been developed. With these new terms, the Gilbert equation (2.13) can be

written as Eq. (2.43).

$$\frac{d}{dt}\left[M_s\hat{z}+\mathbf{m}(t)\right]=-\left|\gamma\right|\left[M_s\hat{z}+\mathbf{m}(t)\right]\times\left[H_{\text{int}}\hat{z}+\left(A-4\pi N\right)\cdot\mathbf{m}(t)+\mathbf{h}(t)\right] \\ -\frac{\alpha}{M_s}\left[M_s\hat{z}+\mathbf{m}(t)\right]\times\frac{d}{dt}\left[M_s\hat{z}+\mathbf{m}(t)\right] \tag{2.43}$$

Because of the small signal approximation, all the second and higher order terms in $\mathbf{m}(t)$ or $\mathbf{h}(t)$ can be dropped, and the linearized Gilbert equation is expressed as Eq. (2.44)

$$\frac{d}{dt}\mathbf{m}(t)+\left|\gamma\right|\left[H_{\text{int}}\mathbf{m}(t)-M_s\left(A-4\pi N\right)\cdot\mathbf{m}(t)\right]\times\hat{z}-\frac{\alpha}{M_s}M_s\frac{d}{dt}\mathbf{m}(t)\times\hat{z}=\left|\gamma\right|M_s\mathbf{h}(t) \tag{2.44}$$

Eq. (2.45) shows the term including the demagnetization factor and the dynamic magnetic anisotropy matrix.

$$4\pi N_{xyz}-A=$$

$$\begin{pmatrix} -4\pi N_X & 0 & 0 \\ 0 & -4\pi\left(N_Y\cos^2\theta_{\text{M}}+N_Z\sin^2\theta_{\text{M}}\right)+\frac{H_{\text{A}}}{M_s}m_y(t)\sin^2\theta_{\text{M}} & -\frac{4\pi(N_Y-N_Z)}{2}\sin(2\theta_{\text{M}}) \\ 0 & -\frac{4\pi(N_Y-N_Z)}{2}\sin(2\theta_{\text{M}})-\frac{H_{\text{A}}}{M_s}m_y(t)\frac{\sin(2\theta_{\text{M}})}{2} & -4\pi\left(N_Y\sin^2\theta_{\text{M}}+N_Z\cos^2\theta_{\text{M}}\right) \end{pmatrix} \tag{2.45}$$

With the approximation that the dynamic component of magnetization is in phase with the dynamic component of the magnetic field, one can obtain Eqs. (2.46) and (2.47).

$$\mathbf{m}(t)=m_{0x}e^{i\omega t}\hat{x}+m_{0y}e^{i\omega t}\hat{y} \tag{2.46}$$

$$\mathbf{h}(t)=h_{0x}e^{i\omega t}\hat{x}+h_{0y}e^{i\omega t}\hat{y} \tag{2.47}$$

Then the term $H_{\text{int}}\mathbf{m}(t)-M_s\left(A-4\pi N\right)\cdot\mathbf{m}(t)$ can be written as Eq. (2.48).

$$H_{\text{int}}\mathbf{m}(t) - M_{\text{s}}\left(A - 4\pi N\right)\cdot\mathbf{m}(t) = \begin{pmatrix} H_x m_{0x} e^{i\omega t} \\ H_y m_{0y} e^{i\omega t} \\ \dfrac{4\pi M_{\text{s}}(N_Y - N_Z)}{2}\sin(2\theta_{\text{M}}) m_{0y} e^{i\omega t} \end{pmatrix} \tag{2.48}$$

where,

$$H_x = H_{\text{int}} + 4\pi M_{\text{s}} N_X \tag{2.49}$$

$$H_y = H_{\text{int}} + 4\pi M_{\text{s}}\left(N_Y \cos^2\theta_{\text{M}} + N_Z \sin^2\theta_{\text{M}}\right) \tag{2.50}$$

Equations (2.49) and (2.50) are defined as the stiffness fields. Finally, the Gilbert equation is cast into the form of Eq. (2.51).

$$\begin{pmatrix} \dfrac{d}{dt} m_{0x} e^{i\omega t} + |\gamma| H_y m_{0y} e^{i\omega t} - \alpha \dfrac{d}{dt} m_{0y} e^{i\omega t} \\ \dfrac{d}{dt} m_{0y} e^{i\omega t} - |\gamma| H_x m_{0x} e^{i\omega t} + \alpha \dfrac{d}{dt} m_{0x} e^{i\omega t} \\ 0 \end{pmatrix} = \begin{pmatrix} |\gamma| M_{\text{s}} h_{0y} e^{i\omega t} \\ -|\gamma| M_{\text{s}} h_{0x} e^{i\omega t} \\ 0 \end{pmatrix} \tag{2.51}$$

The ready state solution gives Eq. (2.52).

$$\begin{pmatrix} i\omega m_{0x} + |\gamma| H_y m_{0y} - \alpha i\omega m_{0y} \\ i\omega m_{0y} - |\gamma| H_x m_{0x} + \alpha i\omega m_{0x} \\ 0 \end{pmatrix} = \begin{pmatrix} |\gamma| M_{\text{s}} h_{0y} \\ -|\gamma| M_{\text{s}} h_{0x} \\ 0 \end{pmatrix} \tag{2.52}$$

The magnetic susceptibility χ is defined as a dimensionless constant that describes the degree of magnetization of a material in response to an applied magnetic field. The expression of the rf magentic susceptibility has a form of Eq. (2.53).

$$\mathbf{m} = \chi \cdot \mathbf{h} \tag{2.53}$$

For the uniform excitation mode considered in this subsection, the expression for the rf magnetic susceptibility is expressed as a 2×2 matrix given in Eq. (2.54).

$$\begin{pmatrix} m_{0x} \\ m_{0y} \end{pmatrix} = \begin{pmatrix} \chi_{xx} & -i\kappa \\ i\kappa & \chi_{yy} \end{pmatrix} \begin{pmatrix} h_{0x} \\ h_{0y} \end{pmatrix} \tag{2.54}$$

It is natural to connect Eq. (2.52) with Eq. (2.54), and the expressions for m_{0x} and m_{0y} are given as below:

$$m_{0x} = \frac{\gamma^2 H_y M_s h_{0x} + i|\gamma| M_s \alpha\omega h_{0x} - i|\gamma| M_s \omega h_{0y}}{\gamma^2 H_x H_y - \omega^2 + i\alpha\omega(|\gamma| H_x + |\gamma| H_y) - \alpha^2\omega^2} \tag{2.55}$$

$$m_{0y} = \frac{\gamma^2 H_x M_s h_{0y} + i|\gamma| M_s \alpha\omega h_{0y} + i|\gamma| M_s \omega h_{0x}}{\gamma^2 H_x H_y - \omega^2 + i\alpha\omega(|\gamma| H_x + |\gamma| H_y) - \alpha^2\omega^2} \tag{2.56}$$

It is straight forward to find the elements of the susceptibility tensor as given in Eqs. (2.57), (2.58), and (2.59).

$$\chi_{xx} = \frac{\gamma^2 H_y M_s + i|\gamma| M_s \alpha\omega}{\gamma^2 H_x H_y - \omega^2 + i\alpha\omega(|\gamma| H_x + |\gamma| H_y) - \alpha^2\omega^2} \tag{2.57}$$

$$\chi_{yy} = \frac{\gamma^2 H_x M_s + i|\gamma| M_s \alpha\omega}{\gamma^2 H_x H_y - \omega^2 + i\alpha\omega(|\gamma| H_x + |\gamma| H_y) - \alpha^2\omega^2} \tag{2.58}$$

$$\kappa = \frac{|\gamma| M_s \omega}{\gamma^2 H_x H_y - \omega^2 + i\alpha\omega(|\gamma| H_x + |\gamma| H_y) - \alpha^2\omega^2} \tag{2.59}$$

Each of the susceptibility elements is comprised of both real and imaginary parts. The real parts are related to the dispersive properties of the materials, and the imaginary parts are connected with the microwave losses in the materials. Both the real and imaginary parts of the susceptibility are strongly affected by the ferromagnetic resonance. Typically α is considered to be a small value. If the second order term of α is dropped, the simplified expressions for the susceptibility elements are given in Eqs. (2.60), (2.61), and (2.62).

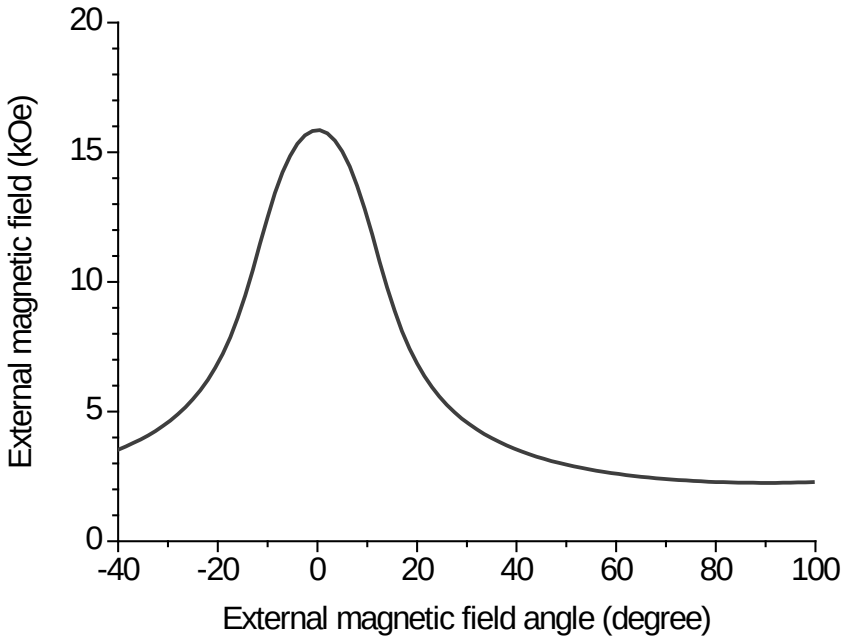

FIG. 2.8. Plot of FMR field vs. external magnetic field angle. A thin film configuration is considered in the calculations. The material has a saturation induction of 10.5 kG. The microwave frequency is fixed at 15 GHz. No anisotropy magnetic anisotropy is considered.

$$4\pi\chi_{xx} = \frac{\omega_M\left(\omega_y + i\alpha\omega\right)}{\omega_x\omega_y - \omega^2 + i\alpha\omega(\omega_x + \omega_y)} \tag{2.60}$$

$$4\pi\chi_{yy} = \frac{\omega_{\mathrm{M}}\left(\omega_x + i\alpha\omega\right)}{\omega_x\omega_y - \omega^2 + i\alpha\omega(\omega_x + \omega_y)} \tag{2.61}$$

$$4\pi\kappa = \frac{\omega_{\mathrm{M}}\omega}{\omega_x\omega_y - \omega^2 + i\alpha\omega(\omega_x + \omega_y)} \tag{2.62}$$

where $\omega_{\mathrm{M}} = |\gamma| 4\pi M_s$, $\omega_x = |\gamma| H_x$, and $\omega_y = |\gamma| H_y$. ω_x and ω_y are the stiffness frequencies. The so-called on resonance condition happens when $\omega_x\omega_y - \omega_0^2 = 0$ is satisfied.

The FMR frequency is obtained by the substitute of the stiffness fields as given in Eq.

(2.63).

$$\omega_0 = |\gamma| \sqrt{\left[H_{\text{ext}} \cos(\theta_{\text{H}} - \theta_{\text{M}}) - 4\pi M_{\text{s}} (N_Y \sin^2 \theta_{\text{M}} + N_Z \cos^2 \theta_{\text{M}}) + H_{\text{A}} \cos^2 \theta_{\text{M}} \right]} \cdot \sqrt{A + 4\pi M_{\text{s}} \left(N_Y \cos^2 \theta_{\text{M}} + N_Z \sin^2 \theta_{\text{M}} \right)} \qquad (2.63)$$

$$A = H_{\text{ext}} \cos(\theta_{\text{H}} - \theta_{\text{M}}) - 4\pi M_{\text{s}} (N_Y \sin^2 \theta_{\text{M}} + N_Z \cos^2 \theta_{\text{M}}) + H_{\text{A}} \cos^2 \theta_{\text{M}}$$

On the other hand, once the FMR frequency is fixed, Eq. (2.63) gives a single solution for the external magnetic field, which is called the FMR field. A plot of FMR field vs. external magnetic field angle is shown in Fig. 2.8. FMR experiments involve the measurement of the microwave power absorbed by the sample, and the profile of the microwave power absorption depends on the microwave loss in the material. As mentioned above that the imaginary parts are connected with the microwave losses in the materials. So the time-averaged microwave power $\langle P \rangle$ absorbed by the sample is connected with the imaginary part of the magnetic susceptibility (χ''_{xx}) as shown in Eq. (2.64).

$$\langle P \rangle = \frac{1}{2} \omega h_{0x}^2 \chi''_{xx} \qquad (2.64)$$

The expression of the imaginary part of χ_{xx} can be determined from Eq. (2.60), which is given in Eq. (2.65).

$$\text{Im}(4\pi\chi_{xx}) = \frac{-\alpha\omega\omega_{\text{M}} \left(\omega^2 + \omega_y^2 \right)}{\left(\omega_x \omega_y - \omega^2 \right)^2 + \left[\alpha\omega(\omega_x + \omega_y) \right]^2} \qquad (2.65)$$

The microwave power absorption profile can be measured by sweeping the microwave frequency at a fixed magnetic field or sweeping the magnetic field at a fixed microwave frequency, as shown schematically in Fig. 2.3. The half-power linewidth of the absorption curve can be expressed in both frequency and magnetic field units. Equation (2.66) gives the

approximate expression for the frequency linewidth which is obtained with Eq. (2.65).

$$\Delta\omega = \alpha(\omega_x + \omega_y) \tag{2.66}$$

The FMR linewidth is widely used for characterizing the microwave loss of materials. Usually a large FMR linewidth means large microwave loss, and vice versa. Equation (2.66) indicates that the microwave losses are related to the Gilbert damping constant and the resonance frequency. If no relaxations exist, for uniform excitation mode the time dependence of $\mathbf{m}$ is governed by $e^{i\omega_0 t}$, which means that the magnetization is precessing at a given FMR frequency (ω_0) and the precession will last even without any assistances from external driven forces. However, that is not the case for real materials where the precession always has a non-zero decay rate and finally vanishes if no external drives exist. So the time dependence of $\mathbf{m}$ is usually expressed in the terms of Eq. (2.67), where η is the relaxation rate.

$$\mathbf{m}(t) = \mathbf{m}e^{i\omega t}e^{-\eta t} = \mathbf{m}e^{i(\omega + i\eta)t} \tag{2.67}$$

The relation between the frequency-swept FMR linewidth and the relaxation rate is written in Eq. (2.68).

$$\Delta\omega = 2\eta \tag{2.68}$$

With Eq. (2.66), the relaxation rate can be expressed in terms of Gilbert damping constant in the form of Eq. (2.69).

$$\eta = \frac{\alpha\left(\omega_x + \omega_y\right)}{2} \tag{2.69}$$

Equation (2.70) gives the approximate expression for the field-swept FMR linewidth,

$$\Delta H = \frac{\Delta\omega}{|\gamma|\left.\frac{\partial\omega_0}{\partial|\gamma|H_{\text{ext}}}\right|_{\text{FMR}}} = \frac{\alpha(\omega_x+\omega_y)}{|\gamma|\left.\frac{\partial\omega_0}{\partial|\gamma|H_{\text{ext}}}\right|_{\text{FMR}}} = \frac{2\eta}{|\gamma|P_{\text{A}}} \tag{2.70}$$

where H_{ext} is the external magnetic field, and the ellipticity factor P_A provides a convenient way to account for the ellipticity of the FMR response in the relaxation rate and FMR linewidth analyses. Equation (2.71) gives the expression of the ellipticity factor.

$$P_{\text{A}}(\omega_0) = \left.\frac{\partial\omega_0}{\partial|\gamma|H_{\text{ext}}}\right|_{\text{FMR}} = \frac{\omega_x+\omega_y}{2\omega_0} \tag{2.71}$$

With the connection between the frequency-swept FMR linewidth ($\Delta\omega$) and the Gilbert damping constant α shown in Eq. (2.66), the field-swept FMR linewidth ΔH can be written as Eq. (2.72).

$$\Delta H(\omega_0) = \frac{\alpha(\omega_x+\omega_y)}{|\gamma|P_{\text{A}}(\omega_0)} = \frac{2\alpha\omega_0}{|\gamma|} \tag{2.72}$$

One can see that the field-swept FMR linewidh is proportional to the Gilbert damping constant and has a linear dependence on the FMR frequency. Equation (2.72) gives an important result and will be discussed frequently in this thesis.

2.6 Non-uniform magnetization precession modes

The concept of spin waves will be introduced in this subsection, and relevant working equations are developed (Patton 1976). Spin waves may be considered as a collective motion of non-uniform magnetization precessions with continuous symmetry. Unlike the uniform magnetization precession, spatial variations are added into the dynamic component of magnetization. There exist standing spin waves and propagation spin waves, and both have

been observed in various magnetic materials. In the semi-classical perspective, the spin waves are treated with the consideration of the spin-spin interactions. Spin waves are known as magnons in the view of equivalent quasi-particles. Since the spatial dependence of the magnetization is included, one can have the magnetization written as Eq. (2.73).

$$\mathbf{M}(\mathbf{r},t) = M_s\hat{\mathbf{z}} + \mathbf{m}(\mathbf{r},t) \tag{2.73}$$

The magnetization spatial dependence is contributed by the dynamic component $\mathbf{m}(\mathbf{r},t)$ which can be expended in terms of orthogonal plane waves as Eq. (2.74).

$$\mathbf{m}(\mathbf{r},t) = m_0 e^{i\omega_0 t}\hat{\mathbf{x}} + \sum_{k\neq 0} m_k e^{i(\omega_{\mathbf{k}} t + \mathbf{k}\cdot\mathbf{r})}\hat{\mathbf{x}} \tag{2.74}$$

The uniform precession mode can be treated as a special spin-wave mode with a zero wavenumber ($\mathbf{k} = 0$). The non-uniform precession modes are the spin-wave modes with non-zero wavenumbers ($\mathbf{k} \neq 0$).

In the magnetostatic approximation, currents are steady (no time dependence) and the Maxwell's equations have the form of Eq. (2.75).

$$\begin{aligned} \nabla \times \mathbf{h}_i &\approx 0 \\ \nabla \cdot (\mathbf{h}_i + \mathbf{m}) &= 0 \end{aligned} \tag{2.75}$$

The magnetostatic approximation can also be taken as that the induced electric fields are negligible. The torque equation of spatial dependent magnetization precession is developed under the magnetostatic approximation. The excited non-uniform magnetization precessions are considered as magnetostatic spin waves.

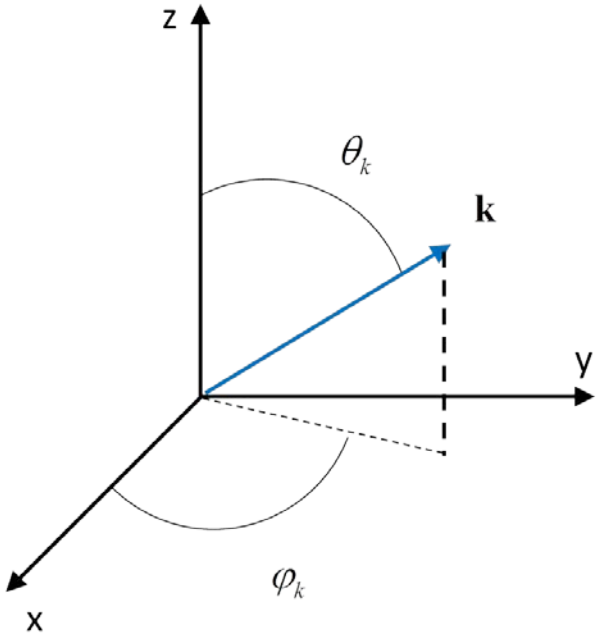

FIG. 2.9. The configuration of spin-wave propagation in the precession frame. The blue arrow shows the spin-wave propagation direction, and $\mathbf{k}$ is the wavenumber of the spin wave. The polar angle between the spin-wave propagation direction and the z axis is defined as θ_k. The azimuth angle is defined as the angle between the $\mathbf{k}$ projection in the $x-y$ plane. The internal magnetic field direction is chosen to be the z axis. The angle between the internal magnetic field and the Z axis is θ_M (see Fig. 2.7). The magnetization precesses around the principle axis of the internal magnetic field. And the dynamic component of the magnetization lies in the $x-y$ plane.

$$\frac{d}{dt}\left[M_s\hat{z}+\mathbf{m}_0e^{i\omega_0t}+\sum_{k\neq0}\mathbf{m}_ke^{i(\omega_\mathbf{k}t+\mathbf{k}\cdot\mathbf{r})}\right]=-|\gamma|\left[M_s\hat{z}+\mathbf{m}_0e^{i\omega_0t}+\sum_{k\neq0}\mathbf{m}_ke^{i(\omega_\mathbf{k}t+\mathbf{k}\cdot\mathbf{r})}\right]$$
$$\times\left[H_{\text{int}}\hat{z}+(A-4\pi N)\cdot\left(M_s\hat{z}+\mathbf{m}_0e^{i\omega_0t}+\sum_{k\neq0}\mathbf{m}_ke^{i(\omega_\mathbf{k}t+\mathbf{k}\cdot\mathbf{r})}\right)+(h_{0x}\hat{x}+h_{0y}\hat{y})e^{i\omega t}\right] \tag{2.76}$$

The expression of the propagation wavenumber $\mathbf{k}$ in the precession frame is given in Eq. (2.77). The azimuth angle and polar angle of the wavenumber $\mathbf{k}$ are defined in Fig. 2.9.

$$\begin{pmatrix} k_x \\ k_y \\ k_z \end{pmatrix} = \begin{pmatrix} k\sin\theta_k\cos\phi_k \\ k\sin\theta_k\sin\phi_k \\ k\cos\theta_k \end{pmatrix} \tag{2.77}$$

The frequency of a spin wave can be derived in the same manner as the derivation of FMR frequency. The spin-wave frequency is written as Eq. (2.78).

$$\begin{aligned} \omega_k &= |\gamma|\sqrt{A\cdot(H_{\text{int}} + 4\pi M_{\text{s}} N_X) - 4\pi M_{\text{s}} H_{\text{A}} \sin^2\theta_{\text{M}} \sin^2\theta_k \cos^2\phi_k} \\ A &= H_{\text{int}} + 4\pi M_{\text{s}}\left(N_Y \cos^2\theta_{\text{M}} + N_Z \sin^2\theta_{\text{M}}\right)\sin^2\theta_k - H_{\text{A}}\sin^2\theta_{\text{M}} \end{aligned} \tag{2.78}$$

The spin-wave frequency expression also unveils the dispersion relation. For example, consider a magnetic thin film with the external magnetic field orientated in the film plane. If $H_{\text{ext}} = 2251$ Oe, $H_{\text{a}}=0$, $4\pi M_s = 10.5$ kG, and $|\gamma| = 2\pi \cdot 2.8$ MHz/Oe, one obtains a spin-wave manifold shown in Fig. 2.10. The upper branch is formed by the spin-wave mode with its wave vector perpendicular to the internal magnetic field, and the lower branch is formed by the spin-wave mode with its wave vector parallel to the internal magnetic field. The two branches are parallel with the wavenumber axis since no spin-spin interactions are included. Just keep in mind that the parameters used in this spin wave manifold example will be applied to all the spin wave manifold calculations in the later discussions.

The spin-wave manifold calculated with Eq. (2.78) corresponds to the simplest consideration in which no spin-spin exchange interactions and dipolar interactions are involved. To consider the exchange interactions, one introduces the exchange magnetic field $\mathbf{h}_{\text{ex}}$, which is an effective

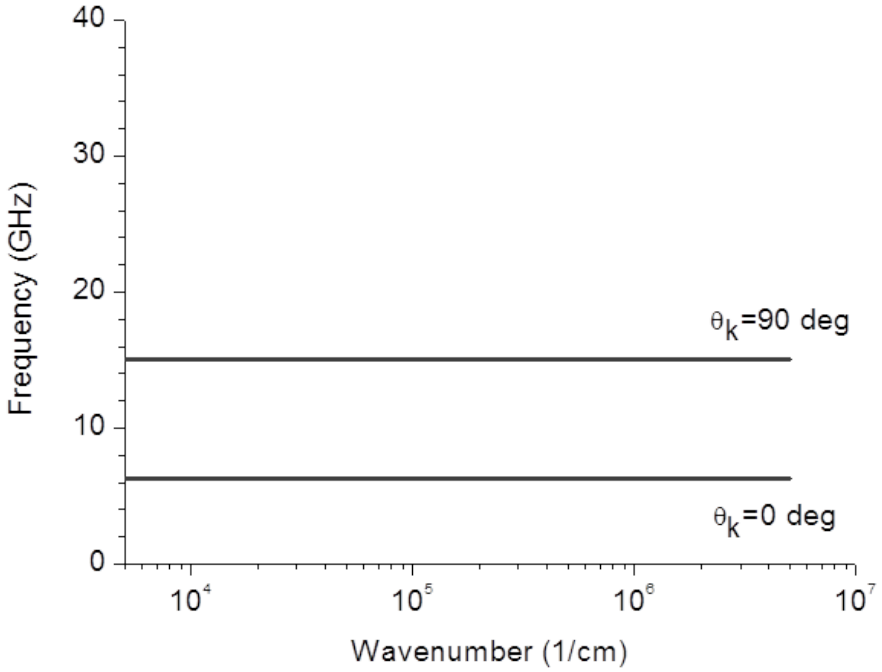

FIG. 2.10. Spin-wave manifold without considering spin-spin exchange interactions. The upper branch indicates the spin-wave mode whose propagation direction is perpendicular to the internal magnetic field. The lower branch shows the spin-wave mode whose propagation direction is parallel to the internal magnetic field. The area between the two branches is formed by the spin-wave modes with the propagation angles between 0 deg and 90 deg. Note that the spin-wave frequency is independent of the spin-wave wavenumber.

magnetic field that tends to align adjacent magnetic moments. The exchange magnetic field can be written as

$$\mathbf{h}_{\text{ex}}(\mathbf{r},t) = \frac{D}{M_{\text{s}}}\nabla^2\mathbf{m}(\mathbf{r},t) \tag{2.79}$$

where D is the exchange constant, which has the unit of $\text{Oe}\times\text{cm}^2/\text{rad}^2$.

Fourier transform of Eq. (2.79) has the form of Eq. (2.80).

$$\mathbf{h}_{\text{ex}}(t) = -\frac{D}{M_{\text{s}}}\nabla^2\mathbf{m}_{\mathbf{k}}(t) = -4\pi N_{\text{ex}} \cdot \mathbf{m}_{\mathbf{k}}(t) \tag{2.80}$$

$$N_{\text{ex}} = \frac{Dk^2}{4\pi M_{\text{s}}}\begin{pmatrix} 1 & 0 & 0 \\ 0 & 1 & 0 \\ 0 & 0 & 1 \end{pmatrix} \tag{2.81}$$

where $k = |\mathbf{k}|$ is the amplitude of the wave vector **k**. The exchange field can be treated as a new term of magnetic field, which directly contributes to the spin-wave dispersion relation. The spin-wave dispersion with the exchange field taken into account can be expressed as Eq. (2.82).

$$\begin{aligned} \omega_k &= |\gamma|\sqrt{(H_{\text{int}} + Dk^2 + 4\pi M_{\text{s}}N_X) - 4\pi M_{\text{s}}H_{\text{A}}\sin^2\theta_{\text{M}}\sin^2\theta_k\cos^2\phi_k} \\ A &= H_{\text{int}} + Dk^2 + 4\pi M_s\left(N_Y\cos^2\theta_{\text{M}} + N_Z\sin^2\theta_{\text{M}}\right)\sin^2\theta_k - H_{\text{A}}\sin^2\theta_{\text{M}} \end{aligned} \tag{2.82}$$

Using the same parameters for the calculations of the curves shown in Fig. 2.10 and taking the exchange constant value as $D = 2.394\cdot10^{-9}\,\text{Oe}\times\text{cm}^2/\text{rad}^2$, the spin-wave manifold with the exchange interactions is calculated and is shown in Fig. 2.11.

Under the magentostatic approximation, the dipolar magnetic field $\mathbf{h}_{dip}$ caused by the accumulation of surface and volume magnetic charges can be calculated from the Maxwell equations.

$$\begin{aligned} \nabla\times\mathbf{h}_{\text{dip}}(\mathbf{r},t) &= 0 \\ \nabla\cdot\mathbf{h}_{\text{dip}}(\mathbf{r},t) &= -4\pi\nabla\cdot\mathbf{m}(\mathbf{r},t) \end{aligned} \tag{2.83}$$

The Fourier transform for a magnetic thin film yields Eq. (2.84).

$$\mathbf{h}_{\text{dip}}(t) = -4\pi N_{\text{dip}} \cdot \mathbf{m}_{\mathbf{k}}(t) \tag{2.84}$$

The tensor N_{dip} in Eq. (2.84) has the form of Eq. (2.85) (Kalarickal 2006).

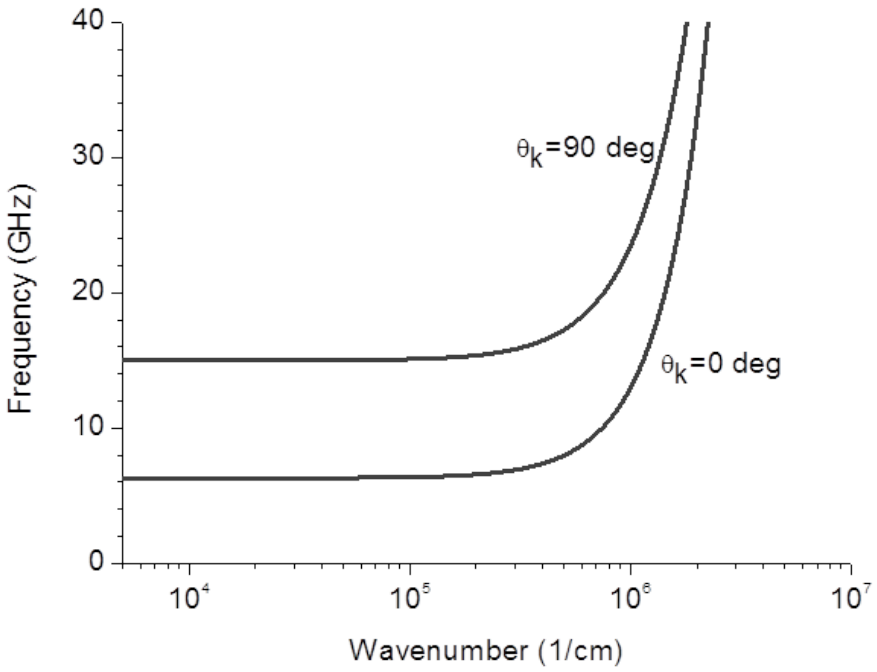

FIG. 2.11. Spin-wave manifold with spin-spin exchange interactions considered. The upper branch indicates the spin-wave mode with its propagation direction perpendicular to the internal magnetic field. The lower branch shows the spin-wave mode with its propagation direction parallel to the internal magnetic field. The area between the two branches is formed by the spin-wave modes with the propagation angle relative the field direction between 0 deg and 90 deg. The spin-wave frequency is dependent on the wavenumber. The dramatic increase of the spin-wave frequency in the high-wavenumber region is due to the significant increase of the exchange magnetic field.

$$N_{\text{dip}} = \begin{pmatrix} n_{xx} & n_{xy} & n_{xz} \\ n_{yx} & n_{yy} & n_{yz} \\ n_{zx} & n_{zy} & n_{zz} \end{pmatrix} \tag{2.85}$$

The explicit expressions for the elements in Eq. (2.85) are given in Eq. (2.86).

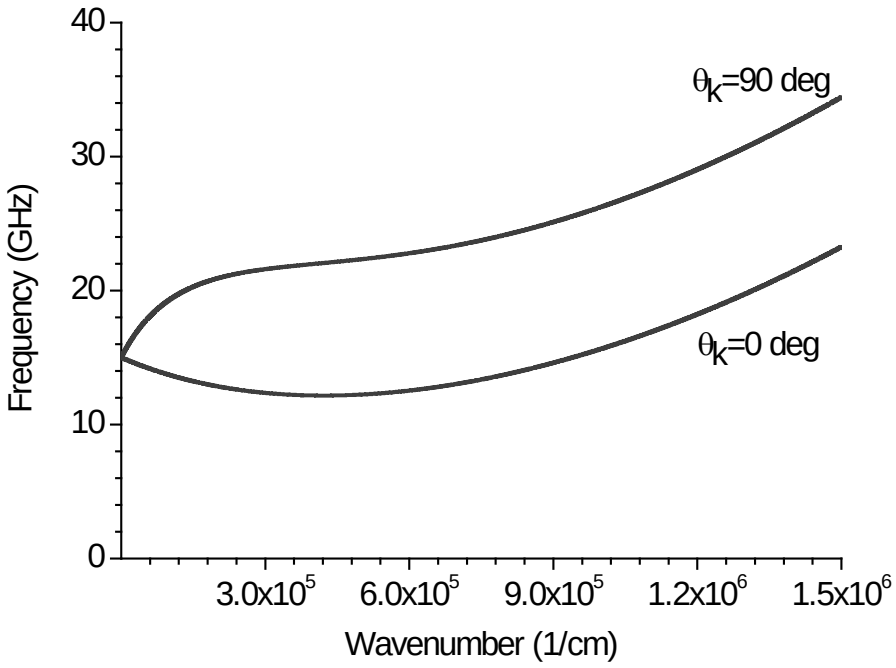

FIG. 2.12. Spin-wave manifold with spin-spin exchange interactions and dipolar interactions considered. The upper branch indicates the spin-wave mode with its propagation direction perpendicular to the internal magnetic field. The lower branch shows the spin-wave mode with its propagation direction parallel to the internal magnetic field. The area between the two branches is formed by the spin-wave modes with the propagation angles between $0\ \text{deg}$ and $90\ \text{deg}$. The cross point between the two branches at the y axis corresponds to the FMR mode ($k = 0$).

$$
\begin{aligned}
n_{xx} &= (1-N_k)\cos^2\theta_{\mathrm{M}}\cos^2\theta_k + N_k\sin^2\theta_{\mathrm{M}} \\
n_{yy} &= (1-N_k)\sin^2\theta_k \\
n_{zz} &= (1-N_k)\sin^2\theta_{\mathrm{M}}\cos^2\theta_k + N_k\cos^2\theta_{\mathrm{M}} \\
n_{xy} &= n_{yx} = (1-N_k)\cos\theta_{\mathrm{M}}\sin\theta_k\cos\theta_k \\
n_{xz} &= n_{zx} = \left[(1-N_k)\cos^2\theta_k - N_k\right]\sin\theta_{\mathrm{M}}\cos\theta_{\mathrm{M}} \\
n_{yz} &= n_{zy} = (1-N_k)\cos\theta_{\mathrm{M}}\sin\theta_k\cos\theta_k
\end{aligned}
\tag{2.86}
$$

N_k is called the Harte dipolar factor. For a magnetic thin film, this factor is given as Eq. (2.87).

$$N_k = \frac{(1-e^{-kd})}{kd} \quad (N_k = 1,\ if\ \ k \cdot d = 0) \tag{2.87}$$

where d is the thickness of the film. Taken the dipolar magnetic field into account, the spin-wave dispersion relation can be written by Eq. (2.88).

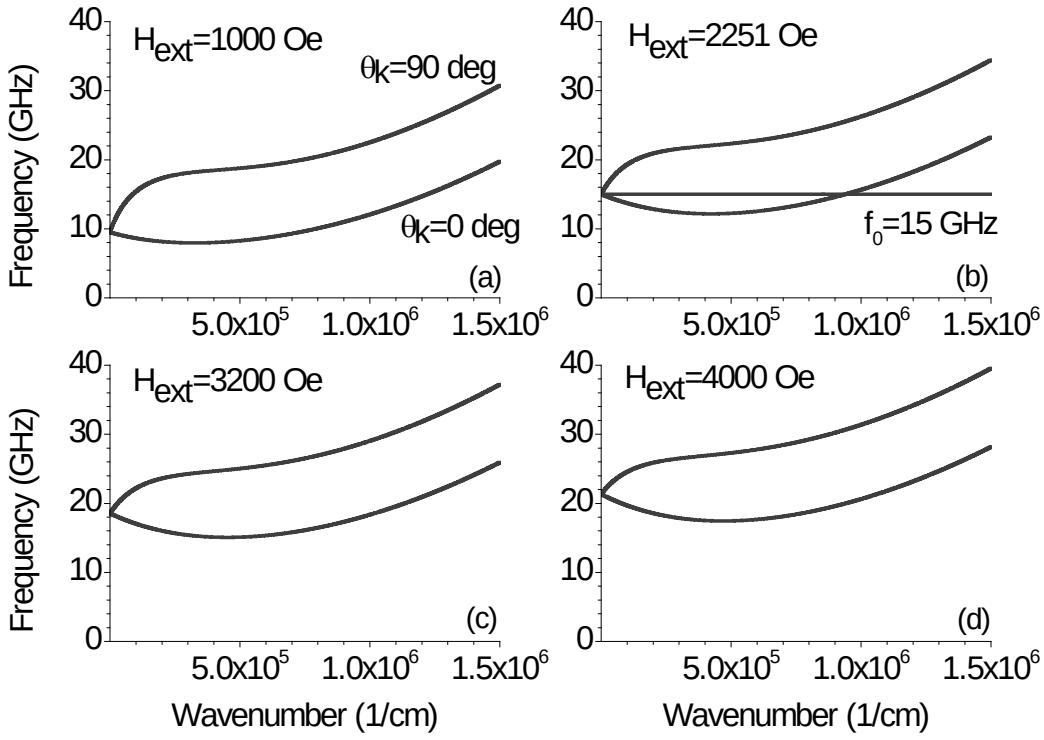

FIG. 2.13. Spin-wave manifolds at different external magnetic fields. In graph (b), the horizontal line indicates the FMR frequency which is 15 GHz. The cross between the spin-wave manifold and the 15 GHz line indicates the available spin-wave modes at the FMR frequency.

$$\omega_k = |\gamma| \sqrt{A \cdot (H_{\text{int}} + Dk^2 + 4\pi M_s N_k + 4\pi M_s N_X) - 4\pi M_s H_A \sin^2\theta_M \sin^2\theta_k \cos^2\phi_k}$$
$$A = H_{\text{int}} + Dk^2 + 4\pi M_s (1 - N_k) \sin^2\theta_k + 4\pi M_s \left(N_Y \cos^2\theta_M + N_Z \sin^2\theta_M\right) \sin^2\theta_k \quad (2.88)$$
$$- H_A \sin^2\theta_M$$

Using the same parameters for the calculation of the curves shown in Fig. 2.10 and taking 50 nm as the film thickness, the spin-wave manifold is calculated and is shown in Fig. 2.12.

So far the spin-wave dispersion relation with the consideration of the exchange magnetic field and the dipolar magnetic field has been developed. The uniform magnetization precession can be treated as a special case of spin waves, a spin wave with the wavenumber equal to zero. From the spin-wave manifold profiles, one can tell that spin waves have a very broad operation frequency for a fixed external magnetic field. The spin-wave manifold shifts to a higher frequency region as the external magnetic field increases, as shown in Fig. 2.13. The horizontal solid line in Fig. 2.13 (b) indicates the FMR frequency, which is 15 GHz. The cross between the spin-wave manifold and the solid line indicates the available spin-wave state at the FMR frequency. Defects, voids, grain boundaries, and magnetic property variations among grains can couple the uniform precession (FMR mode) to the degenerate spin waves. Such coupling between the FMR mode and the spin wave mode can lead to a broadening of the measured FMR profile and an increase in the measured FMR linewidth.

In this thesis, the measured FMR linewidths are considered to have three main components: Gilbert damping, relaxation due to two-magnon scattering, and inhomogeneity line broadening. The Gilbert damping contribution originates from the phenomenological relaxation of magnetization precession and is often classified as the intrinsic damping. The two-magnon

scattering originates from the coupling between the FMR mode and the spin-wave mode, which is an extrinsic damping. Both the intrinsic and extrinsic damping contributes to the magnetization relaxation process. The inhomogeneity line broadening contribution originates from the magnetic property variations among different regions of the sample. This contribution to the FMR linewidth is not a damping. Efforts have been made to separate these contributions from the measured FMR linewidth in the following chapters.

CHAPTER 3. FERROMAGNETIC RELAXATIONS IN METALLIC THIN FILMS

3.1 Two-magnon scattering concept and relaxation rate

The concept of coupling between the uniform magnetization precession (the FMR mode) and the non-uniform magnetization precession (the spin-wave mode) has been briefly introduced in Chapter 2. Defects, inhomogeneity, boundaries and etc. can act as scatters to lead the energy transfer from the uniform magnetization precession into degenerate spin waves. Such transfer of energy demonstrates itself as the annihilation of a zero-wavenumber magnon and the creation of a nonzero-wavenumber magnon. The consequence of this process is that the magnetization precession undergoes rapid relaxation. This process is the so-called two-magnon scattering (TMS) process. It is an extrinsic damping and contributes to the FMR linewidth (Sparks 1964, Patton 1972, Schlömann 1958, 1969, 1970, Vrehen 1969, Hurben and Patton 1998).

The scatters produce non-uniform field distributions which create perturbations on the uniform magnetization precession and thereby trigger the TMS process when there are available degenerate spin-wave states at the resonance frequency. As shown in Fig. 3.1, the available degenerate spin-wave states are indicated by the crossing between the spin-wave manifolds and the 15 GHz solid lines. The amount of the available degenerate spin-wave states depends on the external magnetic field orientation, and it generally decreases as the external magnetic field orientates more close to the film normal direction. In fact, there are no available degenerate spin-wave states at the out-of-plane external magnetic field configuration, as indicated in Fig. 3.1 (d). One can simply draw the conclusion that the intrinsic damping could be characterized

under the out-of-plane external magnetic field configuration where the TMS is absent. This chapter mainly discusses the dominate TMS processes in metallic thin films, including grain-to-grain TMS and grain-boundary TMS. The grain-to-grain TMS process is usually caused by randomly orientated anisotropy among grains. Both the classical and quantum models of the TMS process associated with random anisotropy scattering in metallic thin films has been established previously (Celinski 1991, Heinrich 2002, McMichael 2004, Woltersdorf 2004, Krivosik 2007). In the grain-boundary TMS model, the grain boundaries are considered to have uniaxial magnetic anisotropy, and the scattering process is caused by the anisotropy scattering at the grain boundaries. The grain-boundary TMS model has already been developed from the classical perspective (Mo 2008). It should be noted that very often the TMS is a non-negligible contribution to the measured FMR linewidth and is widely used to explain the non-linear frequency dependence of the FMR linewidth in metallic thin films.

The development of the TMS-produced relaxation rate is based on the simple assumption that the relaxation rate of spin waves is very fast, with the limit of Eq. (3.1).

$$\eta_{\mathbf{k}} \to 0 \tag{3.1}$$

In other words, it is considered that the non-zero wavenumber magnon annihilates as soon as it is created. Thus, the TMS relaxation directly contributes to the relaxation of the uniform magnetization precession. The general expression of the relaxation rate for the TMS is written as Eq. (3.2).

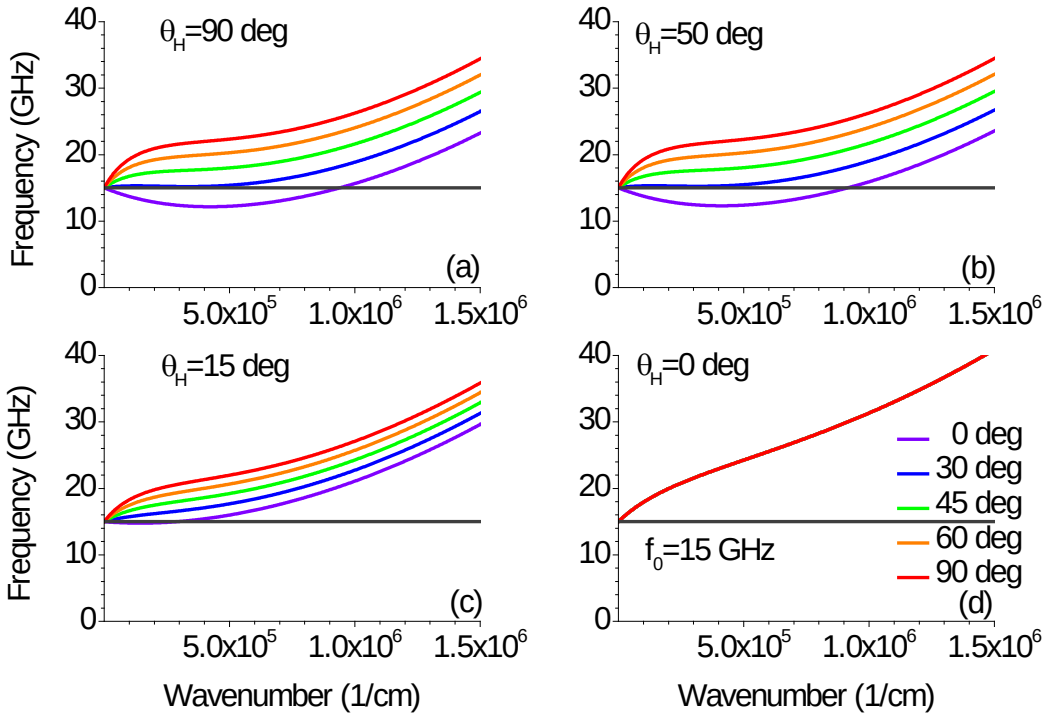

FIG. 3.1. Spin wave manifold under different external magnetic field orientations. (a) Spin wave manifold under in-plane external magnetic field. (b) Spin wave manifold under the external magnetic field pointing 50 degree off from the film normal direction. (c) Spin wave manifold under the external magnetic field pointing 15 degree off from the film normal direction. (d) Spin wave manifold under out-of-plane external magnetic field. The colored lines are calculated with different spin wave propagation directions as indicated in graph (d). The cross section between the spin wave manifold and FMR frequency line gets smaller as the external magnetic field angle decreases, as shown in graph (a), (b), and (c). The spin wave manifold only crosses with the FMR frequency line at the y-axis, which indicates no degenerate spin wave state is available when the external magnetic field is normal to the film plane, thus the two-magnon scattering process is suppressed.

$$\eta_{\mathrm{TMS}} \approx \pi \sum_{\mathbf{k}} \left| G_{0,\mathbf{k}} \right|^2 \delta\left(\omega_0 - \omega_{\mathbf{k}}\right) \tag{3.2}$$

This formula is close to the two-magnon transition probabilities developed from Fermi's golden rule. The coupling factor $\left|G_{0,\mathbf{k}}\right|^2$ descripts the coupling strength between the uniform mode and the degenerate spin-wave modes, which is given in Eq. (3.3).

$$\left|G_{0,\mathbf{k}}\right|^2 = \frac{\left|\gamma\right|^4 C_{\mathbf{k}}}{4\omega_{\mathbf{k}}\omega_0}\left\{\begin{array}{l}\left\langle h_{xx}^2\right\rangle H_{yy,\mathbf{k}}H_{yy,0} + \left\langle h_{yy}^2\right\rangle H_{xx,\mathbf{k}}H_{xx,0} + 2\left\langle h_{xx}h_{yy}\right\rangle\left(\frac{\omega_{\mathbf{k}}\omega_0}{\left|\gamma\right|^2} + H_{xy,\mathbf{k}}H_{xy,0}\right) \\ + \left\langle h_{xy}^2\right\rangle\left[H_{xx,\mathbf{k}}H_{yy,0} + H_{yy,\mathbf{k}}H_{xx,0} - 2\left(\frac{\omega_{\mathbf{k}}\omega_0}{\left|\gamma\right|^2} + H_{xy,\mathbf{k}}H_{xy,0}\right)\right]\end{array}\right\} \tag{3.3}$$

where $C_{\mathbf{k}}$ is the Fourier transform of the appropriate correlation factor $C(\mathbf{r}) = e^{\frac{-|\mathbf{r}|}{\xi}}$. The individual scatter is assumed to have a correlation length of ξ. In this thesis, the correlation length is considered to be close to the average grain size. $C_{\mathbf{k}}$ is expressed in Eq. (3.4).

$$C_{\mathbf{k}} \equiv C(k) = \frac{1}{A}\frac{2\pi\xi^2}{\left[1+(k\xi)^2\right]^{\frac{3}{2}}} \tag{3.4}$$

The fields h_{xx}, h_{yy}, and h_{xy} in Eq. (3.3) are the perturbation stiffness fields which are model dependent. The stiffness fields for the uniform mode and the spin-wave mode are expressed as the following.

$$H_{xx,0} = H_{\text{int}} \tag{3.5}$$

$$H_{yy,0} = H_{\text{int}} + 4\pi M_{\text{s}}\sin^2\theta_{\text{M}} \tag{3.6}$$

$$H_{xy,0} = 0 \tag{3.7}$$

$$H_{xx,k} = H_{\text{int}} + Dk^2 + 4\pi M_{\text{S}}[(1-N_{\text{k}})\cos^2(\theta_{\text{M}})\cos^2(\theta_{\text{k}}) + N_{\text{k}}\sin^2(\theta_{\text{M}})] \tag{3.8}$$

$$H_{yy,k} = H_{\text{int}} + Dk^2 + 4\pi M_{\text{S}}(1-N_{\text{k}})\sin^2(\theta_{\text{k}}) \tag{3.09}$$

$$H_{xy,\mathrm{k}} = 4\pi M_{\mathrm{S}}(1-N_{\mathrm{k}})\cos(\theta_{\mathrm{k}})\sin(\theta_{\mathrm{k}})\cos(\theta_{\mathrm{M}}) \tag{3.10}$$

and,

$$H_{\mathrm{int}} = H_{\mathrm{ext}}\cos(\theta_{\mathrm{H}}-\theta_{\mathrm{M}}) - 4\pi M_{\mathrm{s}}(N_Y \sin^2\theta_{\mathrm{M}} + N_Z\cos^2\theta_{\mathrm{M}}) + H_{\mathrm{A}}\cos^2\theta_{\mathrm{M}} \tag{3.11}$$

where $\omega_0 = |\gamma|\sqrt{H_{xx,0}H_{yy,0}}$ and $\omega_k = |\gamma|\sqrt{H_{xx,k}H_{yy,k} - H_{xy,k}^2}$.

For thin film geometry, only spin waves propagating in the film plane are considered. If one assumes the excited spin waves to be planar waves, the summation in Eq. (3.2) can be converted as

$$\sum_{\mathbf{k}} \rightarrow \iint d^2k \tag{3.12}$$

The delta function in Eq. (3.2) describes the conservation of energy in the TMS process. Namely, only the spin waves at the FMR frequency can be excited through the TMS process. Thus, the delta function can be written as

$$\delta(\omega_0-\omega_k) = \begin{cases} \dfrac{1}{\Delta\omega_k}, & \text{if } |\omega_0-\omega_k| \le \dfrac{1}{2}\Delta\omega_M \\ 0, & \text{otherwise} \end{cases} \tag{3.13}$$

The following formula shows the approximation to the integration of the delta function, which is also named as the available density of degenerate spin wave states,

$$\iint \delta(\omega_0-\omega_k)d^2k = \iint \frac{1}{\Delta\omega_k}\theta_k d\theta_k dk = 4\int_0^{k_{\max}}\int_{\theta_{k\min}}^{\theta_{k\max}} \frac{1}{\Delta\omega_k}\theta_k d\theta_k dk = 4\int_0^{k_{\max}} \frac{\theta_{k\max}-\theta_{k\min}}{\Delta\omega_k}dk \tag{3.14}$$

Since the spin-wave relaxation is assumed to be very fast, $\Delta\omega_k$ is a small number. Thus, Eq. (3.14) can be further simplified as Eq. (3.15).

$$\iint \delta(\omega_0-\omega_k)d^2k = 4\int_0^{k_{\max}} \frac{\partial\theta_k}{\partial\omega_k}kdk \tag{3.15}$$

$$\frac{\theta_{k\max} - \theta_{k\min}}{\Delta\omega_k} \approx \frac{\partial\theta_k}{\partial\omega_k} \tag{3.16}$$

As a result, the general expression for the TMS relaxation rate in metallic thin films is written as Eq. (3.17)

$$\eta_{TMS} = 4\pi \int_0^{k_{\max}} \left|G_{0,\mathbf{k}}\right|^2 \frac{\partial\theta_k}{\partial\omega_k} k dk \tag{3.17}$$

The TMS process contributes to the measured FMR linewidth, which may broaden the FMR profile significantly. Theoretically, the TMS has a Lorentzian linewidth contribution which is the same as the Gilbert damping linewidth contribution. Two types of TMS processes are going to be specifically discussed in the following subsections: grain-to-grain TMS and grain-boundary TMS.

3.2 Grain-to-grain two-magnon scattering

The grain-to-grain TMS has been observed in many metallic thin films. It arises from the random grain-to-grain fluctuations in the properties, such as the effective crystalline magnetic anisotropy field direction, of polycrystalline thin films. The expression for the grain-to-grain TMS relaxation rate is given in Eq. (3.18).

$$\eta_{\mathrm{GG}} = 2\left|\gamma\right|^2 \xi^2 H_{\mathrm{A}}^2 \int_0^{k_{\max}} \Lambda_{\mathrm{GG}}\ C_{\mathrm{GG}}\ D\ dk \tag{3.18}$$

where Λ_{GG} is the ellipticity function, C_{GG} is the correlation function, and D is the density of state function. The ellipticity function has the explicate form of Eq. (3.19). The values for the averaging coefficients for the anisotropy direction variation are listed in table 3.1

$$\Lambda_{GG} = c_1 \frac{1}{\sqrt{\frac{H_{xx,k}}{H_{yy,k}} - \frac{H_{xy,k}^2}{H_{yy,k}^2}}} \frac{\sqrt{H_{yy,0}}}{\sqrt{H_{xx,0}}} + c_2 \frac{1}{\sqrt{\frac{H_{yy,k}}{H_{xx,k}} - \frac{H_{xy,k}^2}{H_{xx,k}^2}}} \frac{\sqrt{H_{xx,0}}}{\sqrt{H_{yy,0}}}$$
$$+ c_3 \left(\frac{1}{\sqrt{\frac{H_{yy,k}}{H_{xx,k}} - \frac{H_{xy,k}^2}{H_{xx,k}^2}}} \frac{\sqrt{H_{yy,0}}}{\sqrt{H_{xx,0}}} + \frac{1}{\sqrt{\frac{H_{xx,k}}{H_{yy,k}} - \frac{H_{xy,k}^2}{H_{yy,k}^2}}} \frac{\sqrt{H_{xx,0}}}{\sqrt{H_{yy,0}}} \right) + c_4 \tag{3.19}$$

Table 3.1 Average coefficients for anisotropy direction variation

Coefficient	c_1	c_2	c_3	c_4
In-plane uniaxial	1/2	3/8	0	1/2
First order cubic	29/105	29/105	3/35	1/105

The correlation function in Eq. (3.18) has the expression of Eq. (3.20).

$$C_{\mathrm{GG}} = \frac{1}{\left[1+\left(k\xi\right)^2\right]^{\frac{3}{2}}} \tag{3.20}$$

where ξ is the average grain size. The density of state function has been introduced in the previous subsection, and it is written as Eq. (3.21).

$$D = \frac{\partial \theta_k}{\partial \omega_k} k \tag{3.21}$$

The grain-to-grain TMS relaxation rate can be converted into the form of the FMR linewidth through Eq. (3.22), which has been introduced in Chapter 2.

$$\Delta H_{\mathrm{GG}} = \frac{2\eta_{\mathrm{GG}}}{\left|\gamma\right| P_{\mathrm{A}}} \tag{3.22}$$

Thus the FMR linewidth contribution from the grain-to-grain TMS can be written as Eq. (3.23).

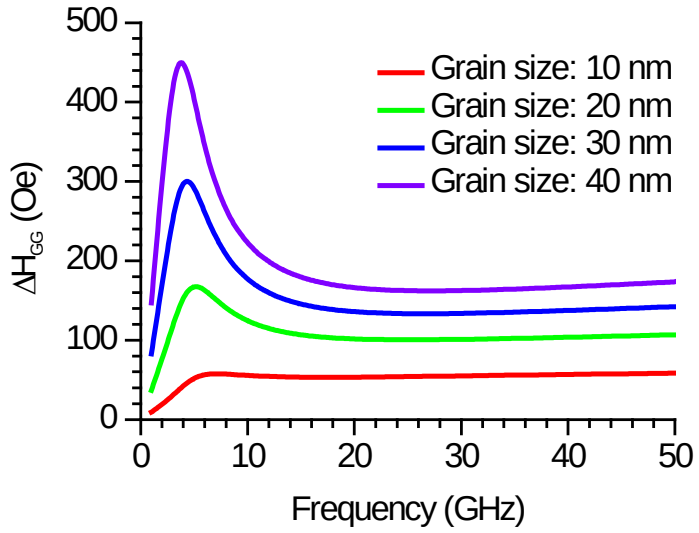

FIG. 3.2. Plot of grain-to-grain two-magnon scattering linewidth contribution vs. frequency. The curves are calculated for the in-plane external magnetic field configuration for films with different average grain sizes, as indicated. The level of the grain-to-grain two-magnon scattering linewidth contribution increases as the average grain size increases.

$$\Delta H_{\mathrm{GG}} = \frac{|\gamma|\xi^2 H_{\mathrm{A}}^2}{P_{\mathrm{A}}} \int_0^{k_{\max}} \Lambda_{\mathrm{GG}}\ C_{\mathrm{GG}}\ D\ dk \tag{3.23}$$

As shown in Fig. 3.2, the calculated grain-to-grain TMS linewidth contributions are not linearly dependent on the frequency. They show a peak response around 6 GHz and is almost constant beyond 20 GHz. The curves are calculated based on the parameters given in Chapter 2 ($4\pi M_s$ =10.5 kG and $|\gamma| = 2\pi \cdot 2.8$ MHz/Oe). The crystalline magnetic anisotropy is considered to be cubic, and the effective anisotropy field H_{A} is taken to be 1 kOe. The film thickness d is 50 nm, the exchange constant D is $2.394 \cdot 10^{-9}$ Oe×cm^2/rad^2, and the average grain size are given in Fig. 3.2.

3.3 Grain-boundary two-magnon scattering

Grain-boundary TMS has been reported in metallic alloy films by Nan Mo[13]. It is mainly caused by the presence of uniaxial anisotropy at grain boundaries. The theory is established based on three assumptions: (1) the grain boundaries are perpendicular to the film plane, (2) the grain size distribution in the plane is uniform and Gaussian-like, and (3) there exists an extra surface anisotropy (uniaxial) at the grain boundaries. The surface anisotropy at the grain boundaries has a non-uniform spatial distribution, which acts as a perturbation field and gives grain boundary scattering. The grain-boundary TMS relaxation rate is written as Eq. (3.24).

$$\eta_{\mathrm{GB}} = \frac{3|\gamma|^2 K_{\mathrm{s}}^2}{2M_{\mathrm{s}}^2} \int_0^{k_{\max}} \Lambda_{\mathrm{GB}}\ C_{\mathrm{GB}}\ D\ dk \tag{3.24}$$

where K_{s} is the grain boundary surface anisotropy constant in the unit of erg/cm^2. The elipticity function and the correlation function for the grain-boundary TMS can be written as follow.

$$\Lambda_{\mathrm{GB}} = \frac{a_k\left(3\omega_x \cos^2\theta_{\mathrm{M}} + \omega_y\right)\cos^2\theta_{\mathrm{M}} + b_k\left(\omega_x \cos^2\theta_{\mathrm{M}} + 3\omega_y\right)}{2\omega^2} \tag{3.25}$$

$$\begin{aligned} a_k &= \omega_{\mathrm{H}} + Dk^2 + (1-N_k)\cos^2\theta_{\mathrm{M}}\cos^2\theta_k + N_k \sin^2\theta_{\mathrm{M}} \\ b_k &= \omega_{\mathrm{H}} + Dk^2 + (1-N_k)\sin^2\theta_k \end{aligned} \tag{3.26}$$

$$C_{\mathrm{GB}} = \frac{k^2\xi^2 g\left(\frac{k\xi}{\pi}, 1, \frac{\sigma}{\xi}\right)}{\left[1+(k\xi)^2\right]^{\frac{3}{2}}} \tag{3.27}$$

g in Eq. (3.27) is the Gaussian distribution with σ as the standard deviation. The linewidth contribution of the grain-boundary TMS is expressed as Eq. (3.28).

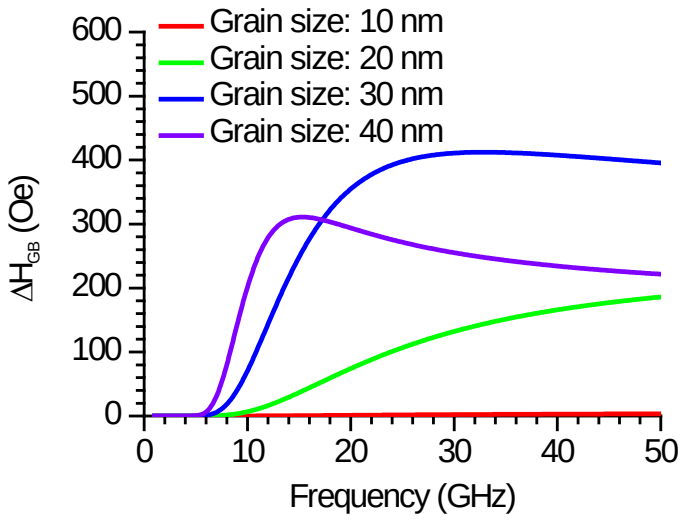

FIG. 3.3. Plot of grain-boundary two-magnon scattering linewidth contribution vs. frequency. The curves are calculated for the in-plane external magnetic field configuration, a fixed standard deviation of grain size distribution (15 nm), and different average grain sizes, as indicated.

$$\Delta H_{\mathrm{GB}} = \frac{3|\gamma|K_{\mathrm{s}}^{2}}{M_{\mathrm{s}}^{2}P_{\mathrm{A}}}\int_{0}^{k_{\max}} \Lambda_{\mathrm{GB}}\, C_{\mathrm{GB}}\, D\, dk \tag{3.28}$$

One can see from Eq. (3.28) that the grain-boundary TMS linewidth not only depends on the average grain size but also on the standard deviation of the grain size distribution. Figures 3.3 and 3.4 show the average grain size dependence and standard deviation of the grain size distribution dependence of grain-boundary TMS linewidth contribution, respectively. The calculations are done with the same parameters used for the calculations of the curves shown in Fig. 3.2, except for the average grain size and standard deviation of the grain size distribution. Similar to the results shown in Fig. 3.2, the grain-boundary TMS is significantly impacted by the average grain size and standard deviation of the grain size distribution. One can draw the conclusion that the TMS processes in magnetic thin films can be tuned by the grain size

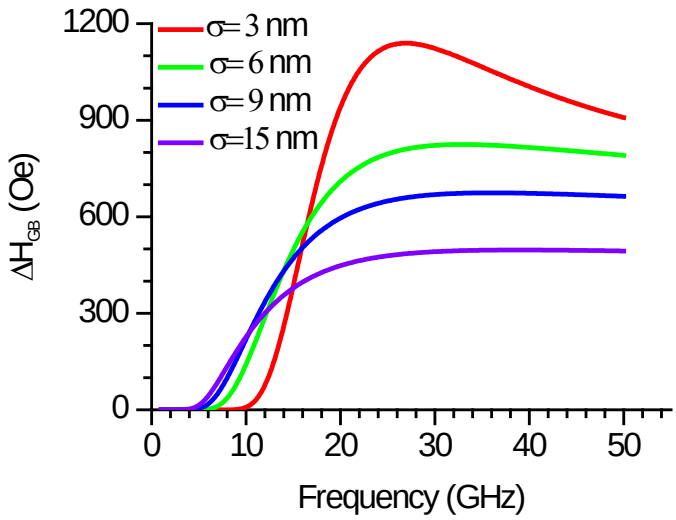

FIG. 3.4. Plot of grain-boundary two-magnon scattering linewidth contribution vs. frequency. The curves are calculated for the in-plane external magnetic field configuration, a fixed average grain size (30 nm), and different standard deviations of the grain size distribution, as indicated.

distribution, so does the TMS relaxation rate which is an important component of the net magnetization relaxation rate.

The magnetization relaxation rate can be specifically tailored by careful controlling the grain size distribution. The tuning of the magnetization relaxation rate in ferromagnetic thin films is of great fundamental and practical significance, and specific examples on tuning the magnetization relaxation rate through the grain size distribution are discussed in Chapter 6.

3.4 Inhomogeneity line broadening

FMR profiles could be broadened by a number of mechanisms, and the broadening featured itself as an increase in the FMR linewidth. TMS is one mechanism that leads to a Lorentzian shape line broadening, while inhomogeneity line-broadening is another mechanism which, in

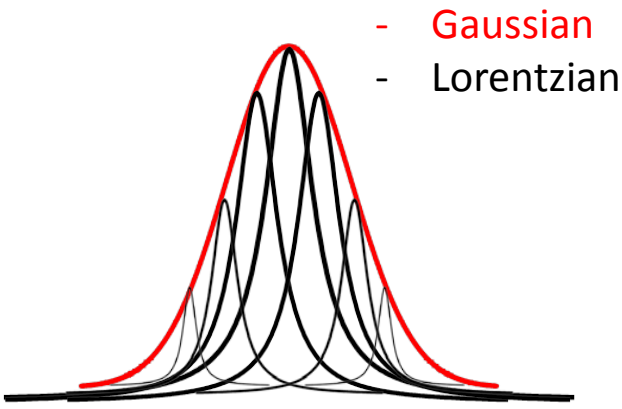

FIG. 3.5. Schematic plot of inhomogeneity line-broadening mechanism. The black lines are Lorentzian shape FMR profiles. The red line is the superposition of local FMR profiles, which has a Gaussian shape.

contrast, leads to a Gaussian shape line broadening. Inhomogeneity is an unavoidable factor that exists in all the samples. It could be spatial variations in the external magnetic field, the saturation magnetization, or the magnetic anisotropy strength or direction etc. Any spatial variations can cause the local FMR profiles to vary from region to region in the sample. As a result, the measured FMR profile is the superposition of local FMR profiles generated by different sample regions, as shown schematically in Fig. 3.5. Normally each local FMR profile has Lorentzian shape, which contains the Gilbert contribution and maybe also a TMS contribution. The inhomogeneity line broadening contribution, however, has Gaussian shape due to the fact that inhomogeneity usually follows a Gaussian distribution. The convolution is given as Eq. (3.29).

$$\Delta H_{\text{tot}} = \frac{\Delta H_{\text{Lorentzian}} + 1.97\Delta H_{\text{Lorentzian}}\Delta H_{\text{Gaussian}} + 2.16\Delta H_{\text{Gaussian}}}{\Delta H_{\text{Lorentzian}} + 2.16\Delta H_{\text{Gaussian}}} \tag{3.29}$$

3.5 Physical relaxation processes in magnetic materials

The damping mechanisms in the free layer of tunnel magneto-resistance reader, Fe-Co alloy films, and exchange-coupled composite media will be discussed later. Different physical relaxation processes including Gilbert damping, grain-to-grain two-magnon scattering, grain-boundary two-magnon scattering, and spin pumping have been introduced. This subsection provides an overview of damping processes in magnetic materials. It provides a summary on the damping mechanisms which have been introduced, and also extends the perspective to the damping mechanisms which haven't been touched. This overview will serve to simplify the discussions on damping in the following chapters.

The magnetization in a magnetic material can precess around the direction of a static magnetic field. One can excite a uniform magnetization precession by the use of an RF field. Once the microwave magnetic field is turned off, however, the magnetization will tend to relax

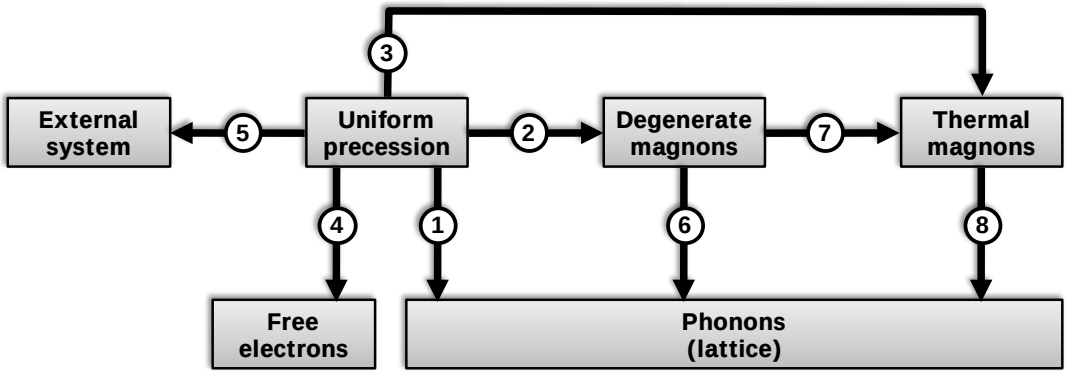

FIG. 3.6 A roadmap for the relaxation of uniform magnetization precession in magnetic materials.

back to the static field direction. Figure 3.6 gives a schematic roadmap for the relaxation or damping of uniform magnetization precession. The arrows and numbers indicate different relaxation routes. Generally speaking, there are three main pathways for magnetization relaxations in a magnetic material: (I) energy redistribution within the magnetic system through routes 2 and 3; (II) energy transfer out of the magnetic system to non-magnetic systems through routes 1 and 4; and (III) energy transfer out of the material to external systems through route 5.

Possible physical relaxation processes in routes 1-5 are summarized in Table 3.1. The relaxation processes in routes 6 and 8 are similar to those in route 1, and the processes in route 7 are similar to those in route 3.

Table 3.1. Physical Relaxation Processes in Magnetic Materials

Route	**Relaxation Process**	**Brief Description**
1	Magnon-phonon scattering	For this process, one views the uniform precession modes as magnons with zero wavenumbers. Those magnons scatter with phonons (lattice vibration modes) and pass their energy to the phonons.
	Charge transfer relaxation	This process is also called the valence-exchange or Fe^{2+}-Fe^{3+} relaxation and occurs in crystals with Fe^{2+} and Fe^{3+} ions on equivalent sites. When there is a net spin alignment, the site degeneracy is split slightly. Via spin-orbit coupling, the precession leads to the breathing of the energy level of each site, resulting in the hopping of a 3d electron from one iron ion to another.
	Slowly relaxing impurity	The impurities are usually rare-earth elements. The relaxation relies on the exchange coupling between the spins of magnetic elements and those of impurity and the coupling of the impurity spins to the lattice. The exchange coupling is anisotropic. As a result, the splitting of the two lowest energy levels depends on the instantaneous direction of the magnetization, leading to the transitions of the impurity between the two energy levels.
	Rapidly relaxing	This is similar to the slowly relaxing impurity mechanism. The

	impurity	difference is that the exchange coupling is isotropic and the energy levels do not breathe. The impurities absorb energy from the magnetization precession and changes from the ground state to the excited state.
	Eddy current	This involves a loss of energy of the uniform precession to the lattice through the conduction electrons. The eddy-current damping increases with the square of the linear sample dimension, such as the film thickness.
2	Two-magnon scattering	This process involves the scatting of zero-wavenumber magnons with inhomogeneities, such as grain-to-grain fluctuations, grain boundaries, small pores, and surface defects. After each scattering, the initial magnon is annihilated and a new magnon is created. The new magnon has a frequency which is the same as the initial magnon and a wavenumber which correlates with the spatial variation of the inhomogeneities.
3	Three-magnon scattering	This process includes three-magnon confluence and three-magnon splitting. In a confluence process, two magnons scatter with each other and are annihilated, and one new magnon is created. In a splitting process, one magnon is annihilated and two new magnons are created.
	Four-magnon scattering	In each scattering process, two magnons scatter with each other and are destroyed, and two new magnons are created.
4	Spin-flip magnon-electron scattering	When a “spin-up” free electron scatters with a magnon, it absorbs the energy of the magnon, destroys it, and changes into a “spin-down” electron. With an increase in temperature, the electron lifetime decreases and the electron Fermi level broadens. As a result, the magnon-electron scattering probability increases and the damping increases.
	Breathing Fermi surface	This process is also called intraband magnon-electron scattering. Via spin-orbit coupling, the magnetization precession changes the energy of the free electron states, pushing some occupied states above the Fermi level and some unoccupied states below the Fermi level. As a result, the electron-hole pairs are produced near the Fermi level. These pairs exist for some lifetime before relaxation through scattering with the lattice. The energy dissipated to the lattice depends on how far the system gets from equilibrium, and the latter increases with the electron lifetime.
5	Spin pumping	At a ferromagnet/normal metal interface, the magnetization precession in the ferromagnet produces a spin current that flows into the normal metal. This spin current carries spin angular momentum

		out of the ferromagnet.

Several phenomenological models have been proposed to describe the relaxation of the uniform magnetization. These models include the Gilbert model, the Landau-Lifshitz model, and the Bloch-Bloembergen model. Each model can take into account one or more of the relaxation processes listed in Table 3.1. None of the existing models, however, can take into account all of the processes. For example, the Gilbert model can describe rigorously the magnon-phonon and magnon-electron scattering processes but fails to describe the two-magnon scattering. In a two-magnon scattering process, the longitudinal component of the magnetization is unchanged and the length of the magnetization vector decreases. As a result, this process can only be described by the T_2 term in the Bloch-Bloembergen equation. In this sense, it is incorrect if one attempts to describe all the relaxation processes in a material with a single damping parameter, such as the Gilbert constant *a*.

Ferromagnetic resonance (FMR) is probably the most widely used technique for the study of the damping of uniform precession. Different FMR techniques have been developed for magnetic material damping studies. Conventional FMR techniques and VNA-FMR techniques will be introduced and applied in various magnetic materials' damping studies later. FMR linewidth is the key parameter to characterize the damping. The origin of the FMR linewidth differs significantly for different materials. In general, one can express the linewidth as Eq. (3.30).

$$\Delta H = \sum_i \Delta H_i + \Delta H_{\mathrm{ILB}} \tag{3.30}$$

where ΔH_i denotes the contribution from a certain relaxation process i and ΔH_{ILB} takes into account the inhomogeneity-caused line broadening. It is important to emphasize that the inhomogeneity line broadening is not a loss, as described in the last section.

At the first glance, it seems really hard to obtain useful information on damping from FMR linewidth measurements. In practice, however, FMR techniques have proved to be an extremely useful tool for the identification and even quantization of different physical damping processes in a great variety of materials. This is possible for three facts as follows. (1) For a specific material, not all the processes listed in Table 3.1 are involved in the relaxation. Rather, only a few of processes take place or play important roles. In a high-resistivity ferrite, for example, the relaxation via the magnon-phonon scattering and charge transfer processes are possible, but the eddy current and magnon-electron scattering effects are negligible. (2) Many of the relaxation processes show unique temperature or frequency dependences. In some cases, this makes it fairly easy to distinguish one process from another. (3) Some of the processes can be easily turned on or off through a change in FMR configurations, such as the direction and magnitude of the static magnetic field. For magnetic thin films, for example, one can suppress the two-magnon scattering simply by applying the static field normal to the film plane, as discussed in chapter 5 and 7.

CHAPTER 4. VECTOR NETWORK ANALYZER FERROMAGNETIC RESONANCE TECHNIQUES

4.1. Vector network analyzer FMR spectrometer system

Besides conventional FMR technique, Stripline, vector network analyzer, and pulsed inductive microwave magnetometer techniques are used to measure FMR responses (Kalarickal 2006). In this chapter, the development of an ultra-sensitive broadband FMR spectrometer based on the vector network analyzer (VNA) FMR technique is described, and the comparison between the VNA-FMR technique and conventional FMR techniques is presented. The objective for developing the VNA-FMR technique is to resolve long-standing problems in damping characterization of ultra-thin magnetic films and perpendicular magnetic recording media. The VNA-FMR spectrometer is designed to measure the FMR responses at different microwave frequencies in a magnetic ultra-thin film with an external magnetic field applied along the normal direction of the film plane (Nembach and Silva 2011).

Figure 4.1 shows a schematic diagram of the VNA-FMR spectrometer. A vector network analyzer with operating frequency range from 10 MHz to 50 GHz is used to measure the scattering parameters of a coplanar waveguide (CPW) on which a magnetic thin film magnetic is placed. In the measurements, both the real and imaginary parts of the transmission (S_{21}) coefficients are collected by the VNA. Ground-signal-ground probes (not shown in Fig. 4.1) and low noise cables are used to build the connection between the VNA and the CPW/sample structure. The probes can be attached and detached from the CPW through a probe station with

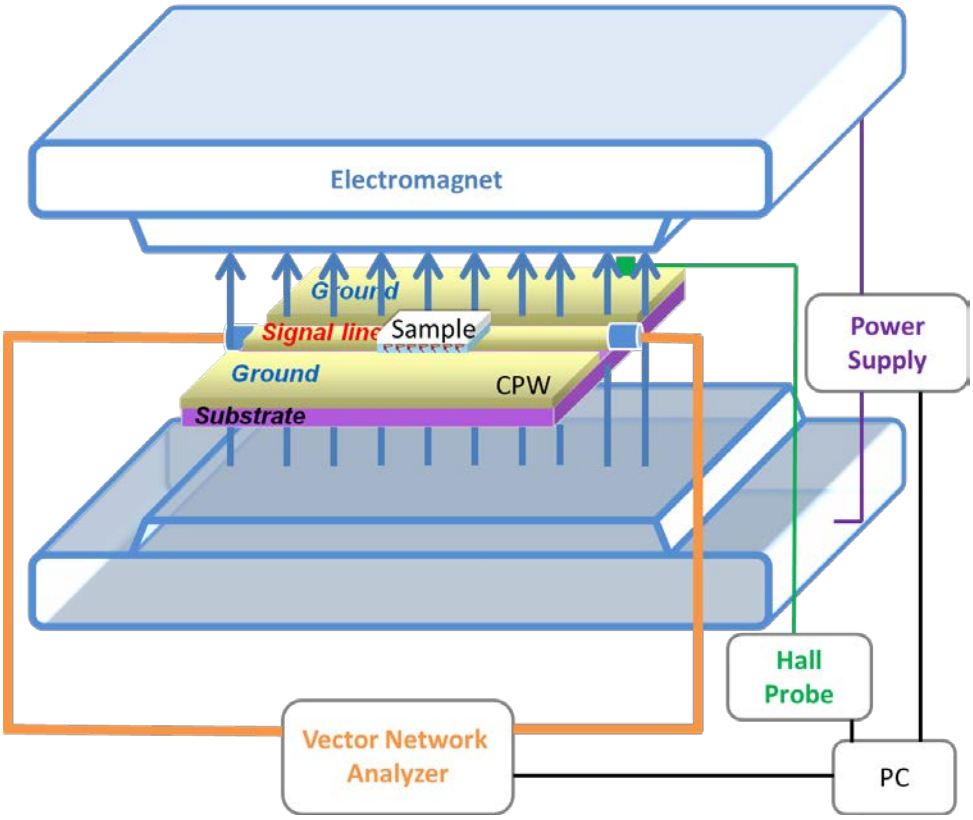

FIG. 4.1. Schematic diagram of a vector network analyzer ferromagnetic resonance spectrometer. The blue layer of the sample is the magnetic film, and the white layer is the substrate. The green square between the two electromagnet poles is the Hall probe. The blue cylinders stand for the ground-signal-ground probes.

xyz fine control translation stages.

The CPW has a 100-μm-wide signal line and 50-μm-gaps between the signal line and the grounds. The CPW is designed to have a 50 Ω impedance in order to keep the impedance matching with the probes and the cables and minimize microwave power loss caused by reflections at the interfaces. The external magnetic field is provided by a GMW dipole

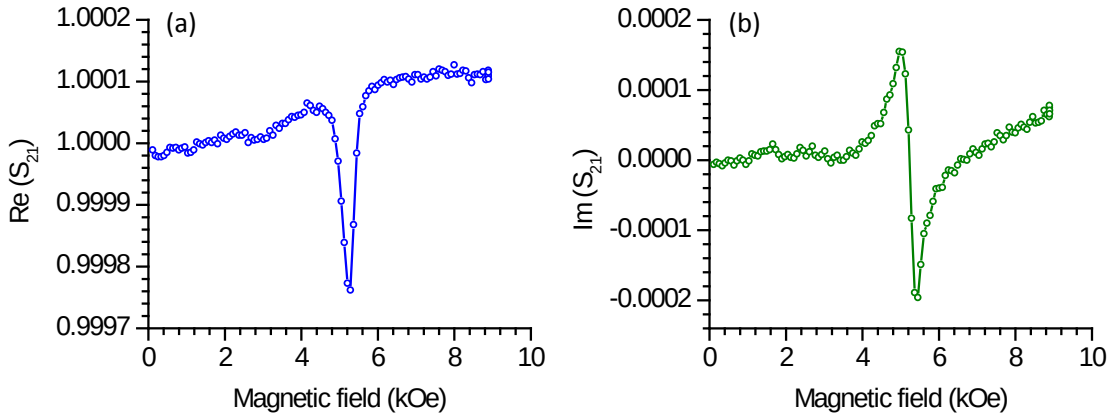

FIG. 4.2. Example of measured complex transmission coefficient data. Graph (a) shows the real part of S_{21}, while graph (b) shows the imaginary part of S_{21}.

electromagnet, and the highest field is 10 kOe.

The sample is placed on the top of the CPW structure, with the film side facing the CPW and the substrate side facing up. Samples of insulating magnetic films can be directly placed on the CPW. Samples of metallic thin films, however, are spin-coated with an about-1-μm-thick non-conducting polymer layer in order to avoid any shorting of the CPW structure.

During the FMR measurements, the electromagnet operates under a fast sweeping mode, so that the magnetic field can be swept from 0 to 10 kOe within a period of 1 minute. The field amplitude is measured by the Hall probe in a real time manner. While the magnetic field is sweeping, the vector network analyzer operates at a fixed microwave frequency and collects the complex transmission coefficient (S_{21}) data. A Labview program is written to operate and control the electromagnet, the vector network analyzer, and the Hall probe and collect the field, frequency, and transmission coefficient data. The data are sent to a PC where the plots of the

complex transmission coefficient vs. the magnetic field are generated. To reduce the random background noise, the signal averaging method is applied. By averaging a set of replicate measurements, the random background noise can be significantly suppressed. The signal-to-noise ratio is generally proportion to the square root of the number of measurements. Usually, 20 to 40 measurements are taken for averaging.

Figure 4.2 presents an example of the experimental data which were obtained after 20 times of averaging. Figure 4.2 (a) gives the real part of S_{21} as a function of the external magnetic field which shows a single dip response. Figure 4.2 (b) gives the imaginary part of S_{21} as a function of the external magnetic field which shows a double peak response. Those dip and peak responses result from the FMR effect in the magnetic film.

4.2. FMR responses expressed in terms of transmission coefficients

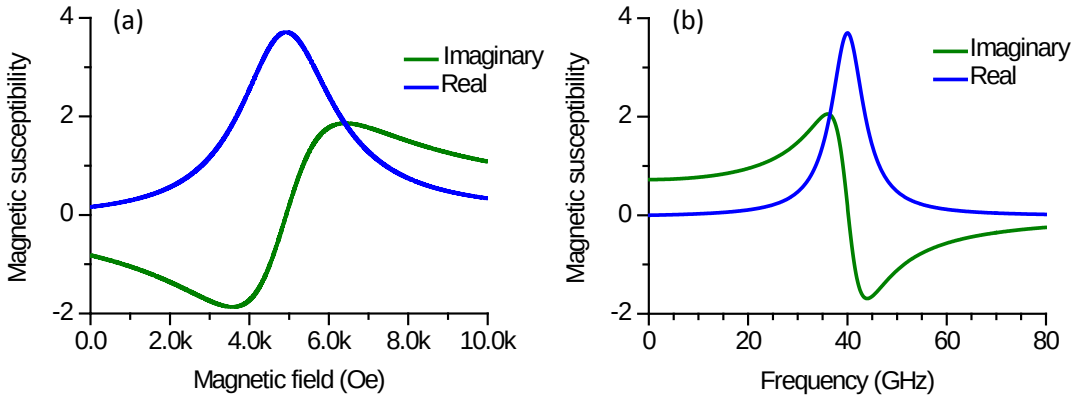

FIG. 4.3. Plots of magnetic susceptibility. Graph (a) shows the magnetic field dependence of the magnetic susceptibility for a given microwave frequency. Graph (b) shows the microwave frequency dependence of the magnetic susceptibility for a given magnetic field.

To extract the FMR field and linewidth from the S_{21} data, the correlation between the complex transmission coefficient and the magnetic susceptibility should be developed. Based on the discussions in Chapter 1, one can write the general expressions for the magnetic susceptibility as the following.

$$4\pi\chi_{xx} = \frac{\omega_M\left(\omega_y + i\alpha\omega\right)}{\omega_x\omega_y - \omega^2 + i\alpha\omega(\omega_x + \omega_y)} \tag{4.1}$$

$$4\pi\chi_{yy} = \frac{\omega_M\left(\omega_x + i\alpha\omega\right)}{\omega_x\omega_y - \omega^2 + i\alpha\omega(\omega_x + \omega_y)} \tag{4.2}$$

When an out-of-plane magnetic field is applied to a thin film with a perpendicular anisotropy, the stiffness frequencies have a relatively simple form as Eq. (4.3).

$$\omega_x = \omega_y = |\gamma|\left(H_{\text{ext}} + H_{\text{k}} - 4\pi M_{\text{s}}\right) \tag{4.3}$$

Thus one has $4\pi\chi_{xx} = 4\pi\chi_{yy}$ and can write the full expression of the magnetic susceptibility (χ) as Eq. (4.4).

$$\chi = \frac{|\gamma|4\pi M_{\text{s}}\left[|\gamma|\left(H_{\text{ext}} + H_{\text{k}} - 4\pi M_{\text{s}}\right) + i\alpha\omega\right]}{|\gamma|^2\left(H_{\text{ext}} + H_{\text{k}} - 4\pi M_{\text{s}}\right)^2 - \omega^2 + 2i\alpha\omega|\gamma|\left(H_{\text{ext}} + H_{\text{k}} - 4\pi M_{\text{s}}\right)} \tag{4.4}$$

Usually, the FMR responses are characterized by measuring the complex magnetic susceptibility as a function of the external magnetic field, $\chi(H_{ext})$, at a fixed microwave frequency, or measuring the susceptibility as a function of the microwave frequency, $\chi(f)$, at a fixed magnetic field. Figures 4.3 (a) and (b) present the numerical calculations of the complex magnetic susceptibility with varying the external fields and the microwave frequencies, respectively. In the following analysis, only the magnetic field-dependent susceptibility is considered since the VNA-FMR technique measures the FMR response by sweeping the external

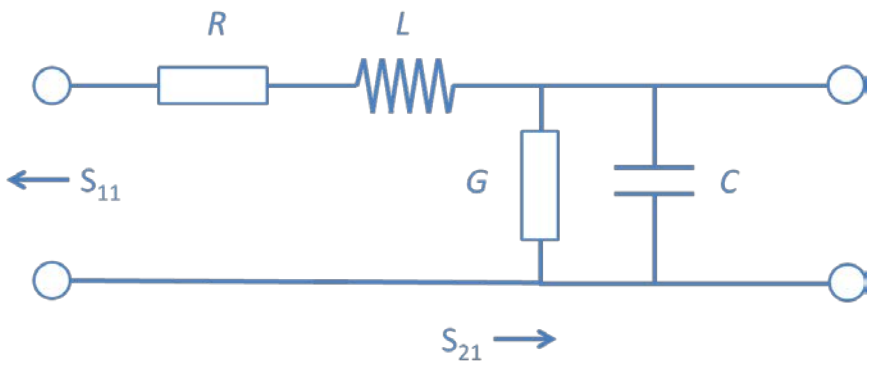

FIG. 4.4. Schematic diagram of effective circuit of the CPW/sample structure. R is the series resistance, L is the effective inductance, G is the shunt conductance, and C is the capacitance. S_{11} is the reflection coefficient, and S_{21} is the transmission coefficient.

magnetic field at a fixed frequency.

The magnetic responses in the films critically affect the effective impedance of the CPW/sample structure. To characterize this correlation, one needs to determine the scattering matrix of the CPW/sample structure. The CPW with a thin film placed on top can be approximately treated as a lumped element with an effective series resistance R, an effective inductance L, an effect shunt conductance G, and an effective capacitance C. The effective microwave circuit is shown in Fig. 4.4. The refection and transmission coefficients can be written as Eq. (4.5) and (4.6) (Ding 2004).

$$S_{11} = \frac{i\omega L + R + \dfrac{Z_0}{1 + Z_0(G + i\omega C)} - Z_0}{i\omega L + R + \dfrac{Z_0}{1 + Z_0(G + i\omega C)} + Z_0} \tag{4.5}$$

$$S_{21} = \frac{\dfrac{2Z_0}{1+Z_0(G+i\omega C)}}{i\omega L + R + \dfrac{Z_0}{1+Z_0(G+i\omega C)} + Z_0} \tag{4.6}$$

where Z_0 is the characteristic impedance (50 Ω) of the CPW and ω is the microwave angular frequency. Solving Eq. (4.5) and Eq. (4.6) one obtains Eq. (4.7).

$$i\omega L = \frac{1+S_{11}-S_{21}}{1-S_{11}} Z_0 - R \tag{4.7}$$

The effective inductance can be expressed in terms of Eq. (4.8) (Ding 2004).

$$L \approx L_0 + clt\mu\mu_0 \tag{4.8}$$

where L_0 is the self-inductance of the CPW, c is a geometry factor with a unit of m^{-1}, l is the length of the film sample, t is the thickness of the magnetic film, and μ_0 is the permeability of vacuum. Taking the approximation that $\chi \approx \mu$, the magnetic susceptibility can be written as Eq. (4.9).

$$\chi = \mu = \frac{Z_0\left(\dfrac{1+S_{11}^1-S_{21}^1}{1-S_{11}^1} - \dfrac{1+S_{11}^0-S_{21}^0}{1-S_{11}^0}\right)}{iclt\mu_0\omega} \tag{4.9}$$

where S_{11}^1 and S_{21}^1 denote the measured reflection and transmission coefficients, respectively, and S_{11}^0 and S_{21}^0 denote the nonmagnetic contributions. Equation (4.9) is obtained under the assumption that the complex reflection and transmission coefficients consist of magnetic and nonmagnetic contributions and can be written as

$$S_{11}^1 = S_{11}^0 + \Delta S_{11} \tag{4.10}$$

$$S_{21}^1 = S_{21}^0 + \Delta S_{21} \tag{4.11}$$

where ΔS_{11} and ΔS_{21} denote the magnetic contribution. With the limit of weak reflected microwave power ($|S_{11}| \ll 1$) from the magnetic thin film sample, Eq. (4.9) can be reduced to Eq. (4.12).

$$\chi \cong \chi_0 \left[\left(2 + 2S_{11}^0 - S_{21}^0 \right) \Delta S_{11} - \left(1 + S_{11}^0 \right) \Delta S_{21} \right] \tag{4.12}$$

where χ_0 is a complex function which contains experimental parameters like *c*, *l*, *t*, μ_0, and ω. The relation $\Delta S_{11} = -\Delta S_{21}$ is considered under the quasi-static limit. Thus Eq. (4.12) can be further reduced to the form of Eq. (4.13).

$$\chi \cong -\chi_0 \left[3\left(1 + S_{11}^0 \right) - S_{21}^0 \right] \Delta S_{21} \tag{4.13}$$

Perfect impedance matching between the waveguide and measurement system is assumed when the magnetic contribution is zero. In the limit of the 100% transmission of the microwave excitations, the expression of the magnetic susceptibility can be simplified as Eq. (4.14).

$$\chi \cong -2\chi_0 \Delta S_{21} \tag{4.14}$$

Equation (4.14) correlates the transmission coefficient of the CPW/sample structure to the magnetic susceptibility in the magnetic film. For the determination of the FMR results from the transmission coefficients, however, one uses a modified equation as follows

$$S_{21}(H,t) = S_{21}^0 - \frac{\chi(H)}{\chi_0} + Dt \tag{4.15}$$

where *t* is time and *D* is a purely phenomenological complex constant. The term Dt stands for the first-order correction to time-dependent signal drifts. This term is included because the magnetic contribution ΔS_{21} is ultra-small and the signal drift is a non-negligible quantity. Note that the term Dt is a simple linear correction, and a rapid external magnetic field sweep is

required to minimize the time-dependent drift. χ_0 in Eq. (4.15) is taken as a complex fitting parameter that compensates for the amplitude and phase differences between the measured complex transmission coefficient of the CPW/sample structure and the complex magnetic susceptibility of the magnetic thin film.

As described in Chapter 2, the magnetic susceptibility for out-of-plane field geometry can be written as Eq. (4.16).

$$\chi\left(H_{\text{ext}}\right)=\frac{|\gamma|4\pi M_{\text{s}}\left[|\gamma|\left(H_{\text{ext}}+H_{\text{k}}-4\pi M_{\text{s}}\right)+\frac{1}{2}|\gamma|\Delta H\right]}{|\gamma|^{2}\left(H_{\text{ext}}+H_{\text{k}}-4\pi M_{\text{s}}\right)^{2}-\omega^{2}+i\omega|\gamma|\Delta H} \tag{4.16}$$

On the other hand, the complex transmission coefficient S_{21} can be written as

$$S_{21}(H_{ext},t)=S_{21,R}(H_{ext},t)+iS_{21,I}(H_{ext},t) \tag{4.17}$$

With Eq. (4.15) and Eq. (4.16), one can write the full expressions for the real and imaginary parts of S_{21} as

$$\begin{aligned}S_{21,\text{R}}(H_{\text{ext}},t)=S_{21,\text{R}}^{0}+D_{\text{R}}t+&\frac{\left[4\pi M_{\text{s}}\chi_{0,\text{I}}\frac{\Delta H}{2}+4\pi M_{\text{s}}\chi_{0,\text{R}}\left(H_{\text{ext}}+H_{\text{k}}-4\pi M_{\text{s}}\right)\right]}{\left\{\left[\left(H_{\text{ext}}+H_{\text{k}}-4\pi M_{\text{s}}\right)^{2}-\left(\frac{\omega}{|\gamma|}\right)^{2}\right]^{2}+\left(\Delta H\frac{\omega}{|\gamma|}\right)^{2}\right\}\left(\chi_{0,\text{R}}^{2}+\chi_{0,\text{I}}^{2}\right)}\\&\times\left[H_{\text{ext}}^{2}+2H_{\text{ext}}H_{\text{k}}-2H_{\text{ext}}4\pi M_{\text{s}}+H_{\text{k}}^{2}-2H_{\text{k}}4\pi M_{\text{s}}+\left(4\pi M_{\text{s}}\right)^{2}-\left(\frac{\omega}{|\gamma|}\right)^{2}\right]\\&-\frac{\left[4\pi M_{\text{s}}\chi_{0,\text{R}}\frac{\Delta H}{2}-4\pi M_{\text{s}}\chi_{0,\text{I}}\left(H_{\text{ext}}+H_{\text{k}}-4\pi M_{\text{s}}\right)\right]\Delta H\frac{\omega}{|\gamma|}}{\left\{\left[\left(H_{\text{ext}}+H_{\text{k}}-4\pi M_{\text{s}}\right)^{2}-\left(\frac{\omega}{|\gamma|}\right)^{2}\right]^{2}+\left(\Delta H\frac{\omega}{|\gamma|}\right)^{2}\right\}\left(\chi_{0,\text{R}}^{2}+\chi_{0,\text{I}}^{2}\right)}\end{aligned} \tag{4.18}$$

and,

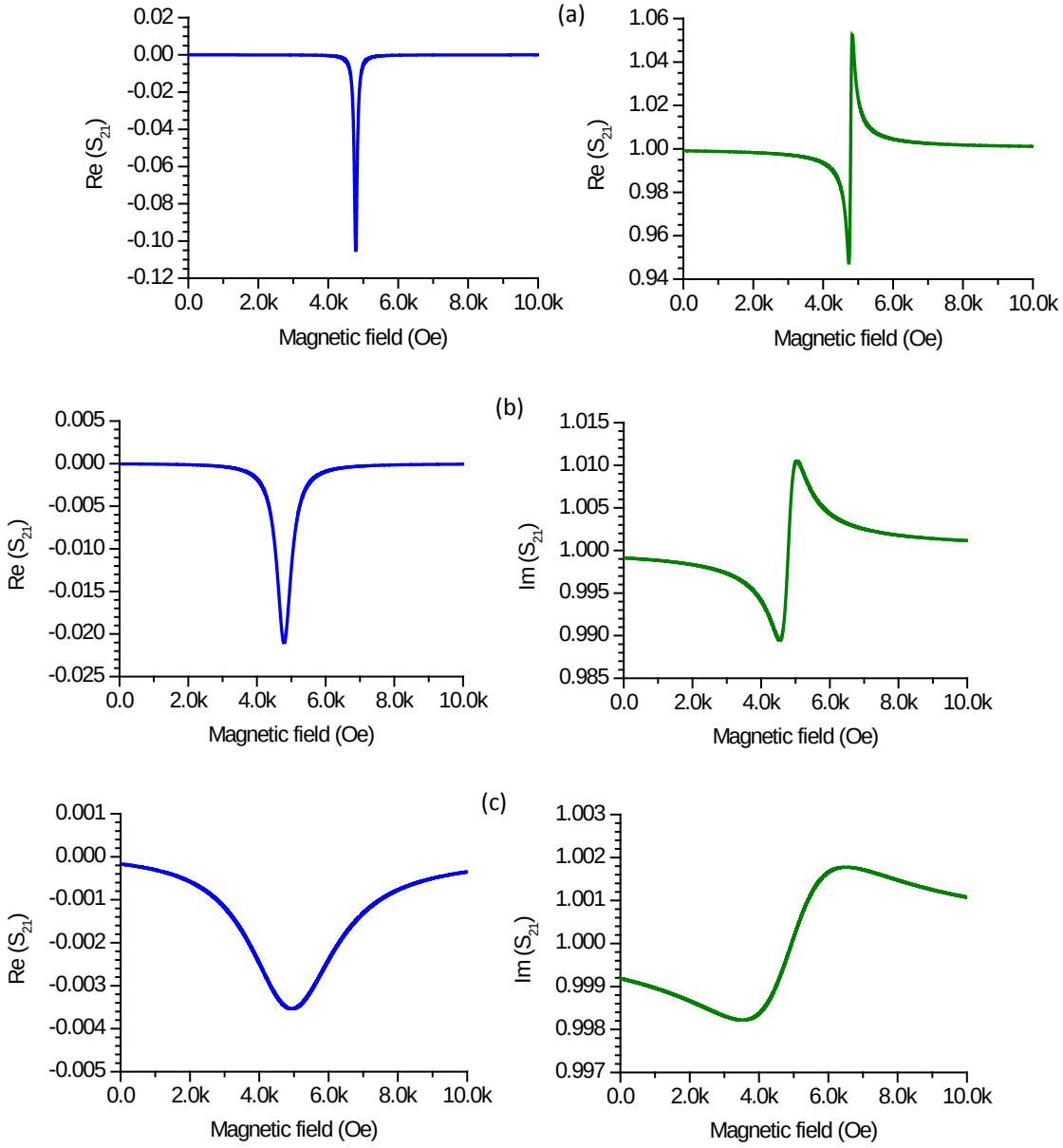

FIG. 4.4. Plots of complex transmission coefficient ΔS_{21} calculated with different values of FMR linewidth, as indicated.

$$S_{21,\mathrm{I}}(H_{\mathrm{ext}},t)=S_{21,\mathrm{I}}^{0}+D_{\mathrm{I}}t+\frac{\left[4\pi M_{\mathrm{s}}\chi_{0,\mathrm{R}}\dfrac{\Delta H}{2}-4\pi M_{\mathrm{s}}\chi_{0,i}\left(H_{\mathrm{ext}}+H_{\mathrm{k}}-4\pi M_{\mathrm{s}}\right)\right]}{\left\{\left[\left(H_{\mathrm{ext}}+H_{\mathrm{k}}-4\pi M_{\mathrm{s}}\right)^{2}-\left(\dfrac{\omega}{|\gamma|}\right)^{2}\right]^{2}+\left(\Delta H\dfrac{\omega}{|\gamma|}\right)^{2}\right\}\left(\chi_{0,\mathrm{R}}^{2}+\chi_{0,\mathrm{I}}^{2}\right)}$$

$$\times\left[H_{\text{ext}}^2+2H_{\text{ext}}H_{\text{k}}-2H_{\text{ext}}4\pi M_{\text{s}}+H_{\text{k}}^2-2H_{\text{k}}4\pi M_{\text{s}}+\left(4\pi M_{\text{s}}\right)^2-\left(\frac{\omega}{|\gamma|}\right)^2\right]$$

$$+\frac{\left[4\pi M_{\text{s}}\chi_{0,\text{I}}\frac{\Delta H}{2}+4\pi M_{\text{s}}\chi_{0,\text{R}}\left(H_{\text{ext}}+H_{\text{k}}-4\pi M_{\text{s}}\right)\right]\Delta H\frac{\omega}{|\gamma|}}{\left\{\left[\left(H_{\text{ext}}+H_{\text{k}}-4\pi M_{\text{s}}\right)^2-\left(\frac{\omega}{|\gamma|}\right)^2\right]^2+\left(\Delta H\frac{\omega}{|\gamma|}\right)^2\right\}\left(\chi_{0,\text{R}}^2+\chi_{0,\text{I}}^2\right)} \tag{4.19}$$

To solve practical issues, $S_{21,\text{R}}$, $S_{21,\text{I}}$, t, $4\pi M_{\text{s}}$, H_{ext}, H_{k}, ω, and $|\gamma|$ are usually considered as parameters to be measured, and $S_{21,\text{R}}^0$, $S_{21,\text{I}}^0$, D_{R}, $\chi_{0,\text{R}}$, $\chi_{0,\text{I}}$, and ΔH are the fitting parameters.

In Fig. 4.4, examples of both the real and imaginary parts of the transmission coefficient ΔS_{21} vs. the external magnetic field H_{ext} plots are presented. These plots were calculated with different FMR linewidths, as indicated. All other parameters are the same for each calculation and are provided in the figure caption. One can see in Fig. 4.4 that the dip and peak responses in both the real and imaginary transmission profiles become broader as the FMR linewidth increases.

The development of the VNA-FMR technique allows for the measurements of the damping constants in ultra-thin ferromagnetic films or thin films with extreme large FMR linewidths (such as perpendicular recording media). The damping study on ultra-thin ferromagnetic films is presented in Section 4.4 in this chapter, while the damping study on perpendicular recording media is presented in Chapter 7.

4.3. Comparison between conventional FMR and VNA-FMR techniques

The ferromagnetic resonance phenomenon has been studied for decades, and several techniques have been developed to measure the ferromagnetic resonance. Conventional FMR techniques use either a standard shorted rectangular waveguide or a microwave cavity, and one usually measures the FMR linewidth by sweeping the magnetic field at a fixed microwave frequency. In general, FMR measurements with microwave cavities yield much higher signal-to-noise ratios than those using shorted waveguides. For this reason, microwave cavities are widely used in studying materials with relatively low FMR signals, such as ultra-thin films and materials with extraordinarily large damping. However, the microwave cavity-based technique has its own drawbacks. In particular, the operation frequency is fixed at a single

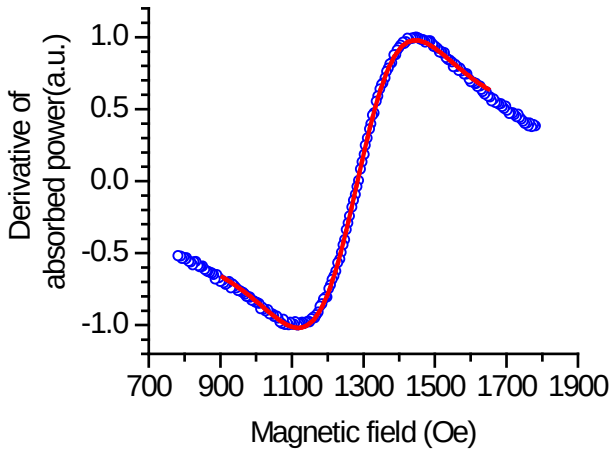

FIG. 4.5. Example of an FMR power absorption derivative profile measured by a conventional FMR technique. The blue circles show the data measured by a shorted waveguide, and the red curve is a fit to a Lorentzian derivative trial function. The sample is BaM ferrite.

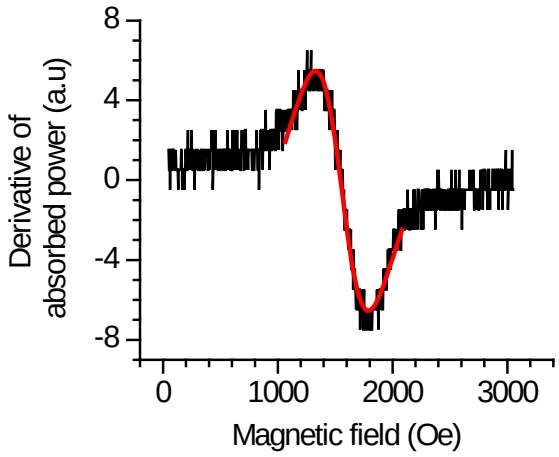

FIG. 4.6. FMR profile for a 2-nm-thick CoFeB film. The black curve shows the FMR data measured by a 9.7 GHz cavity. The red curve shows a fit to a Lorentzian derivative trial function.

value once the cavity is built. In order to perform frequency-dependent FMR studies, cavities with different operation frequencies need to be used. In contrast, shorted waveguides can provide a relatively broad operation frequency range. The signal-to-noise ratios for the shorted waveguide-based measurements, however, are usually very low for ultra-thin films and large-damping samples. The VNA-FMR technique can provide both high signal-to-noise ratios and extremely broad operation frequency ranges.

In conventional FMR techniques, field modulation and lock-in detection are usually used to increase signal-to-noise ratios. As a result, the measured signal is a derivative of the microwave power absorption. Figure 4.5 shows an example of a standard FMR profile for a BaM ferrite sample. The blue circles show the data measured by a shorted waveguid, while the red curve shows the fit to a Lorentzian derivative trial function. The fit yields an FMR field of about 1.28 kOe and an FMR linewidth of about 532 Oe.

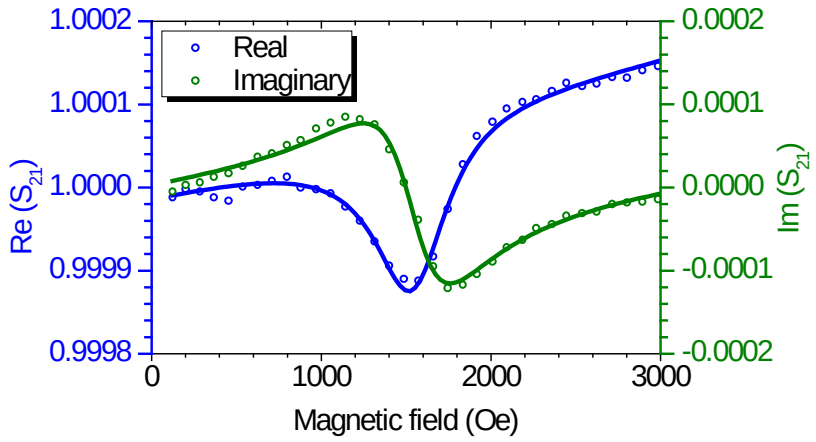

FIG. 4.7. FMR profiles for a 2-nm-thick CoFeB film measure by the VNA-FMR technique at 9.7 GHz. The circles show data, and the curves show numerical fits.

The comparison between conventional FMR and VNA-FMR techniques presented below made use of a sample which consists of a 2-nm-thick perpendicular anisotropy CoFeB film grown on a MgO substrate and capped by a Pd layer. Figure 4.6 shows the FMR results obtained with the conventional FMR technique. The black curve shows the experimental data measured by a 9.7 GHz rectangular cavity with an out-of-plane magnetic field applied. The red curve shows a fit to a Lorentzian derivative trial function. The fitting yields an FMR field of 1555 Oe and an FMR linewidth of 511 Oe.

The same sample was measured by the VNA-FMR technique. Figure 4.7 shows the experimental results measured by the VNA-FMR technique at 9.7 GHz. The blue and green circles show the measured real and imaginary parts of the transmission coefficients, respectively. The blue and green curves show the numerical fits to Eq. (4.18) and Eq. (4.19), respectively. The fitting yields an FMR fit of 1540 Oe and an FMR linewidth of 529 Oe. One can see that

the results measured by the conventional FMR technique and the VNA-FMR technique are comparable. One also can see that the data measured by the VNA-FMR technique have larger signal-to-noise ratios than the conventional FMR technique and can be well fitted by the S_{21} equations developed in the last section. In addition, the VNA-FMR technique provides a much broader frequency range (10 MHz to 50 GHz). No additional modifications on the experimental setup are required for measurements at different microwave frequencies. This makes frequency-dependent measurements extremely convenient.

4.4 Damping study on ultra-thin CoFeB films

Damping in ultra-thin ferromagnetic films is usually difficult to characterize since the FMR signals are very weak due to the extremely small volume of the films. The damping constants of 2-nm-thick CoFeB films are studied by the VNA-FMR technique. Two CoFeB films

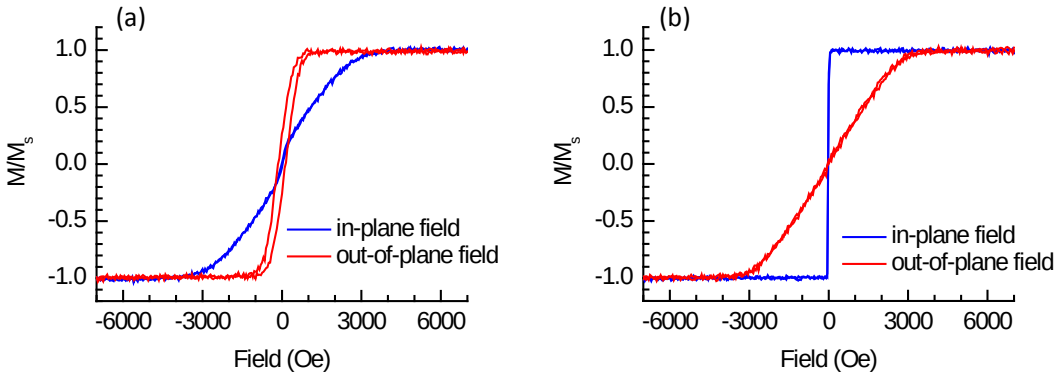

FIG. 4.8. Graphs (a) and (b) show the hysteresis loops of two CoFeB film samples: sample I and sample II. The blue curves were measured with in-plane magnetic fields, while the red curves were measured with out-of-plane magnetic fields.

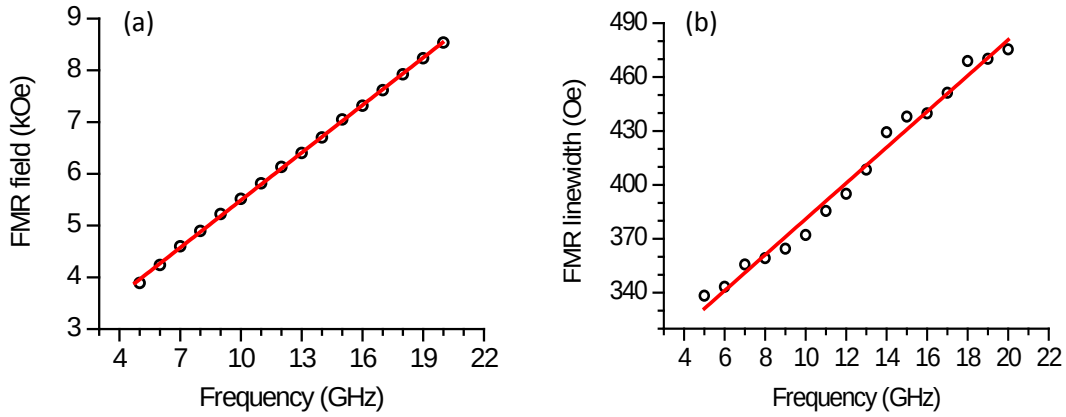

FIG. 4.9. Plots of (a) FMR field and (b) FMR linewidth as a function of frequency for sample I. The black circles show the data, and the red lines show numerical fits.

(sample I and sample II) with different out-of-plane anisotropies prepared by magnetron sputtering are used in this study. Both the in-plane and out-of-plane hysteresis loops were measured by a vibrating sample magnetometer (VSM). The loops are shown in Fig. 4.8, with the blue curves measured with in-plane magnetic fields and the red curves measured with out-of-plane fields. The saturation inductions ($4\pi M_s$) for sample I and sample II are 18.77 kG, and 19.45 kG, respectively.

For sample I, the FMR measurements were performed over a frequency range of 5-20 GHz. The frequency-dependent FMR field and linewidth data of sample I are shown in Fig. 4.9. The black circles show the data. The red line in graph (a) shows a fit to Eq. (4.20), while that in graph (b) shows a fit to Eq. (4.21).

$$\omega(H_{\text{ext}}) = |\gamma|(H_{\text{ext}} + H_{\text{k}} - 4\pi M_{\text{s}}) \tag{4.20}$$

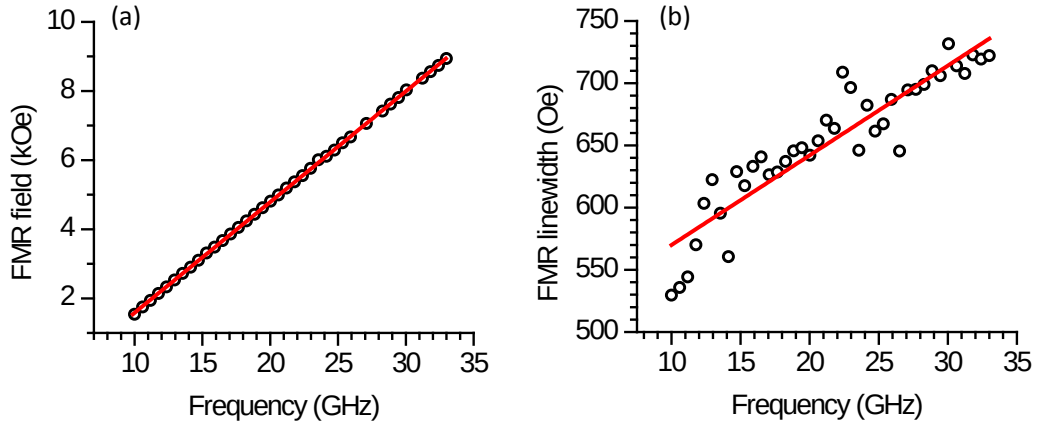

FIG. 4.10. Plots of (a) FMR field and (b) FMR linewidth as a function of frequency for sample II. The black circles show the data, and the red lines show numerical fits.

$$\Delta H(\omega_0) = \frac{2\alpha\omega_0}{|\gamma|} + \Delta H_{\mathrm{ILB}} \tag{4.21}$$

The fitting of the FMR field vs. frequency data yielded a gyromagnetic ratio of 3.26 GHz/kOe and an out-of-plane uniaxial anisotropy filed of 16.34 kOe. The fitting of the FMR lineiwidth vs. frequency data yielded a Gilbert damping constant of 0.016 and a contribution from inhomogeneity line broadening of 281 Oe.

For sample II, the FMR responses were measured over a frequency range of 10-35 GHz. Figure 4.10 shows the plots of the FMR field and FMR linewidth as a function of frequency of sample II. The black circles show the data, while the red lines show the fits to Eq. (4.10) and Eq. (4.11). The fitting yielded a gyromagnetic ratio of 3.12 GHz/kOe, an out-of-plane anisotropy field of 21.11 kOe, a Gilbert damping constant of 0.011, and a contribution from inhomogeneity line broadening of 497 Oe.

One can see that the two samples show similar gyromagnetic ratios and saturation inductions but different anisotropy fields and damping constants; and the sample with a higher anisotropy field shows a lower damping constant. In addition, one can also see that the VNA-FMR technique allows for study of damping in ultra-thin magnetic films.

CHAPTER 5. ORIGINS OF DAMPING IN FREE LAYERS OF TMR READERS

5.1 Overview

The magnetization in a magnetic material can precess around the direction of a static internal magnetic field, and such precession motion typically has a frequency in the microwave range. One can excite and maintain a uniform magnetization precession with an applied alternating microwave magnetic field. Once the microwave magnetic field is turned off, however, the magnetization will tend to relax back to the static equilibrium direction. Such magnetization relaxation can be realized through energy transfer out of the magnetic subsystem to non-magnetic subsystems such as phonons and electrons, energy redistribution within the magnetic subsystem, or energy transfer out of the magnetic material to external systems. Gilbert damping is mainly originated from the energy transfer from the magnetic subsystem to electrons which is named magnon-electron scattering. Two-magnon scattering process is a typical example of magnetization relaxation through energy redistribution within the magnetic subsystem, where one zero wavenumber magnon is extinguished and one non-zero wavenumber magnon is created. The excited non-zero wavenumber magnon is assumed to relax as soon as it is created. Therefore the two-magnon scattering relaxation rate directly contributes to the net magnetization relaxation rate. Spin pumping is considered as a form of energy transfer out of the magnetic material to external systems, which is widely observed in heterostructure samples with ultra-thin ferromagnetic layers. The magnetization precessions in the magnetic layer loss their angular momentums through injection of spin current into the adjacent non-metallic layers

such like Pt, Au, Cu, Ta, Ru, etc. The magnetizations relax back to static equilibrium by losing angular moments. The relaxation rate contributed from spin pumping is formalized in the similar way as the Gilbert damping contribution, therefore, the spin pumping contribution is usually observed as an enhancement in the Gilbert damping.

In tunnel magneto-resistance (TMR) readers, the damping in the free layers plays critical roles in the performance of the readers (Smith 2009). It affects, for example, both the response speed and signal-to-noise ratio of the TMR readers. In spite of such significance, understanding of physical relaxation processes in real free layers has been rather limited. Recent work studied the thickness dependence of damping for a CoFeB free layer in a TMR structure (Liu 2011) and the effects of dipolar coupling with the pinning layer on the ferromagnetic resonance of a NiFe free layer (Schäfer 2012). In both the studies, however, the free layers consisted of a single magnetic layer and was therefore far simpler than the complex multi-layered structure used in real TMR reader devices.

This chapter reports for the first time the damping properties of a free layer made of the same stacking structure and capped with the same non-magnetic layers as in present TMR readers. The study involved frequency- and angle-dependent ferromagnetic resonance (FMR) measurements and the numerical fitting of FMR linewidths with components responsible for different processes. The results indicate that, when the free layer is magnetized with an out-of-plane field, the FMR linewidth consists of a large contribution from Gilbert-type damping and a small contribution from inhomogeneity line broadening. The obtained Gilbert damping

constant is $\alpha \approx 0.0081$. This value is slightly larger than the intrinsic damping constant (Scheck 2006, Kuanr 2004), possibly due to spin pumping. When the field is applied in a direction away from the film normal, there is also a contribution from two magnon scattering (Urban 2001, Kalarickal 2008, Lenz 2006, Lindner 2009) , which, however, is smaller than the Gilbert damping contribution. The static properties yielded from the FMR measurements for various configurations show perfect consistency.

5.2 Ferromagnetic resonance and damping mechanism of free layers of TMR readers

The sample was prepared by magnetron sputtering and consists of a 6.8-nm-thick magnetic stack of NiFe/CoFeB/CoFe capped by a 9-nm-thick non-magnetic stack of Ru(2 nm)/Ta(2 nm)/Ru(5 nm). For the FMR measurements, the sample was cut into a 4-mm-long, 4-mm-wide rectangle piece. The frequency-dependent FMR measurements were carried out with a Ku-band shorted rectangular waveguide, while the angle-dependent measurements used either the Ku-band shorted waveguide or an X-band rectangular cavity. All the measurements made use of field modulation and lock-in detection techniques.

Figure 1 presents the FMR field (H_{FMR}) data. Figure 1(a) gives H_{FMR} as a function of frequency (f) obtained with an external magnetic field (H) applied normal to the sample plane, as indicated. The dots show the data, while the line shows a fit to the Kittel equation

$$f = |\gamma|\left(H_{\mathrm{FMR}} - 4\pi M_{\mathrm{s}}\right) \tag{5.1}$$

where $|\gamma|$ is the absolute gyromagnetic ratio and $4\pi M_{\mathrm{s}}$ is the saturation induction. One sees an almost perfect fit. The fitting yielded $|\gamma|$=2.95 MHz/Oe and $4\pi M_{\mathrm{s}}$ =12.19 kG. The $|\gamma|$ value

was slightly larger than the standard value (2.8 MHz/Oe), as reported previously for other metallic thin films. The $4\pi M_s$ value is as expected for the free layer in TMR readers. Figure 1(b) presents H_{FMR} as a function of the in-plane field angle (ϕ). These data, shown in dots, were obtained by rotating the field in the sample plane with the frequency fixed at f=13 GHz. The data indicate the existence of a weak in-plane uniaxial anisotropy. The curve in graph (b) shows a fit to

$$f = |\gamma| \sqrt{\left[H_{FMR} + H_u \cos(2\phi)\right]\left[H_{FMR} + H_u \cos^2\phi + 4\pi M_s\right]} \tag{5.2}$$

where H_u is the effective anisotropy field. The fitting made use of the above-cited $|\gamma|$ and $4\pi M_s$ values and yielded H_u =20 Oe.

Figure 1(c) presents H_{FMR} as a function of f obtained with the magnetic field applied along the in-plane easy axis. The dots show the data, while the curve shows the response calculated using Eq. (5.2) with ϕ=0 and the other parameters cited above. Figure 1(d) presents H_{FMR} as a function of the polar angle (θ) of the field, which was measured at f=9.46 GHz. The dots show the data, and the curve shows a response calculated using

$$\begin{aligned} f = |\gamma| &\left[H_{FMR}\cos(\theta - \theta_M) - 4\pi M_s \cos(2\theta_M)\right]^{1/2} \\ &\cdot\left[H_{FMR}\cos(\theta - \theta_M) - 4\pi M_s \cos^2\theta_M\right]^{1/2} \end{aligned} \tag{5.3}$$

and the above-cited parameters. Note that in Eq. (5.3) θ_M denotes the angle of the magnetization relative to the normal direction of the sample plane at the equilibrium and satisfies $H\sin(\theta_M - \theta) = 4\pi M_s \sin\theta_M \cos\theta_M$. Note also that the weak anisotropy field H_u is neglected in Eq. (5.3). One can see from graphs (c) and (d) nearly perfect agreements between the

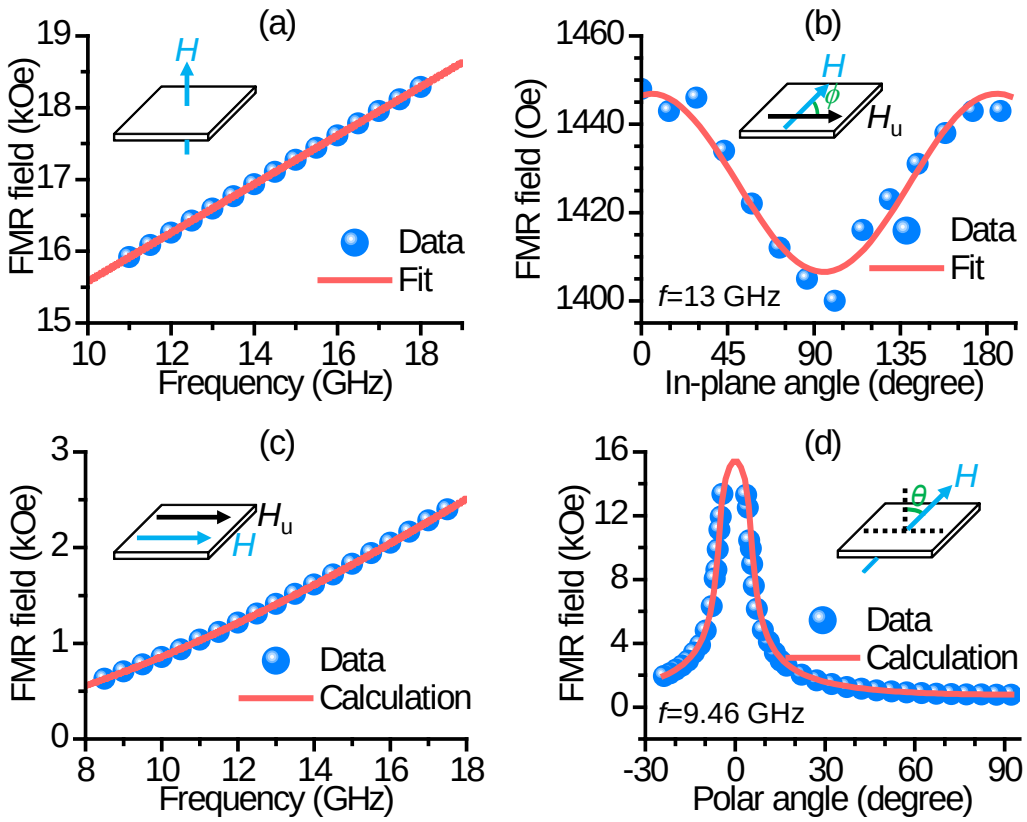

FIG. 5.1. FMR field (H_{FMR}) data obtained with various field configurations. (a) H_{FMR} as a function of frequency (f) for an external field (H) applied normal to the sample plane. (b) H_{FMR} as a function of in-plane field angle (ϕ). (c) H_{FMR} as a function of f for a field applied along the in-plane easy axis. (d) H_{FMR} as a function of the polar angle (θ) of the field. The dots show the data. The curves in (a) and (b) show the theoretical fits, while the curves in (c) and (d) show the calculated responses.

experimental and calculated responses, which confirm the parameters yielded from the above-described fitting.

Figure 2 gives the FMR linewidth (ΔH) data of the sample. The dots in Figs. 5.2(a) and (b) show ΔH as a function of f for the external field applied normal to the sample plane and along

the in-plane easy axis, respectively. The dots in Fig. 5.2(c) show ΔH as a function of θ measured at f=9.46 GHz. All the ΔH data are the half-power linewidth values determined by fitting the FMR power absorption profiles with a Lorentzian trial function.

The line in Fig. 2(a) shows a numerical fit to

$$\Delta H = \frac{2\alpha}{|\gamma|} f + \Delta H_{\mathrm{ILB}} \tag{4}$$

where ΔH_{ILB} describes inhomogeneity line broadening (ILB). One can see an almost perfect linear fitting. The fitting yielded α=8.13×10^{-3}. This damping originates mainly from magnon-electron scattering and magnon-phonon scattering, with the former largely dominating the latter due to the metallic nature of the free layer. The α value is slightly higher than that expected for transition metals, such as 0.0075 for Permalloy**Error! Bookmark not defined.** and 0.0043 for Fe. This slight damping enhancement is most likely due to spin pumping from the free layer to the capping layers. Spin pumping can make rather substantial contributions to damping in many systems, such as Fe/Pd. In the present free layer sample, however the spin-pumping contribution is small because the thicknesses of the Ru and Ta capping layers are smaller than the corresponding spin diffusion lengths (λ_{Ru}≈4 nm and λ_{Ta}≈10 nm).

The fitting of the data in Fig. 5.2(a) also yielded ΔH_{ILB}=22.0 Oe. This contribution to ΔH is not a loss. It arises from the superposition of local FMR profiles for different regions of the sample which have slightly different magnetic properties. Considering weak anisotropy in the sample, one can attribute ΔH_{ILB} mainly to the spatial variation of $4\pi M_{\mathrm{s}}$ and thereby can evaluate it as

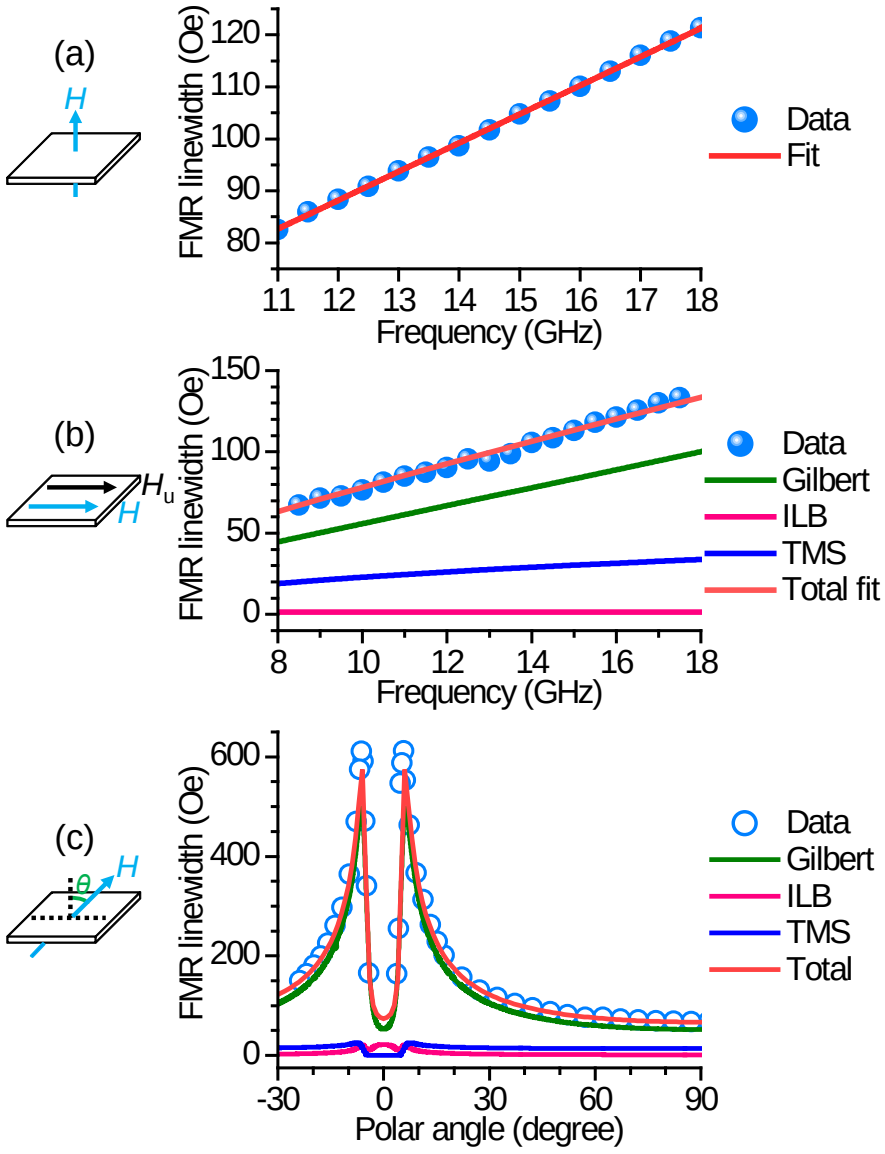

FIG. 5.2. FMR linewidth (ΔH) data obtained with three different field configurations. (a) ΔH as a function of f for an external field (H) applied normal to the sample plane. (b) ΔH as a function of f for a field applied along the in-plane easy axis. (c) ΔH as a function of θ for f=9.46 GHz. The dots show the data. The lines and curves in (a) and (b) show numerical fits. The curves in (c) show the calculated responses for the total linewidth and its four components.

$$\Delta H_{\mathrm{ILB}} = \left| \frac{\partial H_{\mathrm{FMR}}}{\partial \left(4\pi M_{\mathrm{s}}\right)} \right| \Delta \left(4\pi M_{\mathrm{s}}\right) \tag{5.5}$$

where the derivative is determined by Eq. (5.3) and $\Delta(4\pi M_s)$ denotes the width of the distribution of the local saturation induction. For the data shown in Fig. 5.2(a), one has the derivative equal to 1. Thus, ΔH_{ILB}=22.0 Oe indicates $\Delta(4\pi M_s)$=22.0 G and $[\Delta(4\pi M_s)]/(4\pi M_s)$=0.18%, which suggest weak inhomogeneity in the sample.

The data in Fig. 5.2(b) also show a nearly linear response, as those in Fig. 5.2(a), but they are notably larger than the values calculated with Eqs. (5.4) and (5.5) and the parameters cited above. This difference results from two-magnon scattering (TMS). For a magnetic thin film, the TMS process is prohibited when the field is normal to the film plane (θ=0) but is allowed when the field is not normal ($\theta\neq$0). One can express the linewidth for the $\theta\neq$0 configuration as

$$\Delta H = \frac{2\alpha}{|\gamma|} f + \Delta H_{TMS} + \Delta H_{ILB} \tag{5.6}$$

where ΔH_{TMS} denotes the contribution of the TMS process. For the analysis in this work, one assumes that the TMS process occurs due to the random grain-to-grain variation in the anisotropy field and the corresponding linewidth takes the following form

$$\Delta H_{TMS} = \frac{|\gamma|\xi^2 H_a^2}{P} \iint \Lambda[1+(k\xi)^2]^{-\frac{3}{2}} \delta(f - f_k) d^2k \tag{5.7}$$

where ξ denotes the mean grain size, H_a is the effective cubic anisotropy field in the grains, and P is equal to $\partial f/\partial(|\gamma|H_{FMR})$ and accounts for the conversion between frequency- and field-swept linewidths. The integral in Eq. (5.7) folds in the scattering from the uniform mode to all available degenerate spin-wave modes with wavenumber k and frequency f_k. Inside the integral, the Λ function takes into account the ellipticity of the precession response, the second term

specifies the k dependence of the scattering for a given ξ value, and the delta function serves to select out the degenerate modes. A full discussion of the grain-to-grain TMS theory is given in Chapter 3.

The curves in Fig. 5.2(b) show a fit to Eq. (5.6). The Gilbert and ILB components were calculated using the parameters cited above, while the TMS response is a fit to Eq. (5.7). There were only two parameters involved in the fitting, where were ξ and H_a. One can see that the overall fitting to the data is almost perfect. The fitting yielded ξ=4.5 nm and H_a=947 Oe, which were both reasonable values. One can also see that the TMS contribution is definitely non-trivial, although it is about 2.5 times smaller than the Gilbert contribution. Two notes should be made. First, the TMS curve in Fig. 5.2(b) is nonlinear although it seems linear. This nonlinear behavior becomes much clear if one expands the frequency scale (the horizontal axis), for example, to 2-20 GHz. Second, the fitting yielded anisotropy field is for individual grains, and the overall anisotropy field of the entire sample is significantly smaller due to the random orientation of the anisotropy axes of the grains.

The curves in Fig. 5.2(c) are not numerical fits. Rather, they are the responses calculated with the parameters cited above. The ILB and TMS responses were calculated using Eqs. (5.5) and (5.7), respectively. The Gilbert response (ΔH_α) was calculated with

$$\Delta H_{\mathrm{ILB}} = \left| \frac{\partial H_{\mathrm{FMR}}}{\partial \left(4\pi M_{\mathrm{s}}\right)} \right| \Delta \left(4\pi M_{\mathrm{s}}\right) \tag{5.8}$$

where the derivative was determined by Eq. (5.3) and was evaluated at θ=90°, and $\Delta(4\pi M_s)$ is the width of the distribution of the local saturation induction. One can see that the theoretical

results perfectly agree with all the experimental data except for two data points with the largest linewidth. This agreement undoubtedly validates the above-described fitting analysis.

5.3 Summary

In summary, this chapter reported experimental and numerical studies on the damping properties in the free layer of present TMR readers. The studies indicate that the free layer shows a Gilbert damping constant of 8.13×10^{-3}. When the free layer is magnetized with a field which is not normal to the film plane, there exists also two-magnon scattering. This scattering process, however, makes a contribution to the relaxation much smaller than the Gilbert contribution. When the free layer is magnetized by an in-plane field, the TMS component of the FMR linewidth is about 2.5 times smaller than the Gilbert component.

CHAPTER 6. TUNING OF DAMPING IN FERROMAGNETIC THIN FILMS THROUGH SEED LAYERS

6.1 Overview

The tailoring of the magnetization relaxation rate in ferromagnetic thin films is of great fundamental and practical significance. In practical terms, for example, the relaxation rates in thin film materials used in magnetic recording heads and media set a natural limit to the data recording rate; and the bandwidth, insertion loss, and response time of a magnetic thin film-based microwave device are critically associated with the relaxation rate in the film.

In the perspective of magnetic recording, the recording data rate has been pushed by the whole hard disk drive industry for years. Especially for enterprise products, high data rates are even more significant than high area densities. The recording data rate is limited mainly by two factors: (1) the switching speed of the magnetizations near the writer pole tip and (2) the magnetization resonance-induced reader noise. Low damping is desired for the writer material since the writer switching speed is dominated by the velocity of the domain wall motion. On the other hand, large damping is desired for the reader material as fast magnetization relaxation gives less magnetization ringing and less noise.

For magnetic thin film-based microwave device, such like band-pass filters and band-stop filters, the operation frequency is normally determined by the FMR frequency of the magnetic material, and the damping is the key variable to tune the bandwidth. Previous work has demonstrated three approaches for the tuning of relaxation rate in ferromagnetic thin films: (1)

control of film thickness, (2) addition of non-magnetic elements, and (3) doping of rare earth elements. Regarding (1), the tuning of relaxation rate relies on the sensitivity of two-magnon scattering and eddy current effects on the film thickness. Regarding (2), one makes use of the addition of non-magnetic elements to control the microstructural properties of the films and, thereby, control the two-magnon scattering processes. Regarding (3), the relaxation rates are enhanced through the slow relaxing impurity mechanism. These approaches, however, are not practically desirable. Approach (1) sets a limit to film thickness for a specific relaxation rate. For (2) and (3), the change in relaxation rate is always accompanied by significant changes in other film properties, such as saturation induction $4\pi M_s$. It should be noted that the two-magnon scattering processes in thin films are critically associated with film microstructures, such as defects, grain size, and surface roughness. As discussed in chapter 3, both the relaxation rate and frequency dependent behavior are significantly impacted by the average grain size and standard deviation of grain size distribution. The two-magnon scattering processes manifest themselves in a broadening in the FMR linewidth and nonlinear behavior in the linewidth vs. frequency response, rather than linear behavior expected by the Gilbert damping model. It is also possible that the processes give rise to a saturation response or even a decrease in the linewidth as one move to higher frequencies.

6.2 Fe-Co alloy thin films

The $Fe_{65}Co_{35}$ films were deposited at room temperature by dc magnetron sputtering. The substrates were (100) Si wafers with a 300-nm-thick SiO_2 capping layer. Prior to the growth of

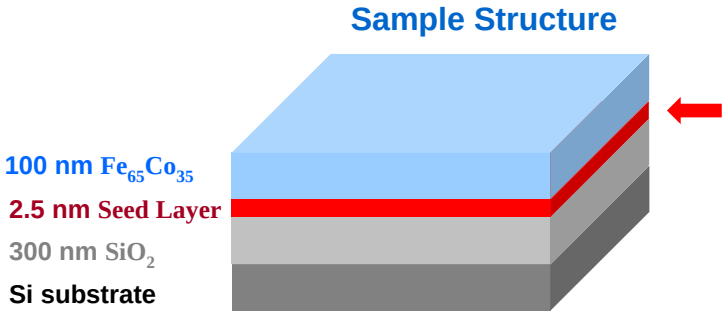

Seed Layer	Structure
Cr	bcc
Ta	bcc
Pt	fcc
Cu	fcc
Ti	hcp
Ru	hcp

FIG. 6.1. Schematic of an Fe-Co alloy film structure. The composition and the nominal thickness for each layer are listed on the left of the sample structure. The table on the right lists the elements and corresponding crystalline structures of the seed layers.

each film, a thin seed layer was deposited which has a nominal thickness of 2.5 nm. The sample structure is illustrated in Fig. 6.1. During the film deposition, a field of 80 Oe was applied to induce an in-plane uniaxial anisotropy in the magnetic layer. The nominal thicknesses of the $Fe_{65}Co_{35}$ films are 100 nm. The grain size and grain-size distribution for Fe-Co layer of each film were determined by transmission electron microscopy (TEM). The statistic results from the TEM measurements are shown in Fig. 6.2. The static magnetic properties were measured by vibrating sample magnetometry. The FMR measurements were carried out by shorted rectangular waveguides over a frequency range of 8.2 to 18.0 GHz. The peak-to-peak field separation in each power absorption derivative profile was taken as the derivative of FMR linewidth, which is named as linewidth throughout this chapter. Ten series samples are prepared for this particular study, six of them contain different types of seed layers and the same seed layer thickness, as indicated in Fig. 6.1. The other four samples have the

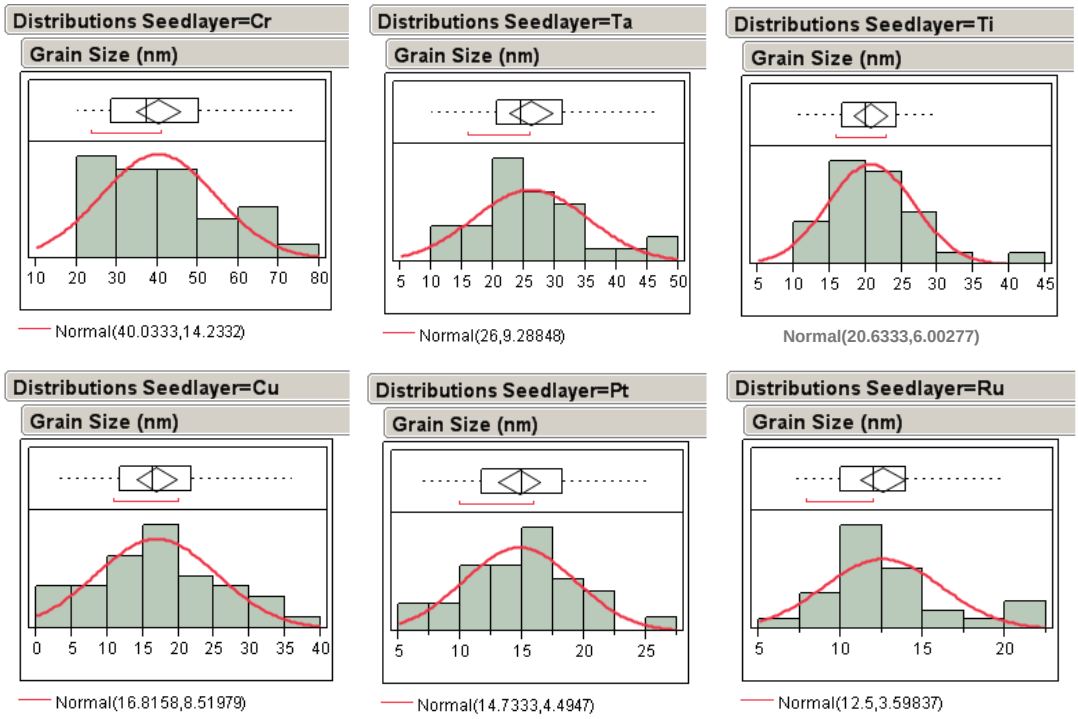

FIG. 6.2. Statistic data of the grain size distribution for the Fe-Co layer measured by transmission electron microscopy. The data are for six samples with different types of seed layers, as indicated. In each diagram, the horizontal axis shows the grain size in the unit of *nm*, the bar height indicates the counts of the grains, the red curve is the normal distribution fit, and the numbers in the bracket corresponds to the average grain size (left) and the standard deviation of grain size distribution (right).

same seed layer (Ru) and different seed layer thickness. The sample properties for all the samples are investigated with the methods mentioned above, and the results are listed in table 6.1.

Table 6.1 provides the details of the samples. Column 1 gives the label for all the samples. Ten samples with different seed layer features are investigated, samples labeled from 1 to 6 are

Fe-Co films deposited on different seed layer elements with 2.5 nm seed layer thickness, which are shown in figure 6.1 and 6.2. In addition, samples labeled from 7 to 10 are Fe-Co films deposited on Ru seed layers with different seed layer thicknesses. Column 2 gives the material, nominal structure, and nominal thickness (nm) of each seed layer. Column 3 gives the values of average grain size d (left) and standard deviation of grain size distribution σ/d (right) for the Fe-Co layer. These values vary significantly with the seed layer, but are relatively independent of the seed layer thickness (except for sample 9). Column 4 lists the $4\pi M_s$ values for Fe-Co layer, which are all close to each other. The average value is 23.1 kG, which matches the values previously reported and is used in the numerical analyses. The small variation in $4\pi M_s$ is probably due to the deviation of the Fe-Co film thickness from the nominal value, which is in the 5% range. Column 5 gives the coercivity values measured along the easy and hard axis. Column 6 gives the uniaxial magnetic anisotropy field H_u values for Fe-Co layer, all of which are smaller than 40 Oe. Column 6 also gives the absolute values of gyromagnetic ratio γ, which are close to each other. The uniaxial magnetic anisotropy field and gyromagnetic ratio values were obtained through fitting the measured FMR field vs. frequency responses with the Kittel equation (eq. 6.1). These fitting parameters are shown with underlines in order to differentiate them from the experimental data in column 6.

$$\omega = |\gamma| \sqrt{(H_{ext} + H_u)(H_{ext} + H_u + 4\pi M_s)} \tag{6.1}$$

Table 6.1. Summary of sample properties.

Label	Seed layer & Thickness (nm)	Grain size d (nm) & Standard deviation σ/d	$4\pi M_s$ (kG)	Coercivity (Oe) Easy & Hard	H_u (Oe) & $\lvert\gamma\rvert/2\pi$ (MHz/Oe)
1	Cr, bcc, 2.5	40, 0.355	23.5	80.4, 77.8	37.8, 2.93
2	Ta, bcc, 2.5	26, 0.354	23.1	67, 64.4	28.0, 2.93
3	Pt, fcc, 2.5	14.7, 0.299	22.4	22.9, 15.0	12.8, 2.90
4	Cu, fcc, 2.5	16.8, 0.506	23.4	19.0, 10.4	17.9, 2.92
5	Ti, hcp, 2.5	20.6, 0.291	22.8	46.1, 39.9	9.8, 2.90
6	Ru, hcp, 2.5	12.5, 0.28	23.7	20.8, 7.0	23.4, 2.93
7	Ru, hcp, 10	13.3, 0.293	22.7	24.5, 10.0	25.3, 2.93
8	Ru, hcp, 5	10.5, 0.429	23.4	24.0, 8.8	29.0, 2.93
9	Ru, hcp, 2	12.5, 0.28	23.1	23.4, 7.4	20.5, 2.93
10	Ru, hcp, 0.5	12.6, 0.27	23.1	22.3, 4.8	24.2, 2.93

6.3 Tuning of damping in Fe-Co films

This chapter reports on the tuning of relaxation rate in ferromagnetic thin films through the use of different types of seed layers. Specifically, the chapter presents experimental and numerical results that demonstrate the tuning of relaxation rate, both the magnitude and frequency dependence, in 100-nm-thick $Fe_{65}Co_{35}$ films through seed layers. It is found that the use of different types of seed layers leads to films with different grain sizes and grain-size distributions for Fe-Co layers, as shown in figure 6.2. The difference in the film grain properties results in a difference in the levels of both grain-to-grain two-magnon scattering and grain-boundary two-magnon scattering processes, as discussed in chapter 3. As a result, the films grown on different seed layers show different relaxation properties, which manifest themselves as different FMR linewidth properties. It is also found that the films on different types of seed layers show similar static magnetic properties (as shown in table 6.1), although

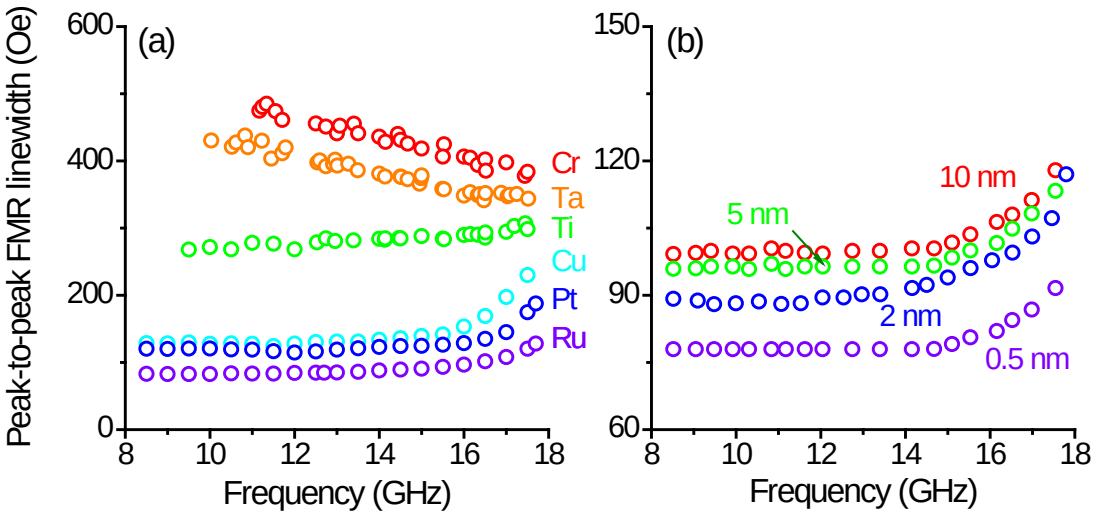

FIG. 6.3 FMR linewidth vs. frequency responses for films grown (a) on different types of 2.5-nm-thick seed layers and (b) on Ru seed layers of different thicknesses.

they differ significantly in relaxation rate (will be shown later). These results clearly demonstrate a simple and practical approach for the control of relaxation properties in ferromagnetic thin films.

Figure 6.3 shows the linewidth vs. frequency responses. Graph (a) shows the data for films deposited on different types of seed layers with the same thickness (2.5 nm), as indicated. Graph (b) shows the data for films deposited on Ru seed layers of different thickness, as indicated. Four important results are evident in Fig. 1. (1) By using different seed layers, one can tune the magnitude of linewidth over a rather wide range of 80-490 Oe. (2) Films on different seed layers also show significantly different linewidth-frequency responses. (3) None of those responses shows linear behavior with a zero linewidth intercept at zero frequency, as expected by the Gilbert damping model. (4) For a given type of seed layer, a change in the seed

layer thickness leads to a notable change in the magnitude of linewidth, but produces negligible effects on the frequency dependence of linewidth.

These results clearly indicate the feasibility of tuning the FMR linewidth properties of the $Fe_{65}Co_{35}$ films via the use of different seed layers. They, however, provide no details on the effects of the seed layer on physical relaxation processes in the Fe-Co films. To understand such effects, numerical analyses are carried out as explained below.

The experimental linewidth ΔH usually takes the form as Eq. (6.2).

$$\Delta H = \Delta H_{\mathrm{r}} + \Delta H_{\mathrm{ILB}} \tag{6.2}$$

ΔH_{r} originates from the magnetization relaxation and ΔH_{ILB} takes into account the sample inhomogeneity-caused FMR line broadening. The term linewidth ΔH can be related to relaxation rate η as Eq. (6.3).

$$\Delta H_{\mathrm{r}} = \frac{2\eta}{\partial \omega_{\mathrm{FMR}} / \partial H} \tag{6.3}$$

ω_{FMR} is the FMR frequency. In this work, one considers three contributions to linewidth (and relaxation rate): (1) Gilbert damping, (2) grain-to-grain two-magnon scattering relaxation, and (3) grain-boundary two-magnon scattering relaxation. The Gilbert damping results mainly from magnon-electron scattering, and contributions from magnon-phonon scattering, eddy current, and spin pumping effects are relatively weak. The term ΔH_{ILB} in Eq. (1) is not a loss. Rather, it arises from the simple superposition of several local FMR profiles for different regions of the film, as discussed in chapter 3. If the inhomogeneity is strong and ΔH_{ILB} is comparable to ΔH_{r}, Eq. (6.3) is inappropriate and the combined linewidth ΔH should take as Eq. (6.4).

$$\Delta H = \frac{\Delta H_r^2 + 1.97\Delta H_r \Delta H_{ILB} + 2.16\Delta H_{ILB}^2}{\Delta H_r + 2.16\Delta H_{ILB}} \quad (6.4)$$

The discussions below were based on Eq. (6.3). Fig. 6.4 and 6.5 show the results from the fitting of the measured linewidth data with four linewidth contributions described above. The fitting used a Gilbert damping constant a=0.003, an exchange constant A=1.25×10^{-6} erg/cm, which was 30% lower than that previously reported, and a magneto-crystalline anisotropy field H_a=960 Oe, which was close to that previously reported. The values of ΔH_{ILB}, d, σ/d, and grain boundary surface anisotropy constant K_s used in the fitting are given in Table 6.2. The use of higher Gilbert damping constant values resulted in poor fits, which are not shown in the figures.

Table 6.2. Summary of fitting parameters.

Label	d (nm)	σ/d	K_s *(erg/cm^2)*	ΔH_{ILB} *(Oe)*
1	36	0.278	0.438	100
2	30	0.233	0.324	80
3	14	0.118	0.438	70
4	15	0.1	0.45	80
5	20	0.4	0.258	70
6	12.5	0.145	0.438	30
7	12.7	0.134	0.438	50
8	12.5	0.136	0.438	45
9	12.2	0.144	0.438	38
10	12.3	0.133	0.438	25

In Fig. 6.4, graphs (a) and (b) show the total fits of the linewidth data and the four components for the films on Ru (2.5 nm) and Cr seed layers, respectively. Graph (c) shows the theoretical fits (curves) to all the linewidth data shown in Fig. 1(a). Graph (d) shows the relaxation rate η values obtained with a two-step procedure: (i) calculation of ΔH_r using equation 6.4 with the

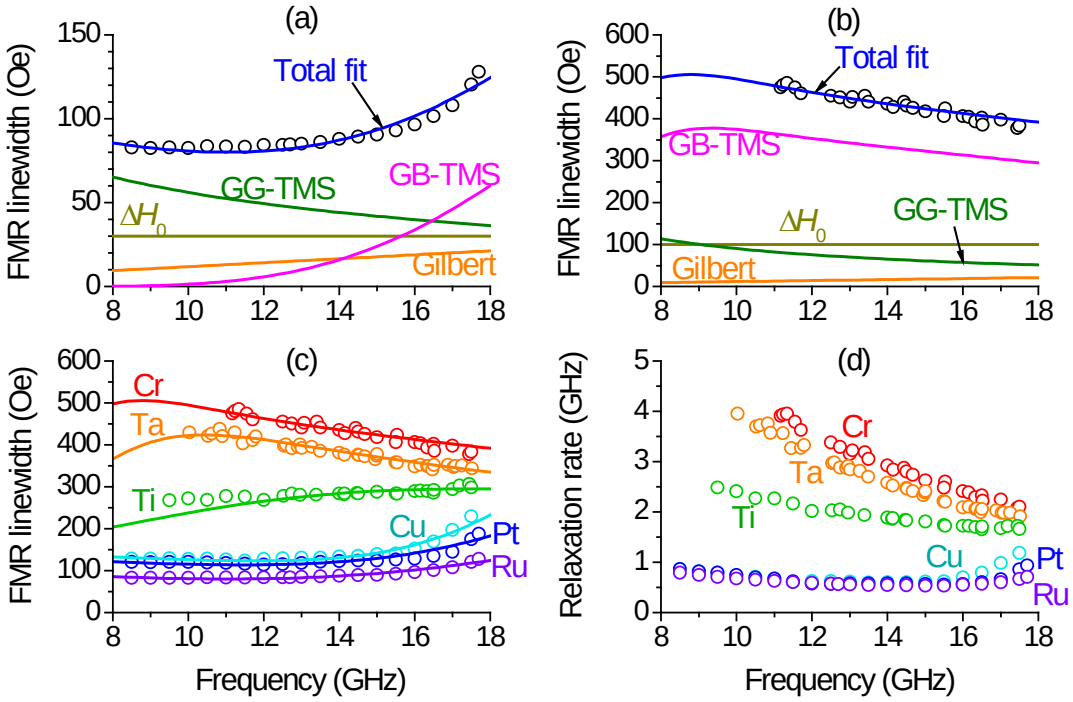

FIG. 6.4. Theoretical fits of linewidth vs. frequency responses and relaxation rates for films grown on different seed layers. (a) Film on Ru seed layer. (b) Film on Cr seed layer. (c) Linewidth vs. frequency data and fits for the six films. (d) Relaxation rate vs. frequency responses for the six films.

experimental linewidth values and the ΔH_{ILB} values from the fitting and (ii) calculation of η using equation 6.3. The data in figure 6.4 indicate three important results. First, through the use of different seed layers, one can tune η over a rather wide range from 0.5 GHz to 4 GHz as well as its frequency dependence, as shown in (d). Second, this tuning relies on the changes of the grain-to-grain two-magnon scattering and grain-boundary two-magnon scattering processes with the seed layer, as shown representatively in (a) and (b). Third, the dominant contributions to the relaxation are from the two-magnon scattering processes, whereas the contribution from Gilbert damping is relatively small.

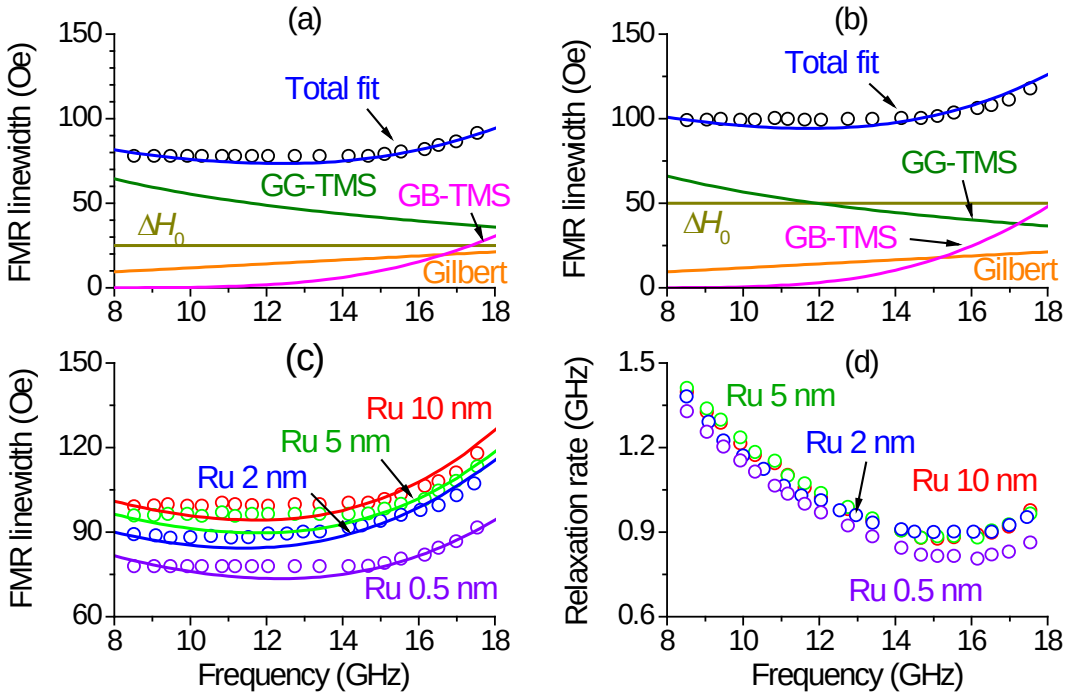

FIG. 6.5. Theoretical fits of FMR linewidth vs. frequency responses and relaxation rates for films grown on Ru seed layers of different thickness, as indicated. (a) Film on 0.5 nm Ru seed layer. (b) Film on *10 nm* Ru seed layer. (c) Linewidth vs. frequency data and fits for the four films. (d) Relaxation rate vs. frequency responses for the four films.

In Fig. 6.5, graphs (a) and (b) show the total fits of the linewidth data and the four components for the films on 0.5 nm and 10 nm thick Ru seed layers, respectively. Graph (c) shows the fits to all the linewidth data shown in Fig. 1(b). Graph (d) shows the corresponding η values obtained with the procedure described above. Two important results are evident in figure 6.5. First, a change in the Ru seed layer thickness results in negligible effects on the two-magnon scattering processes, as shown in (a) and (b), and thereby gives rise to insignificant changes in the relaxation properties, as shown in (d). Second, the seed layer thickness change

results in a notable change in ΔH_{ILB} and a corresponding change in ΔH. There are two important points to be emphasized. (1) The d values used in the fitting were all close to the experimental values. Most of the fitting σ/d values were smaller than the experimental values, and this is probably due to the relatively small numbers of grains (about 30) used in the statistical analyses of the grain properties. Nevertheless, the relative differences in σ/d between the samples are consistent with those from the measurements. These facts strongly support the interpretation of the mechanism of the presented relaxation tuning. (2) The tuning relies on the fact that the grain-to-grain two-magnon scattering and grain-boundary two-magnon scattering processes are the dominant relaxation processes. For films much thinner than the films in this work, spin pumping is also an important damping source so that one can vary both the material and thickness of the seed layer to tailor the film relaxation rate.

6.4 Summary

In summary, this chapter reported the effects of seed layers on the relaxation and FMR responses of 100-nm-thick $Fe_{65}Co_{35}$ films. It was found that the use of different types of seed layers results in films with different relaxation rates, both in magnitude and frequency dependence, but similar static magnetic properties. No significant effects on the relaxation rate were observed when one varied the thickness of the Ru seed layer. These results can be interpreted in terms of the effects of the seed layers on the film grain properties and the correlation between the grain properties and the grain-to-grain two-magnon scattering and grain-boundary two-magnon scattering processes.

CHAPTER 7. DAMPING IN PERPENDICULAR RECORDING MEDIA

7.1 Overview

Understanding the damping of magnetization precession in magnetic recording media is of both fundamental and practical significance. From the practical perspective, the relaxation processes in media not only set a natural limit to the time of magnetization switching, but also play critical roles in microwave-assisted magnetization switching and domain wall-assisted switching (Zhu 2008, Heinonen 2008).

In spite of such importance, however, studies on damping in perpendicular media materials have been rather limited. There are four previous experimental studies on damping in perpendicular media-like materials. Mo (2008) and Mizukami (2010) both reported studies of damping in CoCrPt alloy thin films via ferromagnetic resonance (FMR) techniques. The Gilbert damping constant (α) values reported, however, differ by one order of magnitude: Inada (1997) reported a α range of 0.038-0.042, while Mo reported α=0.004. Mizukami also reported a damping study on CoCrPt alloy films, but with time-resolved magneto-optical Kerr effect techniques. It reported a α range of 0.05-0.06, which are close to the value reported in Inada's but is substantially larger than that in Mo's. Furthermore, Krivosik (2011) presented FMR studies in granular CoCr thin films and reported an α value of 0.004. This value matches that in reference[13] but disagrees with those in Mizukami's and Inada's.

Notwithstanding the inconsistent values for the damping constant, the samples used in those previous studies were significantly different from real perpendicular media. On one hand, the

films were all “soft”, with a coercivity or an anisotropy field much smaller than that in perpendicular media materials. On the other hand, the samples consisted of only a single magnetic layer, which is far simpler than the structure in the present media, such as the exchange coupled composite (ECC) structure. Essentially speaking, the damping in perpendicular media and the responsible physical relaxation processes have never been clarified so far, to the best of our knowledge.

This chapter reports the use of FMR measurements and numerical analyses to determine the damping constant in perpendicular media as well as to clarify the physical origins of the damping. The studies made use of a sample cut from a commercial quality 700-Gbit/in^2 media disk, included frequency (f)- and temperature (T)-dependent FMR measurements, and involved the numerical fitting of FMR linewidth data with components responsible for different relaxation processes. The f-dependent FMR data indicated α=0.056±0.002. The T-dependent FMR data showed α=0.05-0.15, which covers and therefore supports the value obtained from the f-dependent FMR study. Such damping constants consist of contributions from breathing Fermi surface-associated relaxation and spin-flip magnon-electron scattering, with the first process being slightly stronger than the second, and include no contributions associated with sample inhomogeneity.

7.2 Damping in exchange coupled composite media

This chapter reports damping properties in perpendicular recording media for the first time. The experiments made use of a sample cut from a commercial quality 700-Gbit/in^2 media disk.

The frequency-dependent ferromagnetic resonance (FMR) study indicated a Gilbert damping constant of α=0.056, and the temperature-dependent FMR study yielded α =0.05-0.15. These damping constants consist of contributions from breathing Fermi surface-associated relaxation and spin-flip magnon-electron scattering, with the first process being slightly stronger than the second, and include no contributions from two-magnon scattering.

Understanding the damping of magnetization precession in magnetic recording media is of both fundamental and practical significance. From the practical prospective, the relaxation processes in media not only set a natural limit to the time of magnetization switching, but also play critical roles in microwave-assisted magnetization switching and domain wall-assisted switching.

Notwithstanding the debating damping constant, the samples used in those previous studies were significantly different from real perpendicular media. On one hand, the films were all "soft", with a coercivity or an anisotropy field much smaller than that in perpendicular media materials. On the other hand, the samples consisted of only a single magnetic layer, which is far simpler than the structure in the present media, such as the exchange coupled composite (ECC) structure. Essentially speaking, the damping in perpendicular media and the responsible relaxation processes have never been clarified so far, to the best of our knowledge.

This subsection reports the use of FMR measurements and numerical analyses to determine the damping constant in perpendicular media as well as to clarify the physical origins of the damping. The studies made use of a sample cut from a commercial quality 700-Gbit/in2 media

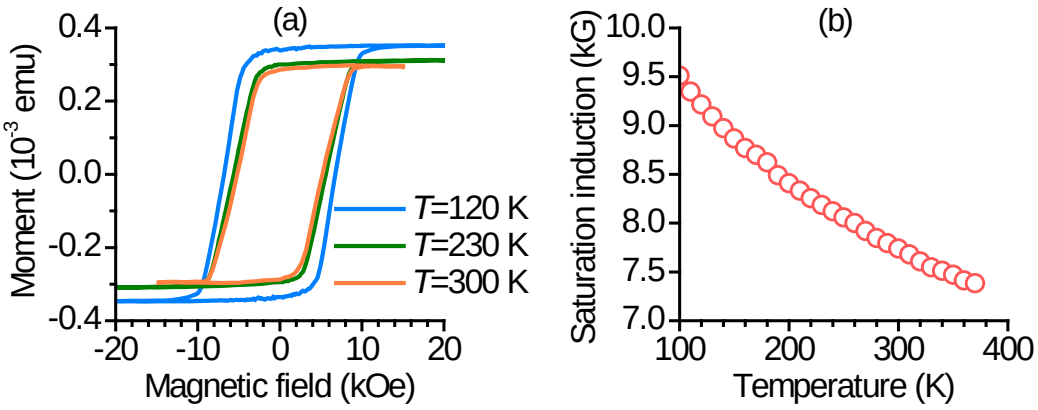

FIG. 7.1. Static magnetic properties of an ECC perpendicular media sample. (a) Hysteresis loops at three different temperatures. (b) Saturation induction ($4\pi M_s$) as a function of temperature.

disk, included frequency (f)- and temperature (T)-dependent FMR measurements, and involved the numerical fitting of FMR linewidth data with components responsible for different relaxation processes. The f-dependent FMR data indicated α=0.056±0.002. The T-dependent FMR data showed α=0.05-0.15, which covers and therefore supports the value obtained from the f-dependent FMR study. Such damping constants consist of contributions from breathing Fermi surface-associated relaxation and spin-flip magnon-electron scattering, with the first process being slightly stronger than the second, and include no contributions associated with sample inhomogeneity.

The sample was a 4 mm by 4 mm rectangle element cut from an ECC perpendicular media disk. The core components of the media include a 14-nm-thick granular “hard” magnetic layer, a 5-nm-thick continuous “soft” magnetic layer, and a 0.8-nm-thick exchange break layer

in-between the continuous and granular layers. Both of the two magnetic layers are CoCrPt-based films. The media layers were deposited on a glass substrate without any soft underlayers.

The static magnetic properties of the sample are shown in Fig. 7.1. Graph (a) shows the hysteresis loops measured by SQUID at three different temperatures, as indicated, with a magnetic field applied normal to the sample plane. The data indicate the coercivity fields of 6.8 kOe at 120 K, 5.6 kOe at 230 K, and 5.2 kOe at 300 K, which are typical for ECC perpendicular media. Graph (b) presents the effective saturation induction ($4\pi M_s$) as a function of temperature (T). The $4\pi M_s$ values were estimated based on the magnetic moments measured by SQUID and the thickness values cited above. One can see that, as T increases from 120 K to 370 K, $4\pi M_s$ decreases from 9.5 kG to 7.4 kG, which is as expected for ECC perpendicular media. Note that the determination of both the effective perpendicular anisotropy field (H_a) and the damping constant described below made use of the $4\pi M_s$ values presented in graph (b).

The section below will present the *f*- and *T*-dependent FMR data first and then discuss in detail the determination of the damping properties from the FMR data. Fig. 7.3 presents *f*-dependent FMR data measured by broadband vector network analyzer techniques at room temperature. The measurements made use of a 50 Ω co-planar waveguide (CPW) structure that consisted of a 100-μm-wide signal line and two grounds 50 μm away from the signal line. The sample was placed on the CPW structure, with the media side facing down and the substrate side facing up. Prior to the measurements, the sample was magnetized to saturation by an external

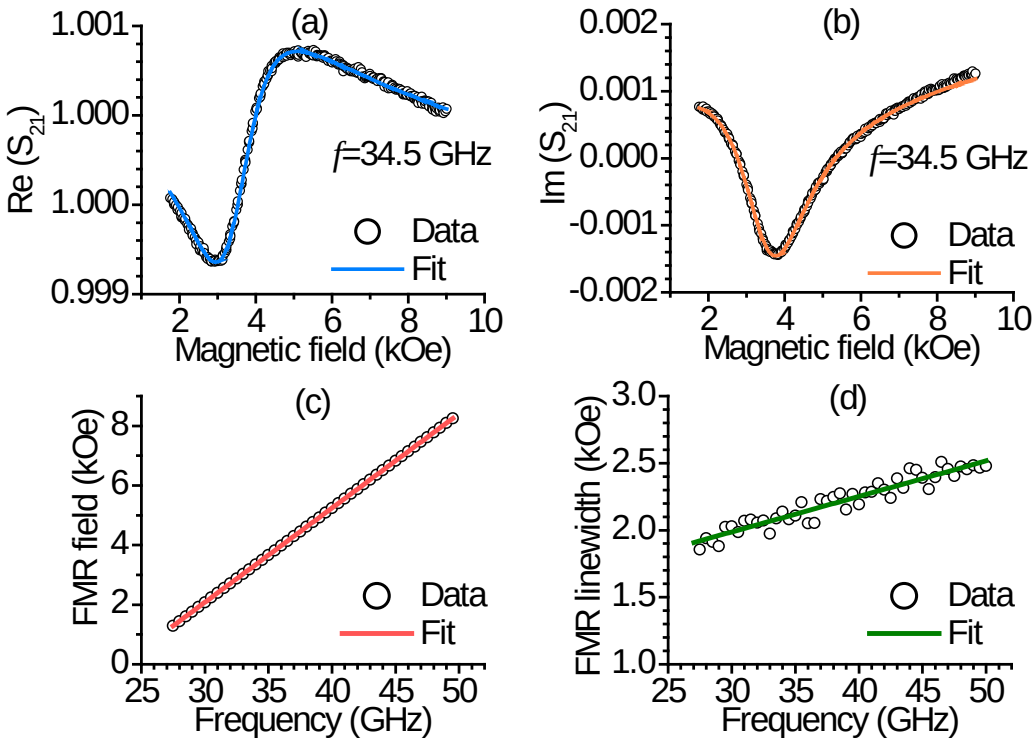

FIG. 7.2. Frequency-dependent FMR data. Graphs (a) and (b) show the real and imaginary parts, respectively, of a transmission response (S_{21}) of the CPW-sample structure. Graphs (c) and (d) show the FMR field and linewidth, respectively, as a function of frequency. In all the graphs, the circles show the data, while the curves and lines are numerical fits.

field of 20 kOe applied normal to the sample plane; during the measurements, the external field was applied along the same direction.

In Fig. 7.2, graphs (a) and (b) show the real and imaginary parts, respectively, of a representative transmission response (S_{21}) of the CPW-sample structure, which was measured by sweeping the field (H) at a fixed f, as indicated. The circles show the data, while the curves are numerical fits.**Error! Bookmark not defined.** The fitting yielded the field (H_{FMR}) and linewidth

(ΔH) values for the FMR at f=34.5 GHz. By carrying out measurements at different frequencies and performing similar fitting, one obtained the H_{FMR} and ΔH values at different frequencies. The circles in graphs (c) and (d) show the obtained H_{FMR} and ΔH data, respectively. The line in graph (c) is a fit to the Kittel equation

$$f = |\gamma|\left(H_{\mathrm{FMR}} + H_{\mathrm{a}} - 4\pi M_{\mathrm{s}}\right) \tag{7.1}$$

where $|\gamma|$ is the absolute gyromagnetic ratio. One can see that the fit is almost perfect. The fitting yielded H_{a}=15.15 kOe, which is as expected. The fitting also yielded $|\gamma|$=3.16 GHz/kOe. This value is higher than the standard value (2.80 GHz/kOe), but is very close to both the values reported for CoCrPt alloy thin films and granular CoCr thin films. The linear fitting in graph (d) is for the determination of the damping constant, which is described later.

Fig. 7.3 gives the T-dependent FMR data measured with a 9.48 GHz microwave cavity. The circles in graph (a) show a representative FMR response measured at T=300 K. Prior to the FMR measurement, the sample was magnetized to saturation by a field of 20 kOe applied normal to the sample plane; during the measurement, the field was applied in a direction opposite to the magnetization and was swept from 0 to 10 kOe. The measurement made use of field modulation and lock-in detection techniques, so the data in graph (a) show an FMR power absorption derivative profile. The curve in graph (a) shows a Gaussian fit for the major portion of the profile. The fitting yielded the H_{FMR} and ΔH values for the FMR at T=300 K. Similar measurements at different temperatures and subsequent fitting yielded the H_{FMR}-T and ΔH-T responses shown in graphs (b) and (c). The curves in graph (c) show the overall fit and

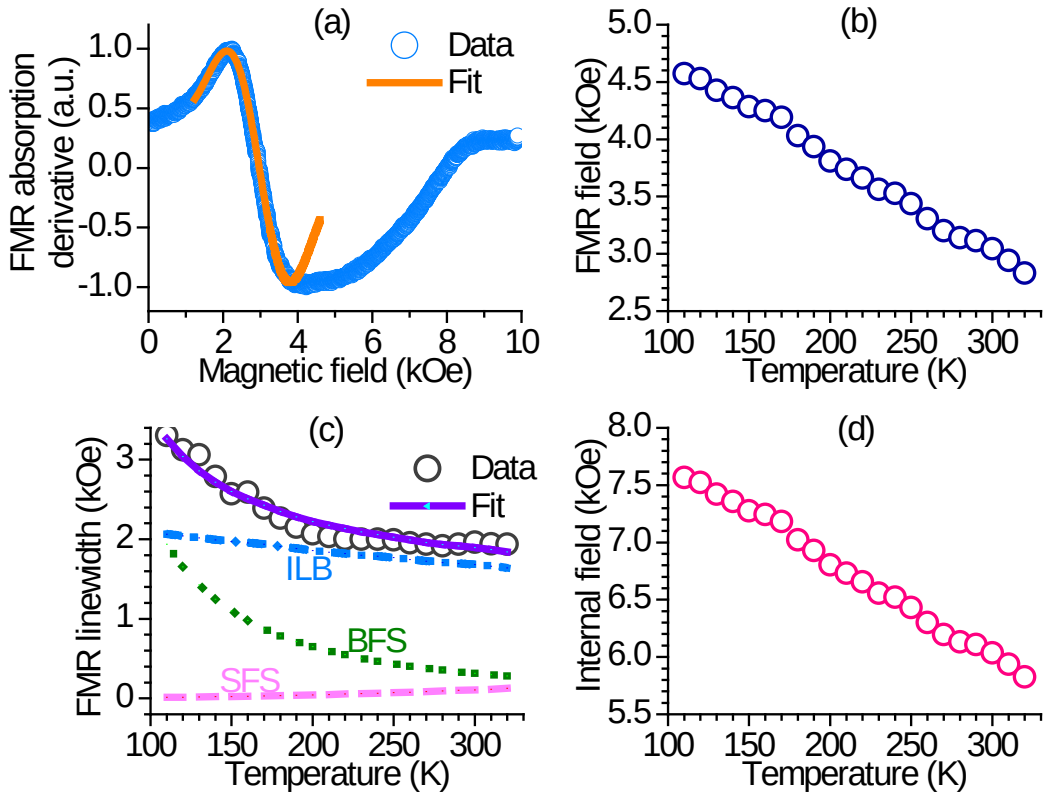

FIG. 7.3. Temperature (T)-dependent FMR data. (a) An FMR response measured at T=300 K. (b) H_{FMR} as a function of T. (c) ΔH as a function of T. (d) H_{int} as a function of T. The circles show the data, while the curves show the fits.

individual components of the ΔH data, which are discussed later. Graph (d) presents the effective internal field (H_{int}) as a function of T. These fields were estimated based on the H_{FMR} data in graph (b), the $|\gamma|$ value cited above, and the Kittel equation

$$f = |\gamma|(H_{int} - H_{FMR}) \tag{7.2}$$

It is worth to emphasize that the external field is parallel to the magnetization for the f-dependent FMR measurements but is anti-parallel to the magnetization for the T-dependent FMR measurements. As a result, the field plays opposite roles in the determination of the FMR

frequency, as shown in Eqs. (7.1) and (7.2). Two important observations should be pointed out about the data in Fig. 7.3. First, although the FMR response in graph (a) is clean and shows clearly-defined resonance behavior, it is abnormal in the high-field region (H>4 kOe). Second, the field H_{int} is slightly smaller than H_a-4πM_s. For example, at T=300 K one has H_{int}=6.04 kOe and H_a-4πM_s=7.41 kOe. These results are due to the facts that the H_a sigma is broadened by the antiparallel field, and the mean is pushed toward the lower value. The reversed grains do not undergo FMR. They, however, provide local dipolar fields to the un-reversed grains, which enhance H_{int}, shift the FMR to higher fields, and thereby broaden the FMR profile in the high-field regime.

It is fortunate that the above-described partial reversal has no effects on the ΔH measurements. Fig. 7.4 shows the evidence. Graph (a) shows four FMR profiles measured at T=300 K. Each profile was obtained with a three-step process: (1) magnetize the sample to saturation with a field of 20 kOe applied normal to the sample plane; (2) realize partial reversal with a field (H_r) anti-parallel to the magnetization in the sample; and (3) run FMR with a field which is in the same direction as H_r and is swept from 0 to 10 kOe. In graph (a), the reversal field H_r for each profile is indicated. Graphs (b) and (c) give the H_{FMR} and ΔH values obtained through the fitting of the profiles in graph (a), as done in Fig. 4(a). One can see that, as H_r is increased and more grains are reversed prior to the FMR measurements, H_{FMR} increases notably as expected, while ΔH remains almost constant.

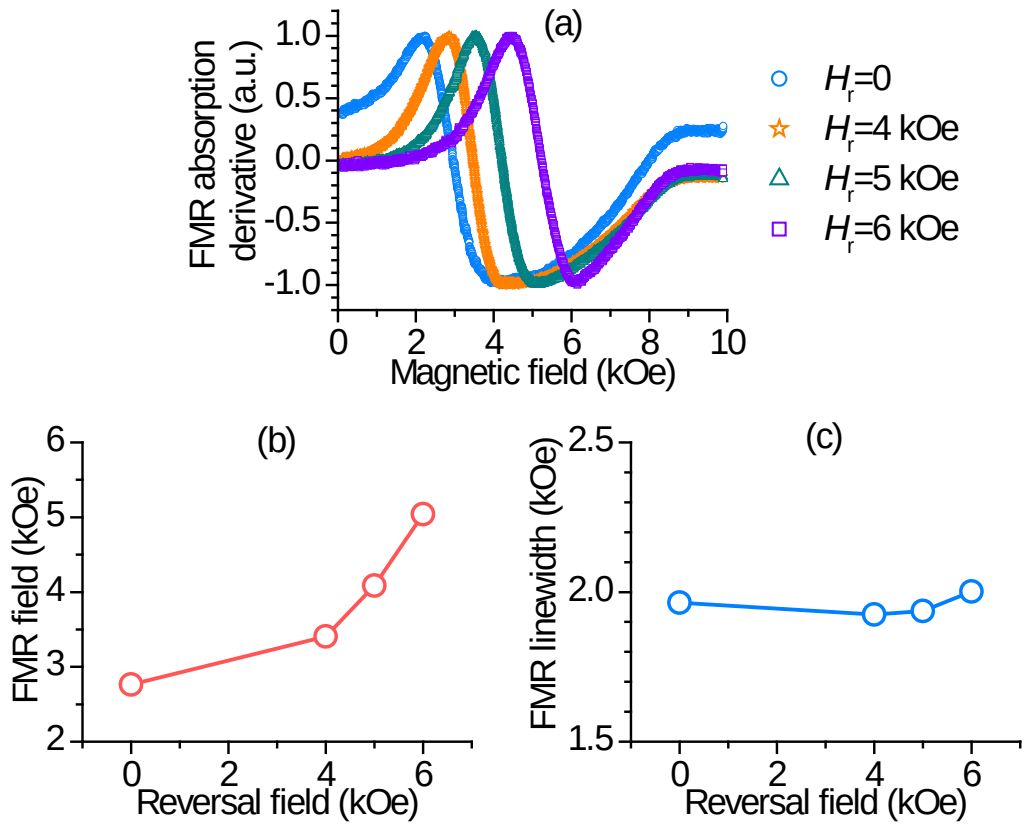

FIG. 7.4. Effects of initial partial reversal on the FMR properties. Different initial partial reversal conditions were realized by applying different reversal fields (H_r) prior to the FMR measurements.

Turn now to the extraction of the damping properties from the above-presented ΔH data. The origin of ΔH differs significantly in different materials. In general, one can express ΔH as $\left(\sum_i \Delta H_i\right) + \Delta H_{ILB}$, where ΔH_i denotes the contribution from a certain relaxation process i and ΔH_{ILB} takes into account the sample inhomogeneity-caused line broadening. The inhomogeneity line broadening is not a loss. It arises from the superposition of local FMR profiles for different regions of the sample. Those local FMR profiles are shifted in field because of the spatial variations of the magnetic properties. For the ECC perpendicular media,

possible relaxation processes include magnon-electron scattering, magnon-phonon scattering, two-magnon scattering, and eddy current-associated damping. As discussed below, the magnon-electron scattering plays a dominate role in the damping in the ECC perpendicular media. The magnon-phonon scattering occurs in all the materials but is expected to play a much weaker role than the magnon-electron scattering in the media. The two-magnon scattering results from film inhomogeneity (such as grain boundaries and voids) and makes a significant contribution when the field is far away from the film normal direction. It can be neglected in the present study since the fields were all normal to the sample plane during the FMR measurements. The eddy current damping is expected to be insignificant due to the fact that the media thickness is considerably smaller than the skin depth.

There are two types of magnon-electron scattering: one involves spin flips, and the other involves no spin flips but is associated with the breathing of the Fermi surface. In a spin-flip scattering (SFS) process, a spin-up free electron destroys a magnon, absorbs its energy and momentum, and changes into a spin-down electron. The process obeys both energy and momentum conservations. At very low temperatures, the process is very weak as the spin-up and spin-down electrons essentially share the same Fermi level, and the energy and momentum conservations cannot be satisfied. With an increase in T, however, the electron relaxation rate (τ^{-1}) increases roughly as T^2. This increase in the relaxation rate results in the broadening of the Fermi surface, and the latter facilitates the energy and momentum conservations. The net effect is that the corresponding damping (α_{SFS}) scales with T^2.

In the breathing Fermi surface (BFS)-associated relaxation process, the magnetization precession changes the energy of the free electron states via spin-orbit coupling. This serves to modulate the Fermi surface level at the precession frequency. There exists a slight lag in the re-population of the electrons to the modulated Fermi level, which causes a damping to the precession. At very low temperatures, as the electron life time (τ) is relatively long, the re-population of the electrons is slow and the lag is large, resulting in a large damping (α_{BFS}). With an increase in T, however, τ decreases as T^{-2} and α_{BFS} also decreases with T^{-2}.

Following the above discussions, one can express ΔH in the ECC perpendicular media as

$$\Delta H = \Delta H_{\mathrm{SFS}} + \Delta H_{\mathrm{BFS}} + \Delta H_{\mathrm{IBL}} \tag{7.3}$$

In the right side of Eq. (3), the first and second terms denote the contributions from the SFS and BFS relaxation processes, respectively, and can be written as

$$\Delta H_{\mathrm{SFS}} = \frac{2\alpha_{\mathrm{SFS}}}{|\gamma|} f = \frac{2}{|\gamma|}\left[\frac{C_{\mathrm{SFS}}}{|\gamma| M_s}\left(\frac{T}{300}\right)^2\right] f \tag{7.4}$$

$$\Delta H_{\mathrm{BFS}} = \frac{2\alpha_{\mathrm{BFS}}}{|\gamma|} f = \frac{2}{|\gamma|}\left[\frac{C_{\mathrm{BFS}}}{|\gamma| M_s}\left(\frac{300}{T}\right)^2\right] f \tag{7.5}$$

where T takes the unit of absolute temperature, and C_{SFS} and C_{BFS} are two constants with the same unit as the frequency. The last term in Eq. (3) is independent of f but varies with T as

$$\Delta H_{\mathrm{ILB}} = \left|\frac{\partial H_{\mathrm{FMR}}}{\partial H_{\mathrm{int}}}\right| \Delta H_{\mathrm{int}}(T) \tag{7.6}$$

where the first term on the right side equals to one according to Eqs. (7.1) and (7.2), and the second term denotes the range of the spatial variation of H_{int} at a given temperature. One can use Eqs. (7.3)-(7.6) to fit the experimental ΔH data to determine α_{SFS} and α_{BFS}. The fitting

discussed below, however, did not use Eq. (7.3), but used a convolution equation

$$\Delta H = \frac{\left(\Delta H_{\mathrm{SFS}} + \Delta H_{\mathrm{BFS}}\right)^2 + 1.97\left(\Delta H_{\mathrm{SFS}} + \Delta H_{\mathrm{BFS}}\right)\Delta H_{\mathrm{ILB}} + 2.16\Delta H_{\mathrm{ILB}}}{\left(\Delta H_{\mathrm{SFS}} + \Delta H_{\mathrm{BFS}}\right) + 2.16\Delta H_{\mathrm{ILB}}} \tag{7.7}$$

This equation was taken in consideration of the fact that ΔH_{ILB} constitutes a significant contribution in the presented ΔH data.

The line in Fig. 7.2(d) shows a fit of the $\Delta H(f)$ response with Eqs. (7.4)-(7.7). The fitting yielded $\alpha=(\alpha_{\mathrm{SFS}}+\alpha_{\mathrm{BFS}})=0.056\pm0.002$. The fitting also yielded $\Delta H_{\mathrm{ILB}}=1.35\pm0.04$ kOe, which is about $(18.2\%)\times H_{\mathrm{int}}$. In Fig. 7.3(c), the solid curve shows a fit of the $\Delta H(T)$ data, while the other three curves show the components of the fit. The fitting used the data in Fig. 7.1(b) and Fig. 7.3(d). The fitting yielded $C_{\mathrm{SFS}}=35$ MHz, $C_{\mathrm{BFS}}=102$ MHz, and $\Delta H_{\mathrm{ILB}}(T)=(27.5\%)\times H_{\mathrm{int}}(T)$. The corresponding damping constants at $T=300$ K are $\alpha_{\mathrm{SFS}}=0.018$, $\alpha_{\mathrm{BFS}}=0.052$, and $\alpha=0.07$. Since the fitting of the $\Delta H(T)$ data involves three fitting parameters, it cannot yield an accurate α value, but gives a α range. Fig. 7.5 presents four different fits which yielded different room-temperature α values, as indicated. One can see that the solid curves in graphs (a) and (d) cannot fit the data well, while the fits in graphs (b) and (c) are much better. The fits shown in Fig. 7.3(c) and Fig. 7.5, together with others not shown here, indicate a α range of 0.05-0.15.

One can conclude that the ECC perpendicular media have a damping constant of $\alpha\approx0.056$ based on the following considerations. (1) The value was determined from the FMR measurements over a relatively wide frequency range (27-50 GHz). (2) The linear fitting in Fig. 7.2(d) was very nice, with an error bar of 0.002 only. (3) The value falls into the α range determined by the T-dependent FMR study. Several points should be made regarding the

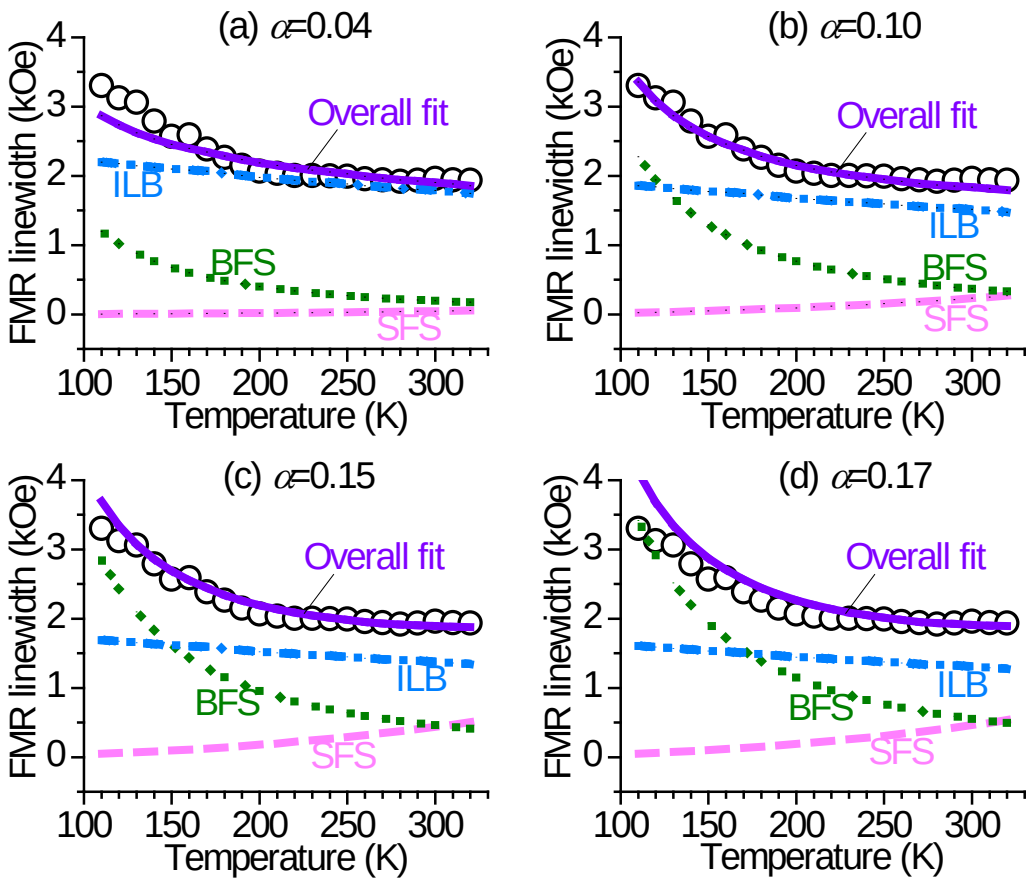

FIG. 7.5. Four different fits of the $\Delta H(T)$ data which yielded different α values, as indicated.

damping constant. First, the α values presented above are close to the α range reported in Mizukami's work. Note that in Mizukami's work the α values were determined with a completely different approach, the time-resolved magneto-optical Kerr effect technique. Second, the α values from this work are one order of magnitude larger than those reported in Mo's work and Krivosik's work. This significant difference is most likely due to the fact that the samples used in previous work were far different from real perpendicular media. Finally, the *T*-dependent FMR measurements in this work were carried out over a temperature range of

T=110-320 K, and it is believed that measurements over a much wider T range would allow for the determination of a much narrower α range. Future work in this aspect is of a great interest.

One can also conclude that the damping in ECC perpendicular media originates mainly from the BFS and SFS relaxation processes, with the BFS process slightly stronger than the SFS process at room temperature. Heat-assisted switching takes place at temperatures significantly higher than room temperature (650-750 K). At those temperatures, the SFS relaxation is expected to play a more significant role than the BFS process. Two important points should be emphasized. First, both the magnon-phonon scattering damping and the eddy current damping are Gilbert-like and contribute to the damping constant $\alpha \approx 0.056$. Their contributions, however, are expected to be significantly smaller than those from the BFS and SFS relaxation processes. Second, the presented α values do not have any contributions associated with sample inhomogeneity. The ILB contribution was identified and removed during the analysis, and the two-magnon scattering contribution was ruled out as the damping determination was based on the FMR measurements where the two-magnon scattering is essentially prohibited.

In summary, this letter reported a study on the damping properties in present ECC perpendicular media. The f-dependent FMR measurements indicate a damping constant of $\alpha \approx 0.056$. The T-dependent FMR measurements did not yield an accurate α value, but gave a α range which supported the f-dependent FMR-determined value. The numerical fitting of the FMR data indicate that the determined damping constant consists of contributions from the BFS and SFS relaxation processes, with the BFS process slightly stronger than the SFS process, and

includes no contributions associated with either two-magnon scattering or inhomogeneity line broadening.

Summary

The media damping is critical for media noise reduction, and is also extremely important for microwave assisted magnetization reversal (MAMR) which is one promising candidate for future high density magnetic recording. In the perspective of fundamental understanding, the Gilbert damping constant of ECC media is studied by both conventional FMR and VNA-FMR techniques. The results from different FMR techniques are consistent with each other. In practical term, people are looking for ways to manipulate the damping in perpendicular media, because there is an optimal value of damping constant to maximize the MAMR effect in media materials. Being able to tune the damping in media materials is an important step for MAMR implementation.

CHAPTER 8. OBSERVATION OF MICROWAVE-ASSISTED MAGNETIZATION REVERSAL IN PERPENDICULAR MEDIA

8.1 Overview

In the presence of microwaves, magnetization reversal in magnetic materials can be realized with relatively low external magnetic fields. This effect is called microwave-assisted magnetization reversal (MAMR). The underlying mechanism for the MAMR effect is shown in Fig. 8.1 and is explained as follows: the microwave magnetic fields excite large-angle magnetization precession; and the large-angle precession lowers the energy barrier for the rotation reversal in single-domain elements and that for domain nucleation or domain wall motion in multi-domain materials; so that the magnetization reversal can be achieved with relatively small switching field.

MAMR is one of the most promising approaches for future high-density magnetic recording. There have been considerable previous studies, both experimental and numerical, on MAMR effects in a wide variety of magnetic elements and materials. The MAMR effect was first observed by Thirion (2003). These authors demonstrated microwave-assisted switching in a 20-nm-diameter cobalt particle using superconducting quantum interference device techniques. Following the work by Thirion et al., the MAMR effect was observed in a number of different magnetic elements and materials. These include (1) single-domain elements, such as micron- and submicron-sized Permalloy film elements (Woltersdorf 2007, Nozaki 2009), Permalloy nano dots (Nembach 209), submicron cobalt particles (Nozaki 2007), and cobalt nanoparticles with a

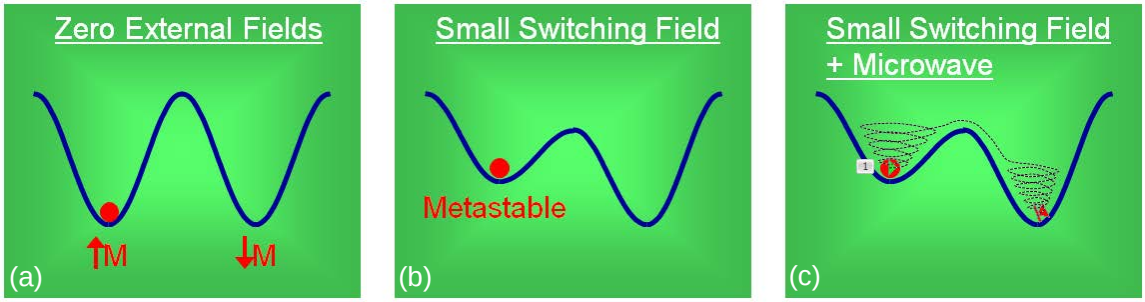

FIG. 8.1. Schematic of the mechanism of MAMR. Graph (a) indicates that there is a large energy barrier between the up and down magnetization states when no external magnetic field presents. Graph (b) shows that a small switching field can lower the energy barrier but not sufficient to switch the magnetization. Graph (c) shows that a small switching field can switch the magnetization through the assistance of a microwave magnetic field with its frequency close to the magnetization resonance frequency.

diameter of only 3 nm (Raufast 2008, Tamion 2010), and (2) multi-domain materials, such as cobalt strips (Grollier 2006), Permalloy wires (Nozaki 2007, Hayashi 2012), Permalloy and FeCo thin films (Nembach 2007, Pimentel 2007, Nistor 2009), Permalloy layers in magnetic tunnel junctions (Moriyama 2007, 2008), and Co/Pd multilayer structures (Yoshioka 2010, Okamoto 2010, 2012). The experiments on these materials all demonstrate that the presence of microwave magnetic fields can remarkably reduce the field required for magnetization reversal if the microwave frequency is close to the natural ferromagnetic resonance (FMR) frequency of the materials.

In addition to the experimental demonstrations summarized above, the numerical simulations of MAMR processes have also been carried out on the basis of the torque equation of

motion with a damping torque. These include the pioneering work by *Thirion et al*. and recent work by *Zhu et al*., etc. The simulation results all indicate that the presence of microwave fields can notably reduce the magnetization reversal field. In particular, simulations by Zhu et al. and Batra and Scholz demonstrate rather clearly the feasibility of microwave-assisted perpendicular recording.

In spite of those considerable works, however, work on MAMR operation on realistic perpendicular recording media is still rather limited. Perpendicular recording media generally consists of a magnetic granular layer and a magnetic capping thin layer and usually have a very large perpendicular anisotropy field, a high magnetization, and a large damping constant, as discussed in Chapter 7. The exchange coupling between the granular and capping layers also plays a critical role in the magnetization dynamics. Moreover, the size and properties of the grains in the granular layer can also fluctuate from grain to grain. Such fluctuations, for example, include variations in the strength of the uniaxial anisotropy field and in the direction of the anisotropy axis. As a result, the MAMR operation in perpendicular media films are expected to demand very large microwave magnetic fields and show responses significantly different from those observed in previous experiments.

The study in this chapter is carried out through close collaborations with industry partners in the fields of both media development and MAMR simulations and is also integrated with the media damping measurement efforts reported in Chapter 7. It is believed that this study could provide an in-depth understanding of the MAMR process in realistic perpendicular media and,

thereby, lay out a timely and solid groundwork for the development of a new MAMR technology for high-density perpendicular recording.

8.2 Experimental approaches

The goal of this section is to develop a micro loop device and use it to study MAMR effects in present perpendicular recording media. Specifically, a co-planar waveguide (CPW) type micro loop structure that can produce a microwave magnetic field of several hundreds of Oster in the 5-20 GHz frequency range has been designed and fabricated. The fabrication of the CPW structures was done by Dr. Axel Hoffmann's group at Argonne National Laboratory.

MAMR operation in perpendicular media involves three essentials as follows:

(1) High-power microwave pulses. The experimental study reported in Chapter 7 shows that the media materials have a large damping constant; and the large damping can result in a limit to the microwave-caused reduction in the switching field. Recent experiments also demonstrated that, for a certain material, one can push this limit in the field reduction by increasing the microwave power. In other words, high-power microwaves can generate high microwave magnetic fields which can induce a large angle precession in the material with very high uniaxial anisotropy field like current perpendicular media. As a result, "high power" is needed for the realization of MAMR in perpendicular media. There are three purposes for the use of "short microwave pulses", rather than continuous microwaves. First, one can eliminate microwave heating effects. Second, the use of pulses will allow us to study the effects of microwave duration on the MAMR process. Third, the magnetization reversal has to be

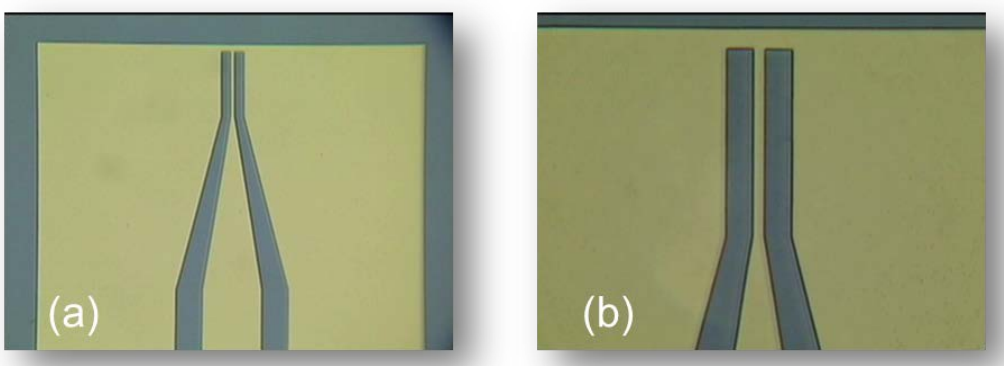

FIG. 8.2. Microscope images of the CPW type micro loop device. Graph (a) shows that the CPW signal-line width changes gradually from 100 μm to 5.5 μm. Graph (b) shows the details of the narrow part of the CPW signal-line which is 100 μm long and 5.5 μm wide.

realized within a short period of several nanoseconds in real hard disc drive devices.

(2) An appropriate structure for the delivery of microwaves to the media. The structure should be sufficiently fine or small so that it can produce a substantially strong alternating magnetic field to the media for a certain input microwave power level.

(3) A tool for the detection of switching status in the media. For (2), microwave co-planar waveguide (CPW) type micro loop devices are designed and fabricated for MAMR experiments. Figure 8.2 shows the schematic of one of such CPW devices. The device design is done with the help of software packages such as the Ansoft HFSS software, which is a full wave electromagnetic field simulator for arbitrary 3D volumetric passive devices. The CPW is defined using photolithography, followed by the thermal deposition of a thin metallic layer (gold) and a lift off procedure. The wide part of the signal line has a width of 100 μm, and the magnetic field produced by the wide signal line is relatively weak. Towards the very end of the

CPW, the signal line narrows down gradually. The narrowest part is 5.5 μm wide and 100 μm long, which can produce microwave magnetic fields as high as several hundreds of Oersted The MAMR experiments are performed with the perpendicular recording media placed on the top of the narrowest part of the CPW structure.

For (3), two approaches could be employed to determine the switching status in the media, (i) the FMR-absorption technique, which we developed recently, and (ii) the magnetic force microscopy (MFM). Experiments based on the FMR-absorption approach are relatively challenging. The media sample will be positioned on the top of the CPW device, with the media side down and the substrate side up. A static magnetic field is applied perpendicular to the film plane. The microwave magnetic field produced by the CPW signal line is to a large degree in the plane of the film. A pulse generator, a microwave source, and a microwave amplifier are used to provide microwave pulses to assist switching. A vector network analyzer (VNA) is used to measure the FMR response of the sample, as discussed in Chapter 4. The advantage of the above-described approach is that one can use one and the same CPW device to provide the microwave field for MAMR and determine the switching field. This approach, however, cannot be used for media samples that have very large damping and strong inhomogeneity. It is extremely hard to fabricate high-quality CPW structures with narrow signal lines.

The second approach is to switch the media sample with the CPW device first and then use the MFM system to determine the switching status in the media sample. This approach will not

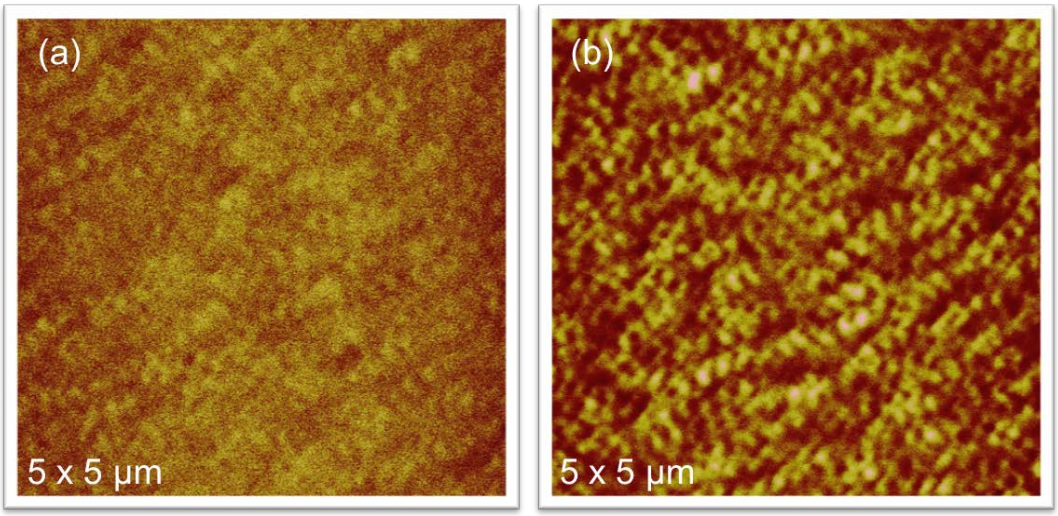

FIG. 8.3. Examples of MFM image. Graph (a) shows the MFM image of a fully saturated media sample. Graph (b) shows the MFM images of a partially saturated media sample.

only facilitate MAMR experiments on samples with very weak FMR signals, but also allow us to obtain detailed information on grain switching statistics. The following MAMR experiments are performed by this approach. Figure 8.3 shows a comparison of MFM surface images between a fully saturated media sample and a partially switched media sample. The fully saturated media sample is prepared by applying a 20 kOe external magnetic field. The partially saturated media sample is prepared by two steps: (1) apply a 20 kOe external magnetic field along one direction and (2) apply a 3.0 kOe external magnetic field in the opposite direction. The MFM image of the partially saturated media sample shows more contrast than that of the fully saturated media sample.

Figure 8.4 illustrates the experimental approach. Graph (a) shows a schematic of the experimental configuration. Graphs (b) and (c) show a photograph and an atomic force

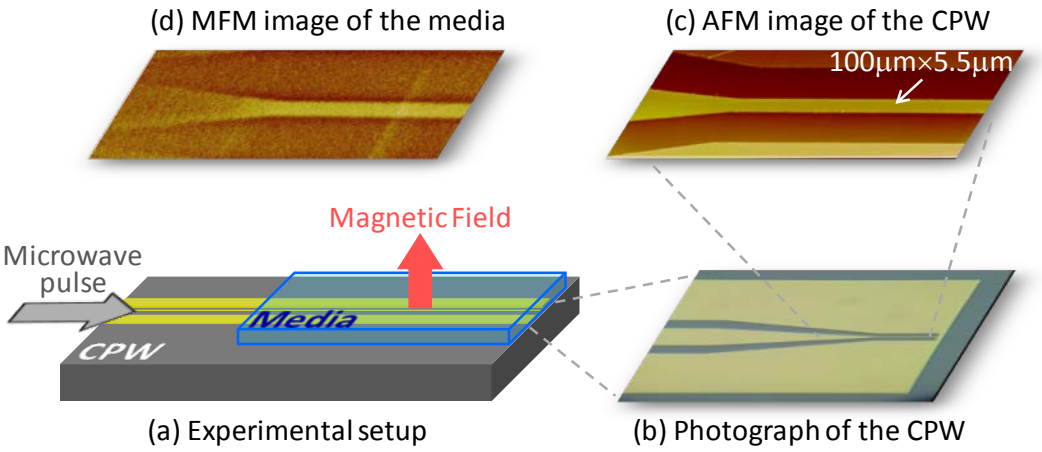

FIG. 8.4. (a) Experimental configuration. (b) A photograph of the portion of the coplanar waveguide (CPW) where the signal line is narrow. (c) An AFM image of the CPW signal line. (d) An MFM image of the media sample which shows the MAMR effect.

microscopy (AFM) image, respectively, of the portion of the CPW structure where the signal line is a 5.5 μm-wide, 100 μm-long narrow strip. Graph (d) gives a representative MFM image which shows an MAMR-caused bright strip.

The MAMR experiments consist of the following four steps. (1) Saturate the media sample with a strong perpendicular magnetic field (20 kOe). (2) Apply a switching field of 3.0 *kOe* which is opposite to the magnetization in the media and is close to the nucleation field (lower than the coercivity field). (3) Apply microwave pulses to the CPW to assist the switching of the grains in the media. (4) Use the MFM system to determine the switching status of the grains in the media. When the microwave pulses are applied, the narrow portion of the CPW signal line (see Fig. 8.4 (c)) produces relatively strong microwave magnetic fields. These microwave fields lower the energy barrier for magnetization reversal in the grains right beneath the signal

line and thereby induce the switching of these grains. Such switching manifests itself as a bright strip in the MFM image, as shown in Fig. 8.4 (d).

8.3 Microwave assisted magnetization reversal in exchange coupled composite media

Numerical simulations have demonstrated the feasibility of MAMR operation in perpendicular recording media. Experimental demonstrations, however, are rather challenging, as the media typically require relatively large switching fields and have significantly large damping in comparison with the above-mentioned magnetic elements. Nevertheless, very recently two groups reported the studies of MAMR in perpendicular media. Boone et al. used the anomalous Hall effect (AHE) to measure the hysteresis loop of a perpendicular media bar and studied the effects of microwaves on the AHE loop. They observed a microwave-caused reduction in the coercivity field of up to 8%. *Nozaki et al*. demonstrated that the exposure of a perpendicular media sample to microwaves could produce a notable shift in the sample's ferromagnetic resonance (FMR) field, which indicated the microwave-assisted switching of certain grains in the sample. These two studies indicated the feasibility of MAMR in perpendicular media.

This section reports on the observation of MAMR responses in a sample cut from an "exchange coupled composite" (ECC) perpendicular media disk. The microwave fields were applied by placing a coplanar waveguide (CPW) structure on the media sample and feeding it with narrow microwave pulses. The switching states of the grains in the media were measured by magnetic force microscopy (MFM) techniques. For the microwaves with a frequency close

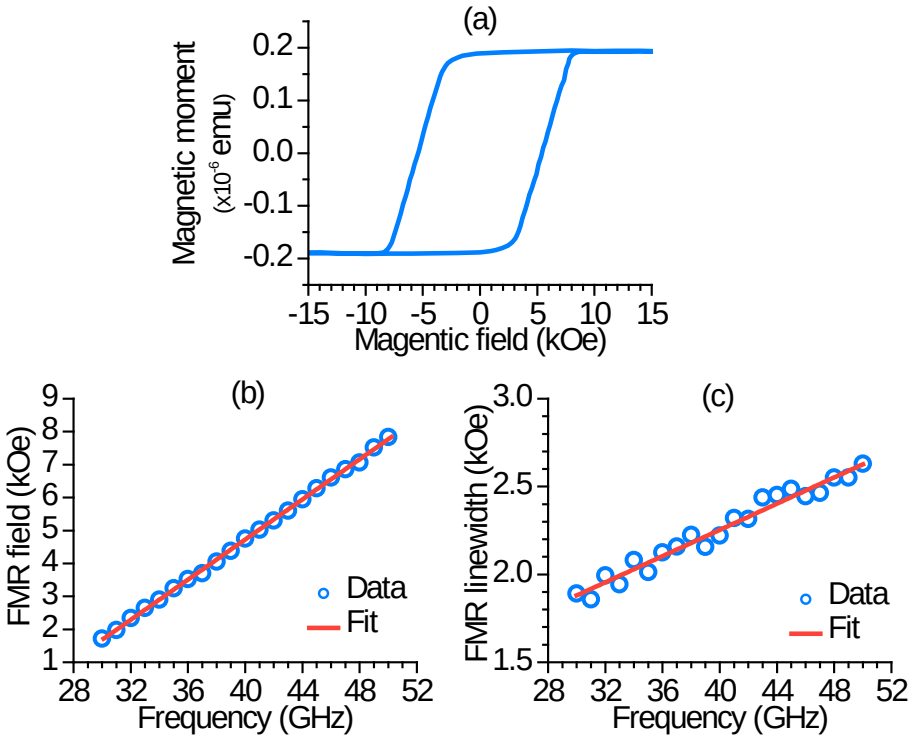

FIG. 8.5. Properties of the ECC media sample. (a) A hysteresis loop. (b) Ferromagnetic resonance (FMR) field vs. frequency. (c) FMR linewidth vs. frequency.

to the FMR frequency of the media, the microwave-assisted switching was observed when the microwave power was higher than a certain threshold level. For the microwaves with a certain high power level, the MAMR was observed for a relatively wide microwave frequency range which covers the FMR frequency and is centered at a frequency below the FMR frequency. The effects of the microwave pulse duration and repetition rate were also examined. The results indicated that the observed MAMR response was not attributed to heating effects.

The sample was a 4 mm by 4 mm rectangle element cut from an ECC media disk. The core components of the ECC media include a 4.5-nm-thick "soft" magnetic layer, an 8.5-nm-thick "hard" magnetic layer, and a 0.8-nm-thick weakly magnetic exchange-break layer

in-between the "soft" and "hard" layers. Both of the two magnetic layers are CoPtCr-based granular films.

Figure 8.5 shows the static and FMR properties of the sample. Graph (a) presents a hysteresis loop measured by SQUID techniques. The measurement was carried out with a magnetic field normal to the sample plane. The data indicate a saturation induction of about 9.2 kG, a nucleation field in the 2-3 kOe range, and a coercivity field of about 5.4 kOe. Graphs (b) and (c) present the FMR data measured by broadband vector network analyzer techniques. Graph (b) shows the FMR field as a function of frequency. The circles show the data, while the line shows a fit with the Kittel equation. One can see that the fitting is almost perfect. The fitting yielded an effective perpendicular anisotropy field of about 16.6 kOe and an absolute gyromagnetic ratio of about 3.28 GHz/kOe. The gyromagnetic ratio here is higher than the standard value (2.8 GHz/kOe). Similar ratios were also reported for CoCrPt alloy films and CoCr granular films. Graph (c) presents the half-power FMR linewidth as a function of the frequency. The circles show the data, while the line shows a linear fit. The fitting yielded an effective Gilbert damping parameter of 0.061±0.003 and an inhomogeneity line broadening contribution of 761±64 Oe. The damping parameter is close to the value reported for CoPtCr alloy films (0.06). The inhomogeneity line broadening is relatively large and is mainly attributed to the variation of the internal effective field on individual grains. The effective field consists of the anisotropy field, the dipole interaction field, the grain self-demagnetization field, and intergranular exchange field.

The MAMR experiments are performed following the experimental approaches introduced in the previous subsection. The pulsed microwave sent to the CPW has frequency of 13 GHz, power of 31 dBm, pulse repetition rate of 100 kHz, and pulse duration of 90 ns. The applied switching field is 3.0 kOe. The MAMR induced switching manifest themselves as bright strips in the MFM images shown in Fig. 8.6. Three facts should be pointed out. First, the bright strip in the MFM image has the same length and width as the narrow signal line of the CPW, as indicated in Fig. 8.6 (a). Second, towards the left end of the bright strip, one sees a gradual increase in the strip width and a gradual decrease in the strip contrast, as shown in Fig. 8.6 (b). This agrees with the expectations that the wider the signal line is, the weaker the microwave field is and the fewer grains are switched. Third, the MFM image shows a completely opposite contrast if one saturates the media along an opposite direction. These facts together clearly demonstrate the validity of the above-described MAMR measurement approaches. Although not shown in figure 8.6, the atomic force microscopy (AFM) images show that the media samples have clear surfaces after MAMR experiment, no microwave heating induced damages. To conclude that the magnetization switching are induced by MAMR effect, but not microwave heating effect, the MAMR experiments are checked with different microwave powers, different microwave frequencies, different pulse repetition rates and different pulsed durations.

The MFM image in Fig. 8.7 is taken from a 100 μm by 100 μm square area of the sample where six separate MAMR experiments are conducted at six different locations.

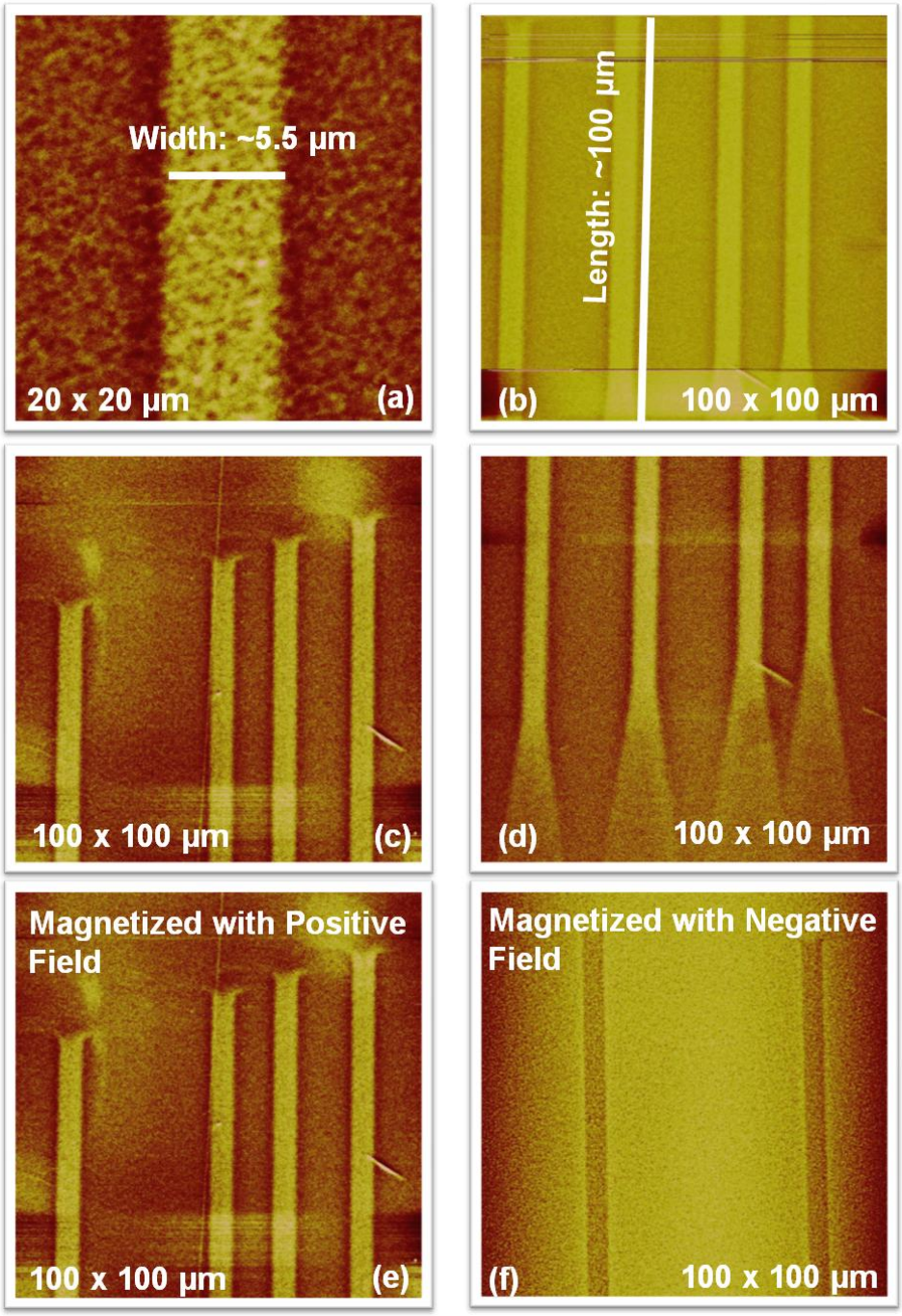

FIG. 8.6. (a) and (b) Dimension of the MAMR induced bright strip. (c) and (d) The MAMR induced bright strips have the same shape as the CPW signal-line. (e) and (f) The MAMR induced strips change from bright to dark as the magnetization are magnetized in the opposite direction.

The microwave power P_{mw} used for each MAMR experiment is indicated at the corresponding location. For all the experiments, the carrier frequency f_{mw} of the microwave pulse is kept the same, at 13 GHz. For the MFM images in Fig. 8.8, in contrast, the MAMR experiments at different locations are carried out at the same microwave power, which is 31 dBm, but different microwave frequencies, as indicated. Except for P_{mw} and f_{mw}, the other parameters were the same for all the experiments. The field used to saturate the sample is 20 kOe. The switching field H_{sw} is 3 kOe. The microwave pulses had a width of 11 ns and a repetition rate of 0.1 kHz. Note that the power levels cited above are nominal power applied to

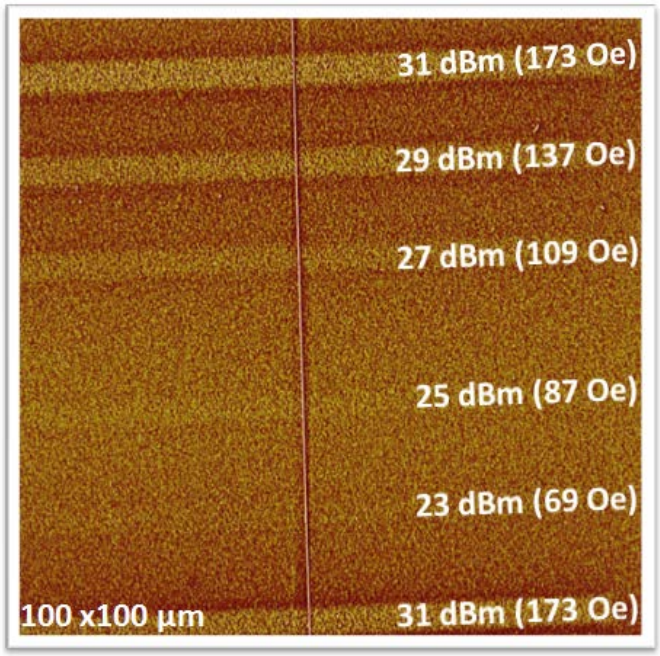

FIG. 8.7. An MFM image of the area of a media sample where six separate MAMR experiments were carried out at six different locations. The microwave power level used in each experiment is indicated at the corresponding location.

the CPW. The field values given in Fig. 8.7 and below are microwave magnetic fields from the narrow CPW signal-line, which were estimated based on the input microwave power, the reflection coefficient of the CPW, and the width of the CPW signal-line. The dashed lines in Fig. 8.8 indicate the positions of the CPW signal line.

The MFM image in Fig. 8.7 shows strips with rather low contrasts for P_{mw}=23 dBm and 25

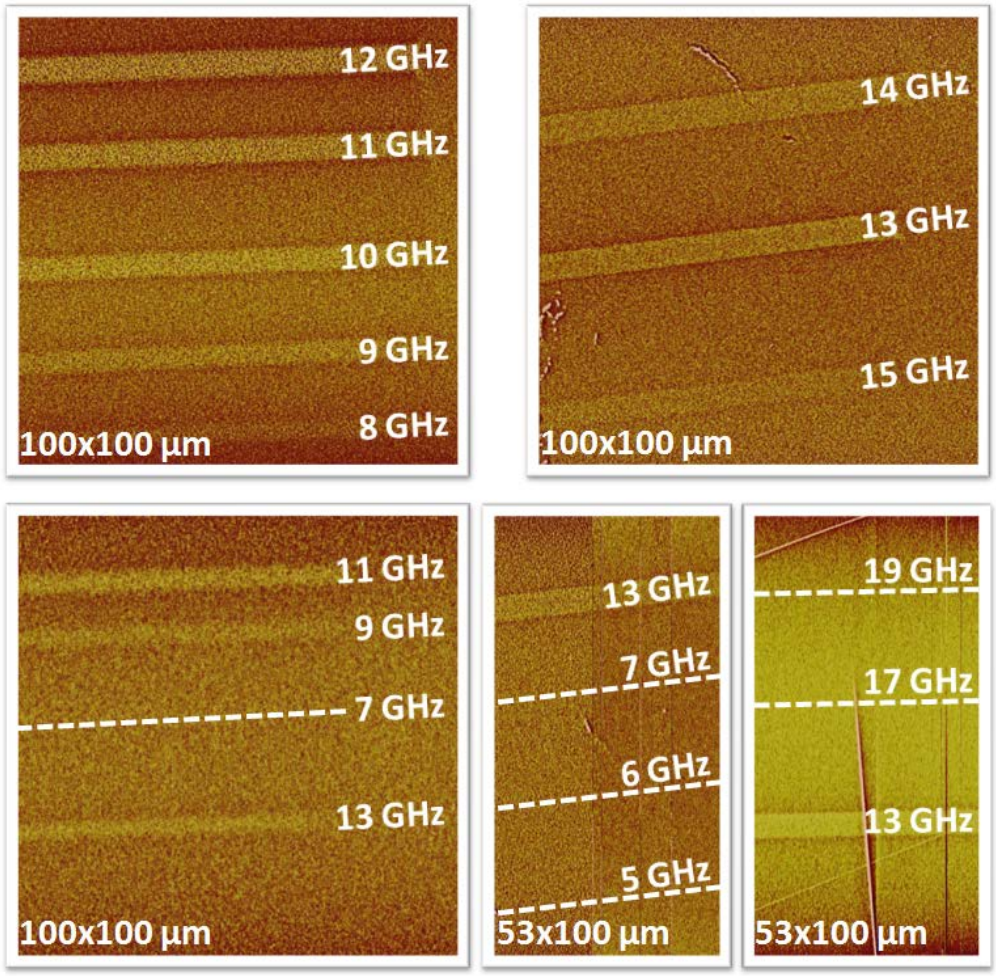

FIG. 8.8. MFM images for the areas of a sample where separate MAMR experiments were carried out at different locations. The experiments were done with microwave pulses of different carrier frequencies, as indicated.

dBm and strips with high contrasts for $P_{mw} \geq 27$ dBm. This indicates a power threshold of about 27 dBm (109 Oe) for MAMR operation with microwave pulses of f_{mw}=13 GHz. The MFM images in Fig. 8.8 show high- contrast strips for f_{mw} =8 GHz, 9 GHz, 10 GHz, 11 GHz, 12 GHz, 13 GHz, 14 GHz, and 15 GHz but show no strips for f_{mw} =5 GHz, 6 GHz, 7 GHz, 17 GHz, and 19 GHz. This indicates that, when P_{mw} =31 dBm, the MAMR occurs over a frequency range of 8-15 GHz. Note that for the given H_{sw} the FMR frequency of the media was estimated to be 14.4 GHz, which is within the 8-15 GHz frequency range.

These results clearly demonstrate the MAMR operation in the media. Moreover, they show that, for certain high microwave power, the MAMR operation can take place over a relatively broad frequency range which covers the FMR frequency but is centered below the FMR frequency. This agrees with previous experimental observations. The reason for such a broad frequency range is that the media have a rather broad FMR linewidth as shown in Fig. 8.5 (c), and the microwaves can excite magnetization precession over a broad frequency range as long as the microwave field is sufficient strong. It is expected that this frequency range increases with an increase in the microwave power. The fact that the frequency range is centered below the FMR frequency is mainly because the effective anisotropy field takes lower values during the switching process, and the precession frequency decreases linearly with the anisotropy field according to the Kittel equation.

Figure 8.9 presents representative MFM images that show the effects of the microwave pulse repetition rate and duration. The left image shows four strips resulted from MAMR with

microwave pulses of the same duration (98 ns) but significantly different repetition rates, as indicated. The right images shows two strips resulted from MAMR with microwave pulses of the same repetition rate (0.1 kHz) but significantly different durations, as indicated. The field used to saturate the sample and the switching field are the same as cited above.

The microwave pulses had f_{mw}=13 GHz and P_{mw}=31 dBm. The strips in each image show almost the same contrast. This demonstrates that the effects of the microwave pulse repetition rate and duration are rather insignificant. This result indicates that the above-presented MAMR responses were not attributed to a heating effect.

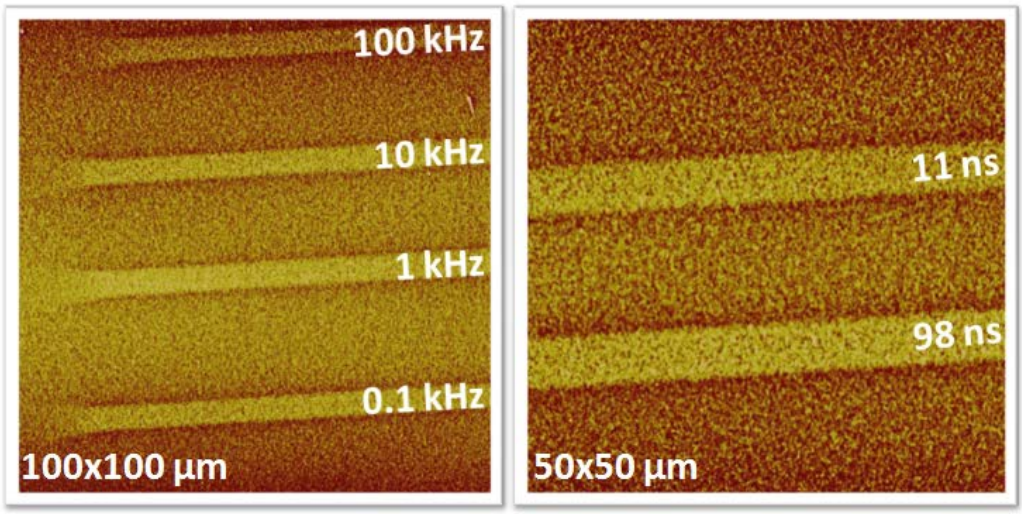

FIG. 8.9. MFM images for the areas of a sample where separate MAMR experiments were carried out at different locations. Left: the experiments were done with microwave pulses of different repetition rates, as indicated. Right: the experiments were done with microwave pulses of different durations, as indicated.

8.4 Summary

In summary, this subsection reports microwave-assisted magnetization reversal (MAMR) in a 700-Gbit/in2 perpendicular media sample. The microwave fields were applied by placing a coplanar waveguide on the media sample and feeding it with narrow microwave pulses. The switching states of the media grains were measured by magnetic force microscopy. For microwaves with a frequency close to the ferromagnetic resonance (FMR) frequency of the media, MAMR was observed for microwave power higher than a certain threshold. For microwaves with certain high power, MAMR was observed for a broad microwave frequency range which covers the FMR frequency and is centered below the FMR frequency.

CHAPTER 9. SUMMARY AND OUTLOOK

Experimental investigations and numerical analyses have been carried out on the magnetization relaxations in magnetic thin films used in present perpendicular magnetic recording technology. The samples studied include the free layers of modern tunnel magneto-resistance (TMR) readers, FeCo alloy films for future writers, and exchange-coupled composite (ECC) perpendicular media. The studies allowed for the understanding of the damping properties in the magnetic recording materials and the demonstration of practical methods for tuning the damping. Moreover, microwave-assisted magnetization reversal has been demonstrated in perpendicular media samples cut from a commercial quality 700-Gbit/in^2 media disk. This study is useful for the development of advanced magnetic recording techniques for future magnetic recording with an area density beyond 1Tbit/in^2.

9.1. Summary

The working equations for ferromagnetic resonance, phenomenological Gilbert damping, and two-magnon scattering contributed damping have been derived. The use of the working equations to solve practical problems has been presented as well. The experimental and numerical studies on the damping properties in the free layer of modern TMR readers have been carried out. The studies indicate that the free layer shows a Gilbert damping constant of 8.13×10^{-3}. When the free layer is magnetized with a field which is not normal to the film plane, two-magnon scattering also occurs. This scattering process, however, makes a contribution to the relaxation much smaller than the Gilbert contribution, which is about 2.5 times smaller than

the Gilbert component for the in-plane field configuration. The TMS process has also been observed in 100-nm-thick $Fe_{65}Co_{35}$ films, which made a much more significant contribution to the relaxation than the Gilbert damping. Furthermore, it is found that the use of different types of seed layers results in films with different relaxation rates, both in magnitude and frequency dependence, but similar static magnetic properties. The changes in damping can be interpreted in terms of the effects of the seed layers on the film grain properties and the correlation between the grain properties and the grain-to-grain TMS and grain-boundary TMS processes.

Damping characterization in perpendicular magnetic recording media is a long-standing problem since the damping and inhomogeneity are believed to be extraordinarily large. An ultra-sensitive broadband ferromagnetic resonance (FMR) spectrometer based on the vector network analyzer (VNA) technique is developed to resolve the media damping issue. With the newly developed VNA-FMR technique, the damping constant of present ECC perpendicular media is found to be about 0.056. This damping value is confirmed by separate measurements with conventional FMR technique. In addition, the numerical fitting of the temperature-dependent FMR data indicate that the determined damping constant consists of contributions from the breathing Fermi surface (BFS) and spin-flip scattering (SFS) relaxation processes, with the BFS process slightly stronger than the SFS process at room temperature, and includes no contributions associated with either two-magnon scattering or inhomogeneity line broadening. The MAMR effect is a very promising mechanism for the realization of next-generation magnetic recording at several terabits per square inch. MAMR operation in a

700-Gbit/in^2 perpendicular media sample has been demonstrated. For microwaves with frequencies close to the FMR frequency of the media, the MAMR operation was observed for microwave power higher than a certain threshold level. For microwaves with certain high power, the MAMR effects were observed for a broad microwave frequency range which covered the FMR frequency and was centered below the FMR frequency. It has also been demonstrated that the MAMR operation was independent of both the microwave pulse duration and repetition rate.

9.2. Outlook

This thesis provides a start for the study of the ferromagnetic resonance and damping properties of magnetic thin films used in present perpendicular magnetic recording. Topics that are relevant to the studies in this thesis and are of great interest for future study include, but are not limited to, the following:

(1) Ferromagnetic resonance and damping properties in patterned structures.

(2) Correlation between damping properties and electrical performances at device levels.

(3) Intergranular exchange coupling in perpendicular recording media

(4) Tuning of damping of perpendicular media via doping.

(5) Effects of ECC perpendicular media damping on MAMR.

(6) MAMR of bit patterned media.

REFERENCE

1. A. B. Kos, T. J. Silva, and P. Kabos, Rev. Sci. Instr 73, 3563 (2002).
2. A. Brataas, Y. Tserkovnyak, and G. E. W. Bauer, *Phys. Rev. Lett*. **101**, 03207 (2008).
3. A. G. Gurevich, and G. A. Melkov, *Magnetic Oscillations and Waves*, (CRC Press, 1996).
4. A. M. Stoneharm, *J. Phys. D* **5**, 670 (1972).
5. A. Tamion, C. Raufast, E. B. Orozco, V. Dupuis, T. Fournier, T. Crozes, E. Bernstein, and W. Wernsdorfer, *J. Magn. Magn. Mater*. **322**, 1315 (2010).
6. A. Widom, C. Vittoria, and S. D. Yoon, *J. Appl. Phys.* **108**, 073924 (2010).
7. B. Heinrich and J. A. C. Bland, *Ultrathin Magnetic Structures: Fundamentals of Nanomagnetism* (Springer, Berlin, 2005).
8. B. Heinrich, R. Urban, and G. Woltersdorf, J. Appl. Phys. **91**, 7523 (2002).
9. B. K. Kuanr, R. E. Camley, and Z. Celinski, *J. Appl. Phys*. **75**, 6610 (2004).
10. B. Kuanr, R. Camley, and Z. Celinski, *J. Appl. Phys*. **95**, 6610 (2004).
11. B. Lax, and K. J. Button, *Microwave Ferrites and Ferrimagnetics*, (McGraw-Hill, 1962).
12. C. E. Patton, "A Review of Microwave Relaxation in Polycrystalline Ferrite", Intermag conference, Japan, 433 (1972).
13. C. E. Patton, "Microwave Resonance and Relaxaton", Chapter 10, *Magnetic oxides*, (John Wilery, London, 1975).
14. C. E. Patton, AIP conference proceeding, **10**, 135 Devner (1972) (1973).
15. C. E. Patton, and H. J. Van Hook, J. Appl. Phys. **43**, 2872 (1972).

16. C. E. Patton, C. H. Wilts, and F. B. Humphrey, J. Appl. Phys. **38**, 1358 (1967).

17. C. E. Patton, Czech. J. Phys. B **21**, 490 (1971).

18. C. E. Patton, Czech. J. Phys. B **26**, 925 (1976).

19. C. E. Patton, J. Appl. Phys. **41**, 1355 (1970).

20. C. E. Patton, T. C. McGill, and C. H. Wilts, J. Appl. Phys. **37**, 3594 (1966).

21. C. Kittel, Phys. Rev., **73**, 155 (1948).

22. C. Nistor, K. Sun, Z. Wang, M. Wu, C. Mathieu, and M. Hadley, *Appl. Phys. Lett*. **95,** 012504 (2009).

23. C. Raufast, A. Tamion, E. Bernstein, V. Dupuis, Th. Tournier, Th. Crozes, E. Bonet, and W. Wernsdorfer, *IEEE Trans. Mag*n. **44**, 2812 (2008).

24. C. Scheck, L, Cheng, and W. E. Bailey, *Appl. Phys. Lett*. **88**, 252510 (2006).

25. C. Scheck, L. Cheng, and W. E. Bailey, *Appl. Phys. Lett*. **88**, 252510 (2006).

26. C. T. Boone, J. A. Katine, E. E. Marinero, S. Pisana, and B. D. Terris, *IEEE Magn. Lett*. **3**, 3500104 (2012).

27. C. T. Boone, J. A. Katine, E. E. Marinero, S. Pisana, and B. D. Terris, *J. Appl. Phys.* **111**, 07B907 (2012).

28. C. Thirion, W. Wernsdorfer, and D. Mailly, *Nat. Mater*. **2**, 524 (2003).

29. D. D. Stancil, *Theory of Magnetostatic Wvaes*, (Springer-Verlag, 1993).

30. D. L. Mills, *Phys. Rev. B* **68**, 014419 (2003).

31. E. Schlömann, IEEE, Trans. Mag. **1**, 75 (1970).

32. E. Schlömann, J. Phys. Chem. Solids, **6**, 257 (1958).

33. E. Schlömann, Phys. Rev. **182**, 632 (1969).

34. G. Woltersdorf and C. H. Back, *Phys. Rev. Lett*. **99**, 227207 (2007).

35. G. Woltersdorf, and B. Heinrich, Phys. Rev. B **69**, 184417 (2004).

36. G. Woltersdorf, M. Buess, B. Heinrich, and C. H. Back, *Phys. Rev. Lett*. **95**, 037401 (2005).

37. G. Woltersdorf, M. Kiessling, G. Meyer, J.-U. Thiele, and C. H. Back, *Phys. Rev. Lett*. **102**, 257602 (2009).

38. H. Lee, L. Wen, M. Pathak, P. Janssen, P. LeClair, C. Alexander, C. K. A. Mewes, and T. Mewes, *J. Phys. D: Appl. Phys.* 41, 215001 (2008).

39. H. Lee, Y. A. Wang, C. K. A. Mewes, W. H. Butler, T. Mewes, S. Maat, B. York, M. J. Carey, and J. R. Childress, *Appl. Phys. Lett*. **95**, 082502 (2009).

40. H. T. Nembach, H. Bauer, J. M. Shaw, M. Schneider, and T. J. Silva, EC-11, the 2009 IEEE International Magnetics Conference, Sacramento, California, May 4-8, 2009.

41. H. T. Nembach, P. M. Pimentel, S. J. Hermsdoerfer, B. Hillebrands, and S. O. Demokritov, *Appl. Phys. Lett*. **90**, 062503 (2007).

42. H. T. Nembach, T. J. Silva, J. M. Shaw, M. L. Schneider, M. J. Carey, S. Maat, and J. R. Childress, *Phys. Rev. B* **84**, 054424 (2011).

43. J. D. Jackson, *Classical Electrodynamics*, (John Wiley & Sons, 1998).

44. J. Dubowik, K. Zaleski, and H. Glowinski, *Phys. Rev. B* **84**, 1844385 (2011).

45. J. G. Zhu and D. Z. Bai, *J. Appl. Phys*. **93**, 6447 (2003).

46. J. G. Zhu, X. Zhu, and Y. Tang, *IEEE Trans. Magn*. **44**, 125 (2008).

47. J. Grollier, M. V. Costache, C. H. van der Wal, and B. J. van Wees, *J. Appl. Phys*. **100**, 024316 (2006).

48. J. Kuneš and V. Kamberský, *Phys. Rev. B* **65**, 212411 (2002).

49. J. Lindner, I. Barsukov, C. Raeder, C. Hassel, O. Posth, R. Meckenstock, P. Landeros, and D. L. Mills, *Phys. Rev B* **80**, 224421 (2009).

50. J. Lindner, K. Lenz, E. Kosubek, K. Baberschke, D. Spoddig, R. Meckenstock, J. Pelzl, Z. Frait, and D. L. Mills, *Phys. Rev. B* **68**, 060102 (R) (2003).

51. J. Lou, R. E. Insignares, Z. Cai, K. S. Ziemer, M. Liu, and N. X. Sun, *Appl. Phys. Lett*. **91**, 182504 (2007).

52. J. M. Beaujour. D. Ravelosona, I. Tudosa, E. E. Fullerton, and A. D. Kent, *Phys. Rev. B* **80**, 180415(R) (2009).

53. J. O. Rantschler, C. Alexander, Jr., and H.-S. Jung, *J. Magn. Magn. Mater.* **286**, 262 (2005).

54. K. D. Mckinstry, Ph. D. Thesis, Colorado State University, 1991.

55. K. Gilmore, Y. U. Idzerda, and M. D. Stiles, *Phys. Rev. Lett.* **99**, 027204 (2007).

56. K. Lenz, H. Wende, W. Kuch, K. Baberschke, K. Nagy, and A. Jánossy, *Phys. Rev. B* **73**, 144424 (2006).

57. K. Satoshi, A. Yasuo, M. Terunobu, and M. Shigemi, Jpn. *J. Appl. Phys.*, Part 1 **45**, 3892 (2006).

58. K. Zakeri, J. Lindner, I. Barsukov, R. Meckenstock, M. Farle, U. von Horsten, H. Wende, W. Keune, J. Rocker, S. S. Kalarickal, K. Lenz, W. Kuch, K. Baberschke, and Z. Frait, *Phys. Rev. B* **76**, 104416 (2007).

59. L. D. Landau, and E. M. Lifshitz, Physik. Z. Sowjetuniou, **8**, 153 (1935).

60. L. Lu, J. Young, M. Wu, C. Mathieu, M. Hadley, P. Krivosik, and N. Mo, *Appl. Phys. Lett*. **100**, 022403 (2012).

61. L. Lu, M. W, M. Mallary, G. Bertero, K. Srinivasan, R. Acharya, H. Schultheiss, A. Hoffman, *Appl. Phys. Lett*. **103**, 042413 (2013).

62. M. Hayashi, Y. K. Takahashi, and S. Mitani, *Appl. Phys. Lett*. **101**, 172406 (2012).

63. M. J. Hurben, and C. E. Patton, *J. Appl. Phys*. **83**, 4344 (1998).

64. M. J. Hurben, D. R. Franklin, and C. E. Patton, *J. Appl. Phys*. **81**, 8979 (1997).

65. M. J. Hurben, Ph. D. Thesis, Colorado State University, 1996.

66. M. L. Schneider, J. M. Shaw, A. B. Kos, T. Cerrits, and T. J. Silva, *J. Appl. Phys*. **102**, 103909 (2007).

67. M. Oogane, T. Kubota, Y. Kota, S. Mizukami, H. Naganuma, A. Sakuma, and Y. Ando, *Appl. Phys. Lett.* **96**, 252501 (2010).

68. M. Sparks, *Ferromagnetic-relaxation Theory* (McGraw-Hill, 1964).

69. M. Sparks, R. Loudon, and C. Kittel, Phys. Rev., **122,** 791 (1961).

70. N. Bloembergen, Proc. ire, 44, 1259 (1956).

71. N. Inaba, Y. Uesaka, A. Nakamura, M. Futamoto, and Y. Sugita, *IEEE Trans. Magn*. **33**, 2989 (1997).

72. N. Mo, J. Hohlfeld, M. ul Islam, C. S. Brown, E. Girt, P. Krivosik, W. Tong, A. Rebei, and C. E. Patton, *Appl. Phys. Lett*. **92**, 022506 (2008).

73. N. Smith, *J. Magn. Magn. Mater*. **321**, 531 (2009).

74. O. Ertl, G. Hrkac, D. Suess, M. Kirschner, F. Dorfbauer, J. Fidler, and T. Schrefl, *J. Appl. Phys.* **99**, 08S303 (2006).

75. O. Heinonen and K. Gao, *J. Magn. Magn. Mater*. **320**, 2885 (2008).

76. P. Kabos, M. Mendik, G. Wiese, and C. E. Patton, Phys. Rev. B **55**, 11457 (1997).

77. P. Krivosik, N. Mo, S. Kalarickal, and C. E. Patton, *J. Appl. Phys.* **101**, 083901 (2007).

78. P. Krivosik, S. S. Kalarickal, N. Mo, S. Wu, and C. E. Patton, *Appl. Phys. Lett*. **95**, 052509 (2009).

79. P. Landeros, R. E. Arias, and D. L. Mills, *Phys. Rev. B* **77**, 214405 (2008).

80. P. M. Pimentel, B. Leven, B. Hillebrands, and H. Grimm, *J. Appl. Phys*. **102**, 063913 (2007).

81. Q. H. F. Vrehen, J. Appl. Phys. **40**, 1849 (1969).

82. R. A. Waldron, *Theory of Guided Electromagnetic Waves*, (Van Nostrand Reinhold Company, 1969).

83. R. C. O'Handley, *Modern Magnetic Materials: Principles and Application*, (Wiley, New York, 2000).

84. R. D. McMichael and D. j. Twisselmann, *Phys. Rev. Lett*. **90**, 227601 (2003).

85. R. D. McMichael and P. Krivosik, *IEEE Trans. Magn.* **40**, 2 (2004).

86. R. D. McMichael, M. D. Stiles, P. J. Chen, and W. F. Egelhoff, *J. Appl. Phys*. **83**, 7037 (1998).

87. R. E. Camley, Z. Celinski, T. Fal, A. V. Glushchenko, A. J. Hutchison, Y. Khivintsev, B. Kuanr, I. R. Harward, V. Veerakumar, and V. V. Zagorodnii, *J. Magn. Magn. Mater*. **321**, 2048 (2009).

88. R. Urban, B. Heinrich, G. Woltersdorf, J. Ajdari, K. Myrtle, J. F. Cochran, and E. Rozenberg, *Phys. Rev. B* **65**, 020402 (2001).

89. S. Hinata, S. Saito, and M. Takahashi, *J. Appl. Phys.* **111**, 07B722 (2012).

90. S. Mizukami, D. Watanabe, T. Kubota, X. Zhang, H. Naganuma, M. Oogane, Y. Ando, and T. Miyazaki, *Appl. Phys. Express* **3**, 123001 (2010).

91. S. Mizukami, E. P. Sajitha, D. Watanabe, F. Wu, T. Miyazaki, H. Naganuma, M. Oogane, and Y. Ando,

Appl. Phys. Lett. **96**, 152502 (2010).

92. S. Mizukami, H. Abe, D. Watanabe, M. Oogane, Y. Ando, and T. Miyazaki, *Appl. Phys. Express* **1**, 121301 (2008).
93. S. Okamoto, N. Kikuchi, M. Furuta, O. Kitakami, and T. Shimatsu, *Appl. Phys. Express* **5**, 093005 (2012).
94. S. Okamoto, N. Kikuchi, O. Kitakami, T. Shimatsu, and H. Aoi, *J. Appl. Phys*. **109**, 07B748 (2011).
95. S. S. Kalarickal, N. Mo, P. Krivosik, and C. E. Patton, *Phys. Rev. B* **79**, 094427 (2009).
96. S. S. Kalarickal, P. Krivosik, J. Das, K. S. Kim, and C. E. Patton, *Phys. Rev. B* **77**, 054427 (2008).
97. S. S. Kalarickal, P. Krivosik, M. Wu, and C. E. Patton, *J. Appl. Phys.* **99**, 093909 (2006).
98. S. Schäfer, N. Pachauri, C. K. A. Mewes, T. Mewes, C. Kaiser, Q. Leng, and M. Pakala, *Appl. Phys. Lett*. **100**, 032402 (2012).
99. T. J. Silva, C. S. Lee, T. M. Crawford, and C. T. Rogers, *J. Appl. Phys.* **85**, 7849 (1999).
100. T. L. Gilbert, *IEEE Trans. Magn*. **40**, 3443 (2004).
101. T. Moriyama, R. Cao, J. Q. Xiao, J. Lu, X. R. Wang, Q. Wen, and H. W. Zhang, *Appl. Phys. Lett.* **90**, 152503 (2007).
102. T. Moriyama, R. Cao, J. Q. Xiao, J. Lu, X. R. Wang, Q. Wen, and H. W. Zhang, *J. Appl. Phys.* **103**, 07A906 (2008).
103. T. Yoshioka, T. Nozaki, T. Seki, M. Shiraishi, T. Shinjo, Y. Suzuki, and Y. Uehara1, *Appl. Phys. Express* **3**, 013002 (2010).
104. W. Scholz and S. Batra, *J. Appl. Phys*. **103**, 07F539 (2008).

105. X. Liu, W. Zhang, M. J. Carter, and G. Xiao, *J. Appl. Phys*. **110**, 033910 (2011).

106. Y. Ding, T. J. Klemmer, and T. M. Crawford, *J. Appl. Phys.* **96**, 2969 (2004).

107. Y. Nozaki, K. Tateishi, and K. Matsuyama, *Appl. Phys. Express* **2**, 033002 (2009).

108. Y. Nozaki, K. Tateishi, S. Taharazako, M. Ohta, S. Yoshimura, and K. Matsuyama, *Appl. Phys. Lett.* **91**, 122505 (2007).

109. Y. Nozaki, M. Ohta, S. Taharazako, K. Tateishi, S. Yoshimura, and K. Matsuyama, *Appl. Phys. Lett.* **91**, 082510 (2007).

110. Y. Nozaki, N. Ishida, Y. Soeno, and K. Sekiguchi, *J. Appl. Phys*. **112**, 083912 (2012).

111. Y. Shiroishi, K. Fukuda, I. Tagawa, H. Iwasaki, S. Takenoiri, H. Tanaka, H. Mutoh, and N. Yoshikawa, *IEEE Trans. Mag*n. **45**, 3816 (2009).

112. Y. Yang, B. Liu, D. Tang, B. Zhang, M. Lu, and H. Lu, *J. Appl. Phys*. **108**, 073902 (2010).

113. Z. Celinski, and B. Heinirich, J. Appl. Phys. **70**, 5935 (1991).

114. Z. Zhang, B. Cui, G. Wang, B. Ma, Q. Y. Jin, and Y. Liu, *Appl. Phys. Lett*. **97**, 172508 (2010).